UNIVERSITY OF OKLAHOMA

GRADUATE COLLEGE

INVESTIGATION OF TURBULENCE MODEL PERFORMANCE IN COMPUTATIONAL FLUID DYNAMICS SIMULATIONS OF HORIZONTAL AXIS WIND TURBINES

A THESIS

SUBMITTED TO THE GRADUATE FACULTY

In partial fulfillment of the requirements for the

Degree of

Master of Science

Mechanical Engineering

By

Keaton Q. Mullenix
Norman, OK
2019

INVESTIGATION OF TURBULENCE MODEL PERFORMANCE IN COMPUTATIONAL FLUID DYNAMICS SIMULATIONS OF HORIZONTAL AXIS WIND TURBINES

A THESIS APPROVED FOR THE SCHOOL OF AEROSPACE AND MECHANICAL ENGINEERING

BY THE COMMITTEE CONSISTING OF

Dr. Dibbon K. Walters, Chair

Dr. F.C. Lai

Dr. Jivtesh Garg

ABSTRACT

Wind turbines are critically important in the quest to move towards a non-renewable energy independent world. With the space to add 5M wind turbines, the United States is at the forefront of this transition. Horizontal axis wind turbines (HAWTs) have been studied numerically and experimentally at length. The vast majority of computational fluid dynamics (CFD) studies of HAWTs documented in the open literature have been carried out using two-dimensional simulations. Currently, the available three-dimensional simulations do not provide a comprehensive investigation of the accuracy of different options for modeling of fluid turbulence. In this paper four sets of CFD simulations are carried out using four different turbulence models that are commonly used for engineering level CFD analysis: SST-k-ω, Transition k-k_L-ω, Standard k-ε, and Monotonically Integrated Large Eddy Simulation (MILES). These models were compared with experimental performance and coefficient of power results for a small-scale industrial wind turbine with inverse tip speed ratios (λ^{-1}) in the range 0.072-0.144. They were further investigated to highlight the similarities and differences for the prediction of coefficient of pressure, skin friction coefficient, wall shear, radial velocity and turbulence kinetic energy for λ^{-1} from 0.072 to 0.324. The results showed that no singular model, of the four investigated, was able to consistently predict the power performance with a high degree of accuracy when compared to the experimental results. The models also exhibited both similarities and key differences for the other aspects of flow physics. The results presented in this study highlight the critical role that turbulence modeling plays in the overall accuracy of a CFD simulation, and indicate that end users should be well aware of the uncertainties that arise in CFD results for wind turbine analysis, even when other sources of numerical error have been carefully minimized.

ACKNOWLEDGMENTS

I would like to thank my advisor, Dr. Keith Walters, for his guidance and support in both my personal and professional development. His enthusiasm for research proved to be contagious and created an environment where learning was both enjoyable and fun. I would also like to thank members of the Advanced Computational Research Team: Tausif Jamal, Daniel Jock, Olalekan Shobayo and Huiyu Wang. The support of these individuals cannot be overstated. This group was always there to ease the defeat and share the triumphs that come with this work. Finally, I would like to thank my wife and family who have always supported my efforts in achieving my academic and personal goals.

TABLE OF CONTENTS

LIST OF FIGURES

NOMENCLATURE

c	Unit Chord Length
C	Pressure Coefficient
C_{pow}	Coefficient of power
C_f	Skin Friction Coefficient
D	Diameter
y^+	Non-dimensional Grid Height
λ	Tip Speed Ratio
λ^{-1}	Inverse Tip Speed Ratio
(x/D)	Axial Position
Θ	Blade Pitch Angle
V_r	Radial Velocity
τ_w	Wall Shear
TKE	Turbulence Kinetic Energy
ρ	Air Density
U_∞	Free Stream (Inlet) Velocity
A	Rotor Swept Area

Re	Reynolds Number
AoA	Angle of Attack

CHAPTER I

INTRODUCTION

The global wind turbine industry is constantly competing with non-renewable energy sources to achieve a more efficient and sustainable method of energy harvesting. The United States wind turbine industry has more than tripled over the past decade and currently has nearly 56,000 wind turbines in use according to the American Wind Energy Association (2019). The office of Energy Efficiency and Renewable Energy has estimated that these turbines are capable of producing around 97,000 MW while the country as a whole has a potential wind capacity estimated around 10.5TW (2019).With the current technology, this number can only be reached by adding 5M turbines.

The development of wind turbines is of considerable cost. Therefore, preliminary analysis is critical to the design process, and that results arising from this analysis provide information that can be trusted. As a consequence, researchers seek to develop techniques for predicting the flow behavior around wind turbines with a high level of accuracy and confidence when investigating new designs. At present there is a lack of a predictive tool that can effectively capture all of the flow physics, in quantitative terms, for any given turbine design. Currently, designers and researchers complete these investigations in two global ways. The first method is testing the design at scale in a wind tunnel or in field testing, otherwise referred to as the experimental method. For example, a considerable number of tests have been completed by the National Renewable Energy Laboratory (NREL), and the results are offered via their public database. Though these tests incur many uncertainties from scale effects, wind tunnel setup, and effects of measurement devices, they provide relevant information for many different turbine

designs and operating conditions. They serve as the baseline data for validation of numerical studies, which is the second main method of analysis. Numerical investigations, or computational fluid dynamics (CFD) studies, are completed with the use of physics based turbulence models that resolve varying scales of motion based on the application. An attempt is made to validate the CFD results with the associated experimental measurements. A crucial aspect of these CFD investigations that all designers and researchers must take into account is computational intensity. This greatly affects the initial cost associated with the CFD study, as well as the time it takes for results to be obtained. For this reason, many CFD studies for wind turbines are completed with a two-dimensional domain for several span-wise locations. This method fails to capture the three-dimensional effects inherent to wind turbines in real world applications. That said, there have been numerous CFD studies completed in a three-dimensional space. This adds to the complexity of the problem exponentially and as a result, designers often from forgo the more computationally robust three-dimensional simulations for more cost efficient methods. Along with this concession, many aspects of the computational study are altered in order to achieve results that best fit the empirical data.

This thesis highlights the performance characteristics of four different CFD turbulence models: SST-k-ω, Transition k-k_L-ω, Standard k-ε, and Monotonically Integrated Large Eddy Simulation (MILES).The investigation specifically evaluates the computational techniques, which provided varying results, of each approach for a three-dimensional computational domain for flow around a wind turbine. Currently the vast majority of studies are only available for two – dimensional studies. The details of the flow physics are investigated to highlight differences and similarities between each fluid model and show that a singular model cannot be used to capture all of the flow physics for validation with absolute certainty.

CHAPTER II

LITERATURE REVIEW

The typical fluid dynamics of flow through horizontal axis wind turbines (HAWT) is driven by low speed flow with high turbulence. Many studies concerned with this type of flow field are available in open literature. These studies are validated by comparing computational results with empirical data, which can be broadly classified as a combined computational/experimental approach. The computational methods can be completed in two or three dimensions. An overview of the open literature for two-dimensional and three-dimensional investigations is presented.

2.1 Two Dimensional Studies

Harbert-Acero et al. (2015) investigated 12 turbulence models to assess the associated predicted airfoil dynamics for each. Their two-dimensional computational mesh varied from model to model though they kept their non-dimensional wall height (y^+) at a value of approximately one. In their study they highlighted the main differences of flow physics for the model predictions for a Reynolds Number (Re) of 3×10^6 for angles of attack (AoA) of 0° and 20°. For the AoA of 0°, they found the best lift coefficient to be represented by two models, $SST - k - \omega$ and Standard $k - \omega$. The Transition $SST - k - \omega$ model slightly over predicted the lift coefficient. As for the drag coefficient, the standard $k - \omega$ model provided the worst prediction. The authors attributed these discrepancies to the inability of the models to consistently capture the transition from laminar to turbulent flow, as well as the inadequate

turbulence modeling at the outer layers of the boundary layer. For the AoA of 20°, they found that the Standard $k-\omega$ model predicted lift force the best but each of them failed to accurately capture the drag force.

Aftab et al. (2016) investigated several turbulence models and their influence on prediction of the formation of separation bubbles on the NACA4415 airfoil. The models investigated were: one equation Spallart-Allmars, two equation $SST-k-\omega$, three equation Intermittency (γ) SST, $k-kl-\omega$, and the four equation transition $\gamma-Re_{\theta}\,SST$. Each of these models exhibits different flow physics. The domain extended 20c in each direction from the airfoil, making up a square domain of $20c\ \times\ 20c$, where c is the unit cord length. A grid of 223,000 nodes was used. Incompressible flow was assumed and pressure, density and viscosity were specified based on atmospheric conditions at sea level. The SIMPLE algorithm, along with second order discretization for pressure and momentum, was employed. Two angles of attack were investigated, 6° and 18°. The authors concluded that the $SST-k-\omega$ and Intermittency (γ) SST models yielded similar results but were unable to completely capture the formation of the separation bubble inherent to their case. They also indicated that the $k-kl-\omega$ model yielded results close to the experimental values for C_p at low AoA. The $k-kl-\omega$ model was able to capture the separation of flow but was unable to capture the re-attachment, which was validated by skin friction coefficient. The model that was able to capture the entirety of the flow physics for the given case was the transition $\gamma-Re_{\theta}\,SST$.

2.2 Three Dimensional Studies

Abdelsalam and Ramalingam (2014) conducted a CFD study, using the Standard k-ε turbulence model, for the flow field surrounding the wind turbine blade and the effects

turbulence has on the near wake and far wake flow regions to gain insight on wind farm layout and efficiency. They used a full three-blade geometry, consisting of three airfoils and the entire hub. Their computational domain extended 2D, 25D, 4D, and 3D in the upstream, downstream, span wise and vertical directions respectively. The grid consisted of 2.9M cells and a y^+value ranging from 50-120. An incompressible flow assumption was made. The Semi Implicit Method for Pressure Linked Equations (SIMPLE) algorithm was used along with a 1st order upwind discretization scheme for the turbulence equations. Higher order discretization schemes were attempted but failed due to divergence. The authors validated their model with NREL data for the NACA 63-2xx airfoil. They concluded that the Standard k-ε model was in good agreement for the full rotor approach, thus validating their CFD approach. The authors went on to investigate the wake characteristics for varying tip speed ratios (λ) in the range of 2.53-10.12 for axial positions (x/D) ranging from 0-25. It was further concluded that the Standard k-ε model using the full rotor geometry was superior to assuming the geometry of the rotor to be an actuator disc.

A similar study was conducted by Abdelsalam et al. (2014) where a few changes were made. This study was carried out for the NREL S-series airfoil using the same turbulence model and domain as the previous study. The grid was refined to 5.7M cells and the y^+=50-150. They found good agreement with experimental data for normalized streamwise mean velocity in the near and far wake regions. Their data also suggested that momentum and power losses increase as wind speed decreases. They concluded that this may be caused by the high value of thrust coefficient at low wind speeds. Finally, they observed a large deviation in the turbulence intensity, chiefly due to the inability of accurate measurement of turbulence intensity by use of Sodar and Lidar measurement devices.

Thumthae and Chitsomboon (2009) performed CFD analysis on the NREL S809 airfoil and compared these results with the experimental results provided by several European Union research labs and NREL. Their goal was to validate the numerical solutions with the experimental results in order to provide a design basis for future work. Their computational domain consisted of an unstructured grid with one blade and the associated portion of the hub. Steady-state, incompressible flow was assumed. The rotational speed of the turbine was held constant at $72.0\ rpm$. The diameter of the turbine was $10.1m$. Four tip speed ratios (TSRs) ($\lambda = 3.59, 4.23, 4.76, 5.29$), were examined at five blade pitch angles ($\Theta = 1,3,5,7,12$). The corresponding Re for the varying λ was 7.8×10^5 to 8.0×10^5. The authors used the Standard k-ε turbulence model with the SIMPLE algorithm. The QUICK method was employed for the convective momentum terms while the turbulence equations were handled using a 1st order upwind scheme. The power output for the CFD and experimental approaches were analyzed. Power output was measured as power output from a generator (e.g. electrical power) and as shaft torque from a strain gauge (e.g. conversion of torque to power) for the experimental approach. The authors used the case for $\lambda = 3.59\ and\ 5.29$ with a blade pitch of 12° for validation. Their results show agreement with the strain gage experimental method to within 2.0% and 5.22% for $\lambda = 5.29$ and 3.59, respectively.

Elfarra et al. (2013) carried out an investigation into design optimization of HAWTs using winglets. The applicable portion of the study is in the validation of the CFD results. They analyzed the NREL S809 airfoil using the Standard k-ε turbulence model. Their computational domain consisted of a cylinder that extended 10 times the blade length in the axial direction and 7 times the blade length in the radial direction, though they used Cartesian coordinates. A structured grid of 350,000 nodes was generated with a y^+ ranging from 1 to 7. A fixed rotation

rate with varying axial velocities was investigated, yielding λ in the range of 3.02 to 15.09. Their simulation was performed using a second-order finite volume scheme for the RANS equations. The authors validated their results by comparing them to the experimental data. It was shown that peak performance was predicted at a wind speed of 11ms^{-1}. Disagreement with the experimental results was found at peak performance and 15 ms^{-1}. They suggested that the Standard k-ε model was unable to capture the flow separation and strong vortices at an inboard span of 30%. It is also noted this result is in agreement with previous work of Sezor-Uzol (2006) using an unsteady-state large eddy simulation model.

Krogstad and Lund (2011) used a combined experimental and computational approach to investigate the performance of a model HAWT with an S826 airfoil profile. They used a computational domain that extended $4.5D$ upstream and $7.8D$ downstream and excluded the tower geometry. Because the tower geometry was excluded, the authors were able to take advantage of the periodicity of the blade and hub. However, spherical coordinates were used for computation; therefore the exact boundary conditions of the wind tunnel could not be used. The authors used the SIMPLER algorithm for pressure and velocity coupling while the turbulence model employed was the k-ω SST model. The convective terms in the RANS equations were solved using a first-order upwind scheme. Pressure discretization was handled with first-order interpolation. Results were produced for a fixed inlet velocity of $10\,{}^{m}/_{S}$ with varied rotational speeds, resulting in TSRs of $\lambda = 3,4,5,6,7,9, and\ 11$. The results of the CFD computations showed that the coefficient of power (C_{pow}) for the majority of TSRs was in agreement with the experimental results. The authors concluded that the k-ω SST model was able to predict the wind turbine performance at model scale.

2.3 Outstanding Issues

The papers above show that investigation into HAWT performance is usually achieved by a combined approach. The majority of current 3D CFD studies completed use two main turbulence models, k-ω SST and standard $k-\varepsilon$, whereas the available 2D investigations compare multiple models. This is a direct result of the low computational requirement for a 2D grid as compared to a 3D grid. Multi-model investigations (those using more than one turbulence model) in 2D can be completed in a relatively short amount of time and cost compared to those of a 3D multi-model investigation. Another shortcoming of the available studies completed in 3D is the method in which the model equations are solved along with the grid size. This area in CFD is inversely related with computational demand. Researchers have used discretization methods with 1st-oder accurate schemes with a relatively fine grid (~3.5M cells) or 2nd-order accurate schemes with a relatively coarse grid (<3.5M cells). While multi-model investigations exist for two-dimensional domains, a three-dimensional multi-model investigation using higher order discretization schemes in combination with a fine grid is lacking.

CHAPTER III

TURBULENCE MODELING

The majority of flows in engineering applications are turbulent. These flows are highly unsteady in space and time and are difficult, if not impossible, to capture fully when investigating experimentally. For this reason a predictive tool is necessary to model and investigate turbulent flows. Turbulence modeling employs constitutive equations to predict the evolution of turbulent flows. To date, there is not a single generally accepted turbulence model. Currently there are two main modeling approaches for use with CFD, Reynolds Averaged Navier-Stokes (RANS) and large eddy simulation (LES). Each approach was used in this study. Details of each approach are discussed below.

3.1 Reynolds Averaged Navier-Stokes (RANS)

RANS based turbulence modeling is the most widely used approach in CFD today, due to the relatively low computational cost relative to other types of modeling efforts. The underlying concept of RANS is to solve the governing equations only for the mean or averaged values of the flow variables. Any effects of fluctuating (turbulent) flow are included through prescribed physical models based on estimates of flow statistical quantities. The basis for the RANS approach is the governing, Navier-Stokes, equations of viscous incompressible flow

$$\frac{\partial \tilde{u}_i}{\partial t} + \tilde{u}_j \frac{\partial \tilde{u}_i}{\partial x_j} = -\frac{1}{\rho}\frac{\partial \tilde{p}}{\partial x_i} + \mu \frac{\partial^2}{\partial x_j \partial x_j}\tilde{u}_i \tag{1}$$

$$\frac{\partial \tilde{u}_i}{\partial x_i} = 0 \tag{2}$$

where $\tilde{u}_i$ is the instantaneous velocity vector, $\tilde{p}$ is the instantaneous pressure, and ν is the kinematic viscosity. To obtain the RANS form of the equations, the total velocity is decomposed into the sum of mean and fluctuating components,

$$\tilde{\boldsymbol{u}}(\boldsymbol{x},\boldsymbol{t}) = \underbrace{\boldsymbol{U}(\boldsymbol{x},\boldsymbol{t})}_{\boldsymbol{mean}} + \underbrace{\boldsymbol{u}(\boldsymbol{x},\boldsymbol{t})}_{\boldsymbol{fluctuating}} \tag{3}$$

and substituted back into Eq. 1. The equations are then ensemble-averaged, assuming an infinite ensemble, resulting in the RANS equations

$$\frac{\partial \bar{U}_i}{\partial t} + \bar{U}_j \frac{\partial \bar{U}_i}{\partial x_j} = -\frac{1}{\rho}\frac{\partial P}{\partial x_i} + \mu \frac{\partial^2 \bar{U}_i}{\partial x_j \partial x_j} - \frac{\partial \overbrace{\overbrace{\overline{u_j u_i}}}^{\substack{Reynolds\\ Stress}}}{\partial x_j} \tag{4}$$

$$\frac{\partial \bar{U}_i}{\partial x_j} = 0 \tag{5}$$

These equations are unclosed because, in three dimensions, there are four equations with ten unknowns. The Reynolds stress transport equation can be derived from equations 1 and 3 and is

$$\frac{\partial \overline{u_i u_j}}{\partial t} + \overline{U_k}\frac{\partial}{\partial x_k} u_j u_i = -\frac{1}{\rho}\underbrace{\left(\overline{\frac{\partial}{\partial x_i} u_j p} - \overline{\frac{\partial}{\partial x_j} u_i p}\right)}_{Redistribution} - \underbrace{2\mu\left(\overline{\frac{\partial}{\partial x_k} u_i \frac{\partial}{\partial x_k} u_j}\right)}_{Dissipation}$$

$$\underbrace{-\frac{\partial}{\partial x_k}\overline{u_k u_i u_j}}_{\substack{Turbulent\\ Transport}} \underbrace{-\overline{u_j u_k}\frac{\partial}{\partial x_k}\overline{U_i} - \overline{u_i u_k}\frac{\partial}{\partial x_k}\overline{U_j}}_{Production} + \underbrace{\mu\frac{\partial^2}{\partial x^2}\overline{u_i u_j}}_{\substack{Molecular\\ Viscous\\ Transport}} \tag{6}$$

The turbulent kinetic energy equation can be obtained by the contraction of Eq. (4) and is expressed as

$$\frac{\partial k}{\partial t} + \overline{U_k}\frac{\partial k}{\partial x_k} = \underbrace{-\frac{1}{\rho}\frac{\partial}{\partial x_i}\overline{u_i p}}_{\substack{Pressure\\ Diffusion}} - \underbrace{\mu\overline{\frac{\partial u_i}{\partial x_k}\frac{\partial u_i}{\partial x_k}}}_{Dissipation} \underbrace{-\frac{1}{2}\overline{\frac{\partial}{\partial x_k} u_k u_i u_i}}_{\substack{Turbulent\\ Transport}} - \underbrace{\overline{u_i u_k}\frac{\partial}{\partial x_k}\overline{U_i}}_{Production} + \mu\frac{\partial^2}{\partial x^2}k \tag{7}$$

where $k \equiv \frac{1}{2}\overline{u_i u_i}$. Each of the annotated portions of equation 5 denotes the physical interpretation of the individual terms. Each will be briefly explained.

Dissipation is the decay of turbulence due to viscous damping at small scales, hence the negative sign preceding the term. Turbulent transport is the transport of turbulent kinetic energy in space due to the turbulent velocity fluctuations themselves. Similarly, pressure diffusion is transport of turbulent kinetic energy in space due to pressure fluctuations. Both of these terms lack any production or destruction and are therefore conservative. The production term represents the rate at which the energy from the mean flow is transferred to turbulent fluctuations. The turbulent kinetic energy equation is the basis of the three turbulence models used in the present study. Each of the models is discussed in brief below.

3.1.1 Standard k-ε

The Standard k-ε model, proposed by Jones and Launder (1972), is a fully turbulent eddy-viscosity model. This model is a two-equation model.

$$\frac{\partial k}{\partial t} + \underbrace{u_j \frac{\partial k}{\partial x_j}}_{Convection} = \underbrace{P_k}_{Production} - \underbrace{\varepsilon}_{Dissipation} + \underbrace{\frac{\partial}{\partial x_j}\left[(\nu + \sigma_k \nu_T)\frac{\partial k}{\partial x_j}\right]}_{Transport} \tag{8}$$

$$\frac{\partial \varepsilon}{\partial t} + \underbrace{u_j \frac{\partial \varepsilon}{\partial x_j}}_{Convection} = \underbrace{C_{1\varepsilon}\frac{\varepsilon}{k}P_k}_{Production} - \underbrace{C_{2\varepsilon}\frac{\varepsilon^2}{k}}_{Destruction} + \underbrace{\frac{\partial}{\partial x_j}\left[(\nu + \sigma_\varepsilon \nu_T)\frac{\partial \omega}{\partial x_j}\right]}_{Transport} \tag{9}$$

The standard k-ε model turbulence length scale is calculated by solving a transport equation for the dissipation of turbulence kinetic energy. The model was developed for the prediction of wall boundary-layer flows where the streamwise accelerations cause the boundary layer to revert partially to a laminar flow type. This type of process is termed “reverse-transition” and occurs when the flow rapidly evolves in the direction of flow and is commonly seen in flow

of rocket nozzles and flow over gas turbine blades, hence high speed turbulent flows. It is a fully turbulent model and cannot model laminar flow until reverse transition occurs. This particular model has inherent disadvantages in resolving TKE at areas of high pressure. This phenomenon was investigated by Durbin (2012) and is referred to as the stagnation point anomaly.

3.1.2 Shear Stress Transport (SST)-k-ω

The SST-k-ω model, proposed by Menter (1994), is a fully turbulent eddy-viscosity model that is a combination of the Wilcox (1994) k-ω model and the k-ε model proposed by Jones and Launder (1972). By substituting $\varepsilon = k\omega$ into equations 8 and 9, the equations for SST-k-ω are

$$\frac{\partial}{\partial t}(\boldsymbol{\rho k}) + \frac{\partial}{\partial x_j}(\boldsymbol{\rho u_i}) = \underbrace{\frac{\partial}{\partial x_j}\left(\Gamma_{\mathbf{k}}\frac{\partial k}{\partial x_j}\right)}_{\boldsymbol{Diffusion}} + \underbrace{\boldsymbol{G_k}}_{\boldsymbol{Production}} - \underbrace{\boldsymbol{Y_k}}_{\boldsymbol{Dissipation}} + \boldsymbol{S_k} \tag{10}$$

$$\frac{\partial}{\partial t}(\boldsymbol{\rho\omega}) + \frac{\partial}{\partial x_j}(\boldsymbol{\rho\omega u_i}) = \underbrace{\frac{\partial}{\partial x_j}\left(\Gamma_{\mathbf{k}}\frac{\partial \omega}{\partial x_j}\right)}_{\boldsymbol{Diffusion}} + \underbrace{\boldsymbol{G_\omega}}_{\boldsymbol{Production}} - \underbrace{\boldsymbol{Y_\omega}}_{\boldsymbol{Dissipation}} + \underbrace{\boldsymbol{D_\omega}}_{\boldsymbol{Blending}} + \boldsymbol{S_\omega} \tag{11}$$

This combination yields terms for production, dissipation and diffusion as well as a blending function for the dissipation equation, annotated above. The blending function is applied in the wake region of the boundary layer. Moreover, the Wilcox model is activated in the near wall treatment and the k-ε model is applied to the outer wake and free shear layers.

3.1.3 Transitional k-k_L-ω

The k-k_L-ω model proposed by Walters and Cokljat (2008) is a transition sensitive eddy-viscosity turbulence model. The basis of this model is the Wilcox (1994) k-ω model with an added equation. Incorporation of an additional transport equation models the pre-transitional boundary layer. It is comprised of three model equations (Eq. 12-14) . These equations are for turbulent kinetic energy, laminar kinetic energy, and specific dissipation rate respectively.

$$\frac{Dk_T}{Dt} = \underbrace{P_{k_T}}_{Production} + R_{BP} + R_{NAT} - \omega k_T - \underbrace{D_T}_{Destruction} + \underbrace{\frac{\partial}{\partial x_j}\left[\left(\nu + \frac{\alpha_T}{\sigma_k}\right)\frac{\partial k_T}{\partial x_j}\right]}_{Transport} \quad (12)$$

$$\frac{Dk_L}{Dt} = \underbrace{P_{k_L}}_{Production} - R_{BP} - R_{NAT} - \underbrace{D_L}_{Destruction} + \underbrace{\frac{\partial}{\partial x_j}\left[\frac{\partial k_T}{\partial x_j}\right]}_{Transport} \quad (13)$$

$$\frac{D\omega}{Dt} = \underbrace{C_{\omega_1}\frac{\omega}{k_T}P_{k_T}}_{\substack{Fully\ Turbulent \\ Production}} + \underbrace{\left(\frac{C_{\omega R}}{f_W} - 1\right)\frac{\omega}{k_T}(R_{BP} + R_{NAT})}_{Transition\ Production} - \underbrace{C_{\omega_2}\omega^2}_{\substack{Fully\ Turbulent \\ Destruction}}$$

$$+ \underbrace{C_{\omega_3} f_\omega \alpha_T f_W^2 \frac{\sqrt{k_T}}{d^3}}_{\substack{BL\ Wake \\ Correction}} + \underbrace{\frac{\partial}{\partial x_j}\left[\left(\nu + \frac{\alpha_T}{\sigma_\omega}\right)\frac{\partial \omega}{\partial x_j}\right]}_{\substack{Fully\ Turbulent \\ Transport}} \quad (14)$$

The equations for turbulent and laminar kinetic energy are equations 12 and 13 respectively. Specific dissipation rate, Equation 14, models the transition between fully turbulent and laminar regions. A combination of turbulent and transitionary terms is used. The terms for the respective regimes and their physical significance are annotated above.

3.2 Large-Eddy Simulation (LES)

3.2.1 Monotonically Integrated Large Eddy Simulation (MILES)

The MILES approach, proposed by Fureby and Grinstein (1999), incorporates no sub grid turbulence model. Instead, it utilizes the dissipative nature of finite volume methods for modeling sub grid scales. These subgrid scales, or small scales, are “smeared” by numerical dissipation. This results in an approach effectively resolves scales larger than the local grid scale.

CHAPTER IV

TEST CASE SETUP

4.1 Geometry

The Endurance S-343 small wind turbine geometry was investigated in this study. This turbine is a three blade HAWT that is used primarily for residential applications requiring 10,000 to 20,000 kWh per year. This particular turbine developed by Endurance Wind Power is also suited for applications in small wind farms or for single use in training environments (2012). The rotor diameter (D) is 6.37m which yields a total swept area of 31.9m^2. Two sets of experimental data were used for comparison. Each set was derived using a 28m tall tilting monopole tower. The Windward Engineering, LLC (WE) experimental field test was conducted in Spanish Fork, Utah from October 19, 2011 to October 27, 2011 in accordance with American Wind Energy Association (AWEA) and under a contract as part of NREL's Regional Test Center (RTC) program. The results for the WE experiment were normalized to normal atmospheric conditions since the test site was at an altitude of 4,820 ft. The XPEED Turbine Technologies, LLC (XTT) experiment was conducted under normal atmospheric conditions at the Department of Energy's (DoE) National Renewable Energy Labs (NREL) for several weeks. Both experiments were run with constant recording of wind speed, turbine rotation rate, and power output. Data were conditionally averaged to yield the relationship between tip speed ratio and total power, which is the primary metric to be used in this study for the comparison of CFD simulation results. For the CFD studies, the tower was neglected. It was assumed that the presence of the monopole would have negligible impact on the overall results since it was located downstream of the rotor. This approach was consistent with the previous studies completed by Thumthae and Chitsomboon (2009), Krogstad and Lund (2011), and Elfarra et. al. (2013). Figure 1 shows the geometry considered for the present investigation and Figure 2 is a CAD model of Figure 1. By

disregarding the monopole, the HAWT could be considered rotationally periodic. This allowed the geometry considered for computations to use a 120° section, shown in Figure 3 below. The Endurance S-343 has a variable twist and chord distribution in the span wise direction. A computer aided design (CAD) model was supplied by XTT. The blade pitch at the tip was 0°. Figure 4 shows the airfoil profiles for varied span wise positions.

Figure 1: EWP S-343 test unit at the Windward Engineering's Spanish Fork, UT test site. (E.L. 2012)

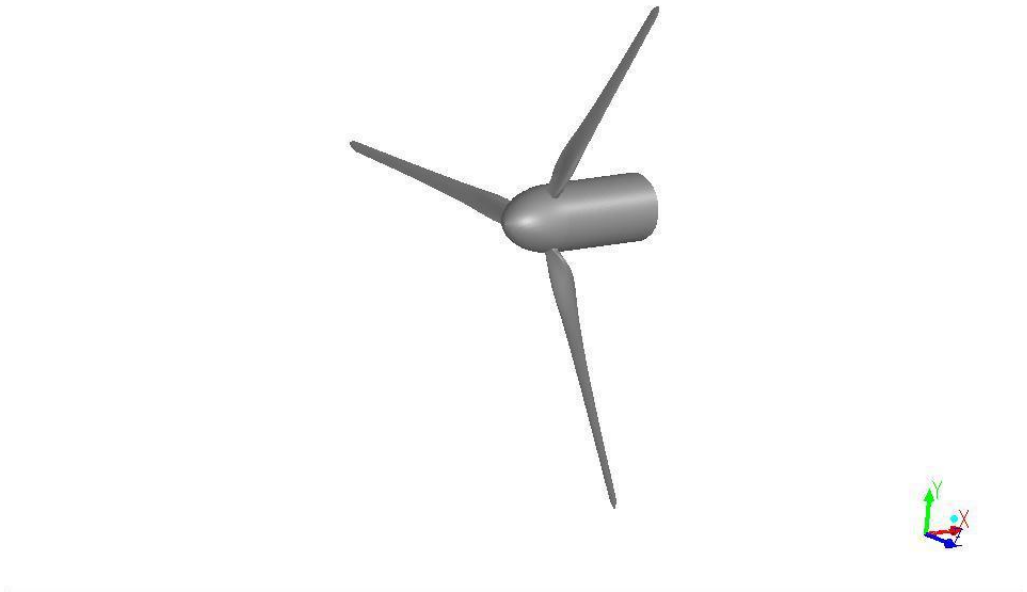

Figure 2: S-343 Full Swept Area Geometry

Figure 3: 1/3 Turbine Geometry

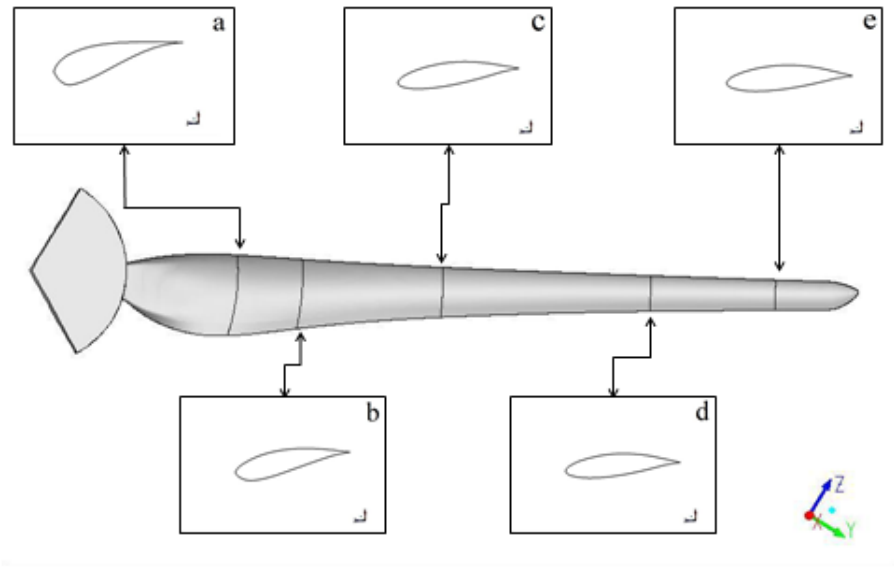

Figure 4: Airfoil Profiles for Span Positions (a) 25%, (b) 33%, (c) 50%, (d) 75%, (e) 90%

4.2 Geometry and Mesh

The farfield boundary was placed at 10D in the radial direction. The inlet and outlet boundaries were located equidistant from the turbine. The inlet and outlet were positioned 10D upstream and downstream of the turbine, respectively. The inlet, outlet, periodic and farfield boundaries are shown in Figure 5.

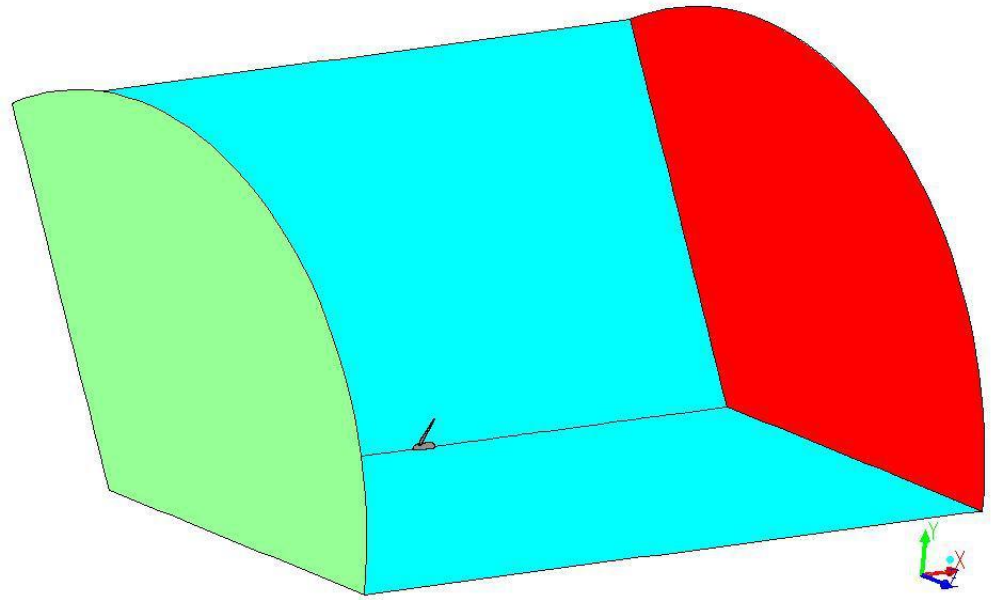

Figure 5: Three Dimensional Computational Domain Boundaries

Ameur et. al. (2011) showed that a grid size of 2×10^6 cells is sufficiently refined for discretization schemes that are of first order error (Ameur et. al., 2011). For their study only half of the rotor and nacelle were considered. This resulted in a computational grid size of4×10^6. For the current study a mesh size of 2.3×10^7cells was used. These cells populated the volume inside the boundaries of figure 5. Since the geometry was in 120° sections, the resultant grid, in comparison with Ameur et. al., was nearly 7.0×10^7 cells. Because no convergence issues were encountered using second order schemes and since the current mesh is an order of magnitude larger than previous studies suggested, the current mesh is assumed to be sufficiently refined. The mesh consists of tetrahedral and hexahedral cells. Compared with tetrahedral cells, hexahedral cells yield a solution with lower discretization error (Hefney & Ooka, 2009). The hexahedral cells are located in the region near the blade wall in order to resolve the boundary layer more accurately (Figures 6 and 7). To ensure the boundary layer is being resolved

accurately it was important to determine the non-dimensional wall height (y^+). In general, a y^+ value greater than 5 is indicative of the cell being located outside the viscous sublayer. For this reason, the first cell y^+ average for $\lambda^{-1} = 0.324$ was held to 1.45. Each y^+ average for $\lambda^1 < 0.324$ resulted in$y^+ \leq 1.45$. This indicates that the simulations have a well refined grid near the wall. Figure 7(a) shows these regions at a span wise location of 90% with a close-up view in Figure 7(b). Figure 7(c) shows the close-up of the structured mesh at the leading edge, also for the span wise location of 90%.

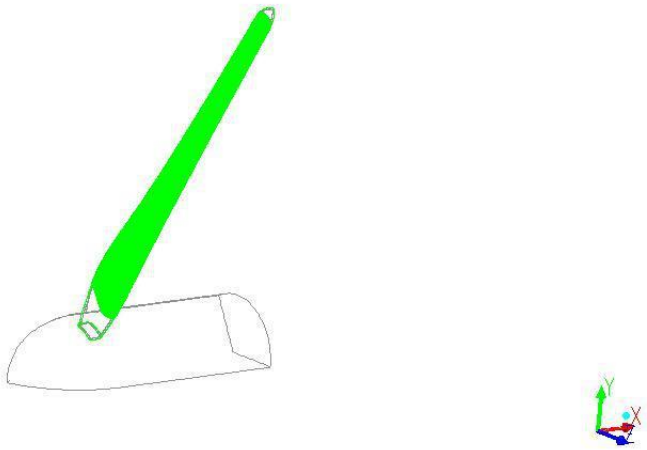

Figure 6: Region of Mesh Near Blade Wall

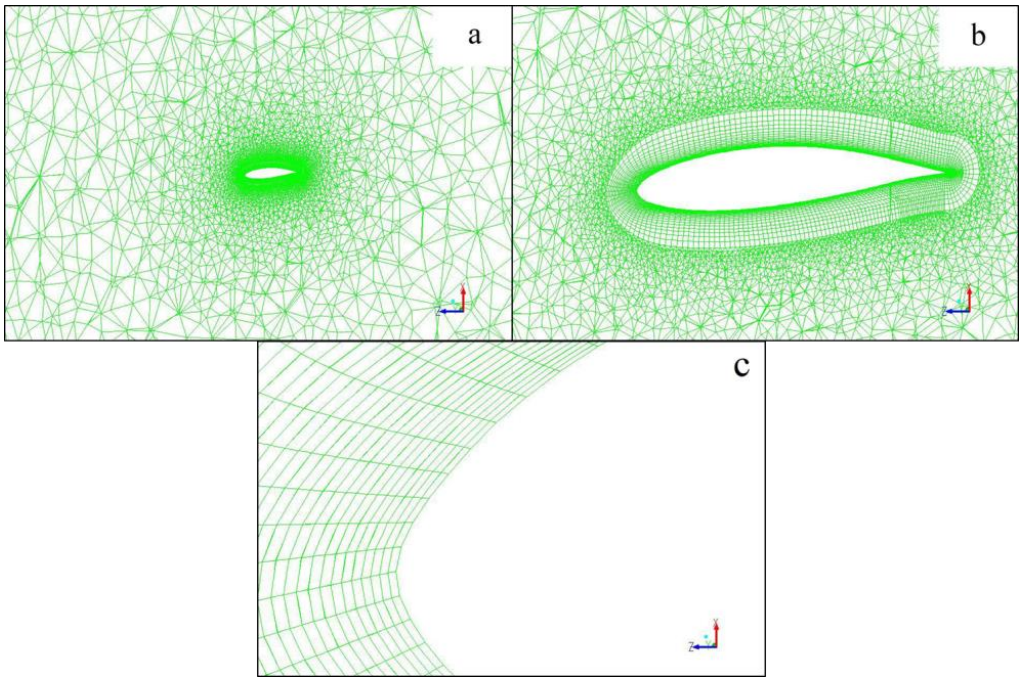

Figure 7: (a-b) Two Dimensional Interface of Structured and Unstructured Meshes near Turbine Rotor at Span=90%, (c) Visualization of Structured Mesh near Leading Edge of S343 at Span=90%

4.3 Boundary Conditions

Flow was propagated in the positive x-direction from the inlet boundary. A uniform mean velocity was prescribed at the inlet. The outlet, farfield and periodic boundary conditions were constant across varying approaches throughout the CFD study. The outlet was defined as a pressure outlet at standard atmospheric pressure, or zero static gage pressure. The farfield was defined as a stationary wall with a specified shear of zero and was located sufficiently far enough from the blade tip such that the velocity experienced at the farfield was no more than 101% of the velocity prescribed at the inlet. This decision was made to increase the numerical stability while having a negligible effect on the results. The inlet condition varied across different approaches as each of the turbulence models dictated. For the SST-k-ω and Standard k-ε models the inlet condition was specified with a turbulent intensity of 5% and a turbulent viscosity ratio

of 10. The k-k_L-ω model inlet condition also required a condition for laminar kinetic energy (k_L). The k_L was assumed to be zero but was set as 1×10^{-6} to avoid computation errors caused by k_L=0. Due to the laminar viscous model used in the MILES approach, no additional turbulence conditions were required.

For each turbulence model, various inlet velocities were specified with a constant rotor rotation rate of 17.38 rad/s. A rotation rate of $17.38 \frac{rad}{s}$ was used in the XTT experiment while the WE experiment had a varying rotation rate for each respective inlet velocity. The mean rate of rotation used by WE for inlet velocities ranging $4 - 17\, {}^{m}/_{s}$ was $17.65 \frac{rad}{s}$. The largest difference in rotation rate was at the inlet speed of$4\, {}^{m}/_{s}$. The corresponding rotation rate for the WE experiment was $15.17 \frac{rad}{s}$. Because the average rotation rate was similar for each study, it was not expected that the difference would be the root cause of a difference in coefficient of power. Therefore both experiments were assumed relevant for comparison to the present study. The rotation rate for the CFD studies was achieved by applying a rotating reference frame to the interior of the domain. This resulted in λ^{-1} ranging from 0.072 to 0.324. The turbine was defined as a wall with a roughness height of zero. The no-slip condition was applied at the wall boundary.

A comparison of air density assumptions was performed for the MILES approach. Two different equation of state assumptions were performed. These two assumption were constant density and ideal gas assumption. This examination was performed for $\lambda^{-1} = 0.072 - 0.252$. The comparison showed there was very little difference in the two approaches. The ideal-gas assumption under predicted for the majority of λ^{-1} investigated, with the exception of $\lambda^{-1} = 0.072$ and $\lambda^{-1} = 0.090$. The average variation in C_{pow} was 1.3%. The maximum variation was 18%. This was found at $\lambda^{-1} = 0.072$ and was an over prediction by the ideal gas assumption

approach. It was determined that the constant air density approach was sufficient for the study. Consequently, a constant air density of $1.225\,\frac{kg}{m^3}$ and dynamic viscosity $1.7894 \times 10^{-5}\,\frac{kg}{m-s}$ were specified as the fluid properties.

4.4 Numerical Methods

All of the simulations were performed using the pressure-based solver in ANSYS Fluent v16.2. The numerical scheme details differed depending on whether a RANS or MILES turbulence modeling approach was used, and details are provided below.

Three RANS models were employed for the current study: SST-k-ω, k-kl-ω, and Standard k-ε. A second order upwind scheme was used for the convective terms of all transport equations, including mean velocity and turbulence model variables (e.g. k, ε) (Barth and Jesperson). The mass flux across cell interfaces was computed using a momentum interpolation method similar to Rhie-Chow interpolation (Mathur and Murthy). The pressure terms of each model were discretized using a standard scheme in which the face pressure was obtained from an average of the pressure values in neighboring cells. Pressure-velocity coupling was handled by the SIMPLE scheme (Patankar and Spalding). Each of these models was applied using a steady state assumption. Steady state problems can be said to be converged when additional iterations yield no change to the solution. Simulations were found to be well converged after 15,000 iterations for each RANS model. This was confirmed by examining the Coefficient of Moment (CoM) with respect to the number of iterations. Shown below are a subset of the SST-k-ω model CoM. The initial 1,000 iterations for each of the simulations were unstable. The CoM for each of the cases was converged after 5,000 iterations. To ensure each case was sufficiently converged the simulations were carried out an additional 10,000 iterations. The figure below illustrated how

the CoM's become constant, thus converged. Inlet velocities 7.0 m/s and 7.5 m/s appeared to have periodic behavior in their region of convergence. The magnitude of this periodicity was negligible and therefore the data was also considered to be converged. This behavior was visualized for all λ^{-1} across all of the investigated RANS turbulence models.

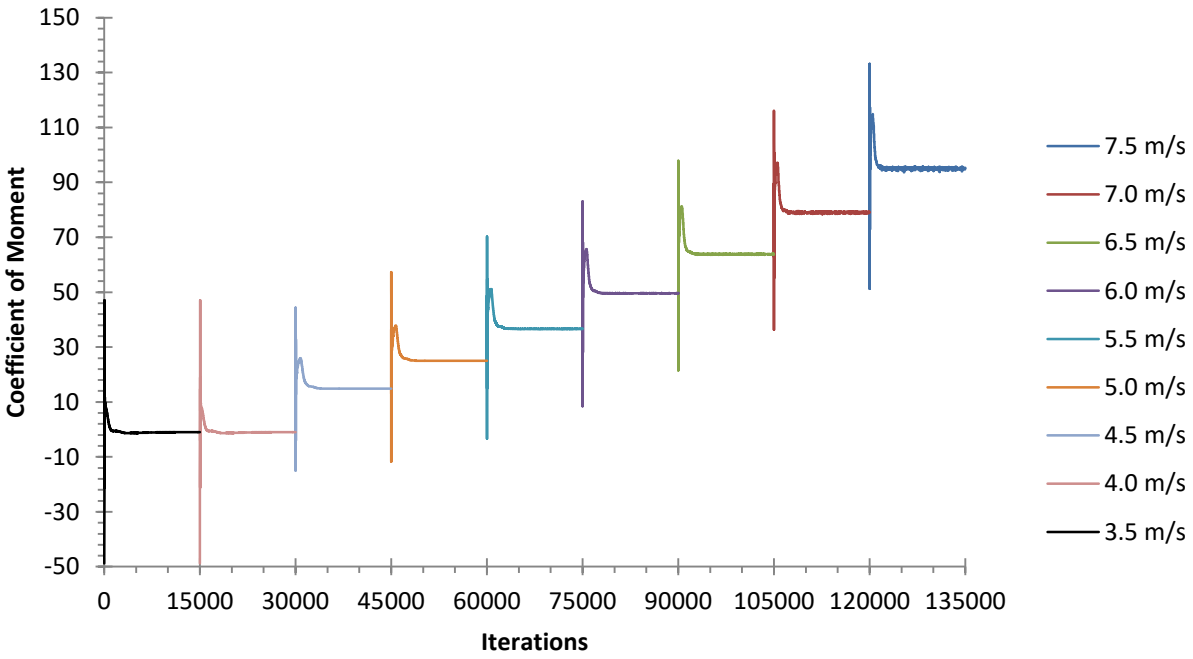

Figure 8: Coefficient of Moment Used for Convergence

The MILES approach was employed by using the Laminar Viscous Model. Numerical details were identical to that for the RANS turbulence models except that a different scheme was used for the convective terms and the discretized unsteady (time-derivative) term was added to the model equations. The bounded central difference scheme was used instead of second-order upwinding in order to reduce the effect of numerical dissipation on the simulations (Jasak et al.). The transient formulation that was employed was the second order implicit scheme, i.e. the three-point backward difference. For convergence of unsteady computations using an implicit time-stepping scheme, convergence should occur at each time step. A time step size of 1×10^{-4} s was used with a maximum of 10 iterations per time step. Convergence at each time step was

achieved with this combination. This was confirmed by ensuring the coefficient of moment was reduced by at least two orders of magnitude in each time step.

4.5 Computational Requirements

As aforementioned, each simulation employed in the current study was completed using ANSYS Fluent v16.2. Because the mesh size was 2.3×10^7 cells, the use of High Performance Computing (HPC) resources was a necessity. HPC resources were provided by the University of Oklahoma Supercomputing Center for Education and Research (OSCER). Each simulation required a minimum of six computing nodes. Each node consisted of 20 CPU cores with 32GB RAM. With six nodes the RANS simulations were completed in 8-16 hours of run time for one λ^{-1}. The MILES simulations required nearly 72 hours of run time to complete one λ^{-1}.

CHAPTER V

RESULTS

In this chapter CFD simulation results for each of the turbulence models are presented. Both quantitative and qualitative results are presented in order to highlight differences and similarities between the models. Results are also compared to available experimental data for validation purposes. As noted above, the goal of the study is to isolate the true turbulence model performance for these cases by carefully addressing sources of error due to domain and computational geometry, dimensionality of the simulation (2D versus 3D), mesh density, and discretization scheme. Nevertheless, both known and unknown sources of uncertainty are expected to be present in the CFD results and experimental data. For one of the experimental data sets, uncertainly was quantified and error bars are included in the plots shown here. In addition, it must be noted that the experimental test cases measured electrical power generation, while the CFD results show only the power delivered to the turbine blades by the flowing air, and do not take into account the electrical losses which are inherent in experimental studies of HAWTs. Since no experimental data regarding electrical losses was provided, and since an analysis of wind turbine electrical systems is beyond the scope of the present work, it is assumed that the CFD results will be biased to higher power output values than the companion experimental measurements.

5.1 Power Output/Performance

Performance, which refers to the overall power produced by a wind turbine as a function of wind speed, is the most widely investigated global factor for wind turbines since this is the total amount of power extracted from the wind. For HAWTs the wind speed at which maximum power is generated is referred to as the point of rating. The power and wind speed found at this

point determine the rated power and rated inverse tip speed ratio (λ_{rated}^{-1}). Comparison was made between two experimental data sets and four turbulence models to inspect the similarities and differences between turbulence model predictions of the point of rating. The regions preceding and following this rating point were also investigated to further highlight differences and similarities between the turbulence models and experimental results over a range of operational wind speeds.

5.1.1 Experimental Data

Two experimental data sets were used for comparison in the current study, and the power output curves for each are shown in Figure 9. These experimental studies were completed by WE (2012) and XTT. These studies were carried out different operating conditions. The WE study was conducted at the Windward Engineering outdoor test facility. The XTT study was conducted at the NREL wind turbine field test facility. Each study predicted rated power output within 2% for the same turbine geometry: 6.11kW and 6.00kW for XTT and WE, respectively. The chief difference between the two studies was that the WE study predicted a $\lambda_{rated}^{-1} = 0.226$ while the XTT study did so at $\lambda_{rated}^{-1} = 0.251$. This difference was assumed to be a direct result of experimental error. This is similar to the findings of the CFD results in the sense that each turbulence model produced a varying result due to the complexity of the fluid dynamics in three dimensions. The differences between the two experimental studies highlight the presence of known and unknown sources of uncertainty, in addition to the formal uncertainty estimates provided by the WE experiments and indicated using error bars in Figure 9.

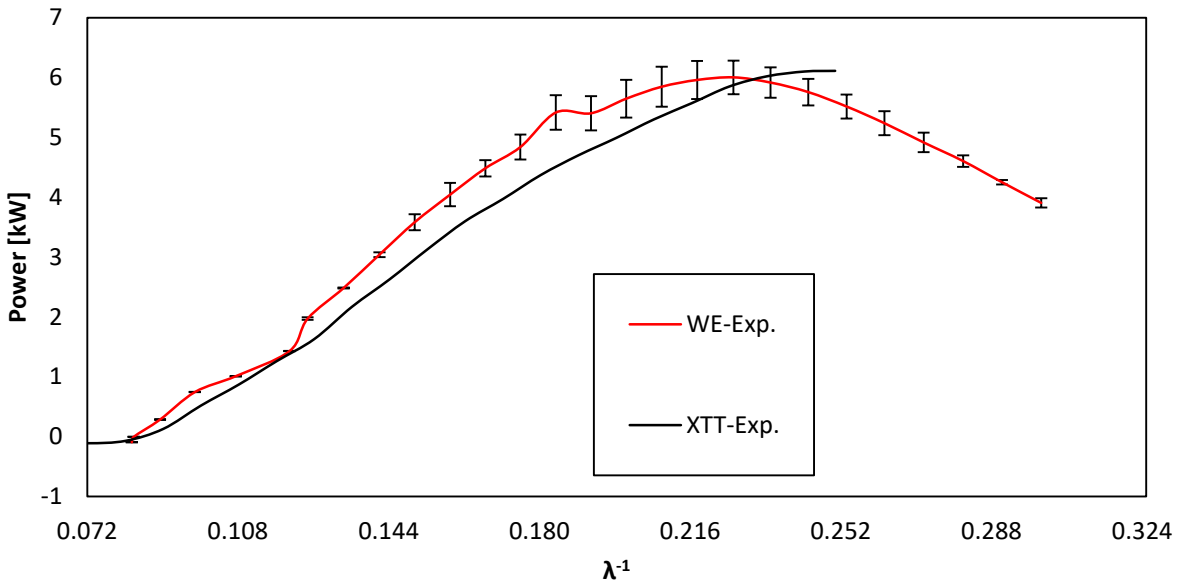

Figure 9: WE and XTT Experimental Results

5.1.2 CFD Results

Results obtained using each of the four turbulence models are shown in Figure 10 and compared to the experimental data sets. The figure clearly shows that there is considerable variation in predicted power for the different turbulence models, suggesting that the uncertainty due to turbulence model choice is substantially greater than the uncertainty in the experimental data. It is also clear that no single model provides the best agreement with experimental data over the entire range of wind speeds investigated. Lastly, it is apparent that all of the models show considerable overall error over at least some portion of the operational range. The performance of each model is discussed in more detail in the following paragraphs.

The SST-k-ω model over predicted the power output in the λ^{-1} range of 0.072-0.180. The λ^{-1}_{rated} was predicted lower than each of the experiments. The λ^{-1}_{rated} occurred at $\lambda^{-1} = 0.198$ which was a 12% and 21% under prediction relative to the WE and XTT studies respectively. The rated power output was 5.67kW for the SST-k-ω model. This was around a 6-

7% under prediction relative to the experimental results. In the post stall region, the SST-k-ω model grossly under predicted the power output. For this region, this model yielded the under largest prediction for all models.

The MILES turbulence model grossly over predicted the power output relative to the experimental studies up to the point of stall. The power output in the λ^{-1} range of 0.072-0.180 for the MILES approach was predicted much higher than any other model for the same range. This approach predicted $\lambda_{rated}^{-1} = 0.180$ with a resulting rated power output of 6.87kW. The rated power output was over predicted by 14% and 12% compared to the WE and XTT experiments respectively. Further, the λ_{rated}^{-1} was under predicted by over 20% relative to each experiment. In relation to the post stall region of the WE experiment, $\lambda^{-1} = 0.234 - 0.300$, the WE study the MILES turbulence model were close in their prediction of power output.

The k-k_L-ω model predicted the power output closer to the experimental studies than the MILES approach for $\lambda^{-1} = 0.072 - 0.180$, but showed the largest over prediction of all models from that point through the point of rating and post stall region. The maximum power output of 8.67kW was an over prediction of over 40% relative to the experiments. Stall occurred at $\lambda_{rated}^{-1} = 0.234$ and was within 4% and 7% of the WE and XTT experiments respectively. This model provided the closest correlation to the point of rating in regards to the λ^{-1} while providing the largest discrepancy for power output at the point of rating. Interestingly, the k-k_L-ω model appears to most closely follow the overall shape of the experimental power output curves, although it is not clear if this is an indication that the model is more correctly resolving qualitative flow features than the other models (for example boundary layer transition, which the k-k_L-ω model was designed to predict) or whether it is coincidence. Further simulations using

alternative turbine geometries would likely help to clarify this point, but they are beyond the scope of this work.

Similarly, the k-k_L-ω model was able to predict an anomalous behavior that existed in the WE experiment. This correlation was only qualitative in nature and occurred just prior to the point of rating in both models. Specifically, the WE experiment experienced an increase in power for $\lambda^{-1} = 0.072 - 0.184$, a subsequent decrease in power at $\lambda^{-1} = 0.184 - 0.192$, and then an increase in power up to stall at $\lambda^{-1} = 0.192 - 0.226$. The k-$k_L$-ω model produced a similar behavior that was drawn out over a larger region of λ^{-1}. Specifically, the k-k_L-ω model showed there to be an increase in power from for $\lambda^{-1} = 0.072 - 0.198$, a decrease in power at $\lambda^{-1} = 0.198 - 0.216$ and then an increase in power up to stall from $\lambda^{-1} = 0.216 - 0.234$.

The standard k-ε model yielded the only under prediction of power output for all values of λ^{-1} in the pre-stall region. At very low values of λ^{-1}, around 0.072-0.108, the model had a strong correlation with the XTT experimental results. This correlation diminished as a progressive under prediction as the value of λ^{-1}increased. The point of rating for the model occurred at $\lambda^{-1} = 0.307$ with a corresponding power output of 5.64kW. Compared with the WE and XTT results the stall point λ^{-1} was over predicted by 35% and 22% respectively. This was the largest difference in stall point compared with all other models. The power output at the point of rating was within 6% of both experiments. Because the point of rating for the standard k-ε model was near the maximum λ^{-1} for this study, information regarding the post stall region was not available, though it appears that the decline in power output predicted by the model is much less steep than that found in the WE experiments, which provide data up to about $\lambda^{-1} = 0.3$.

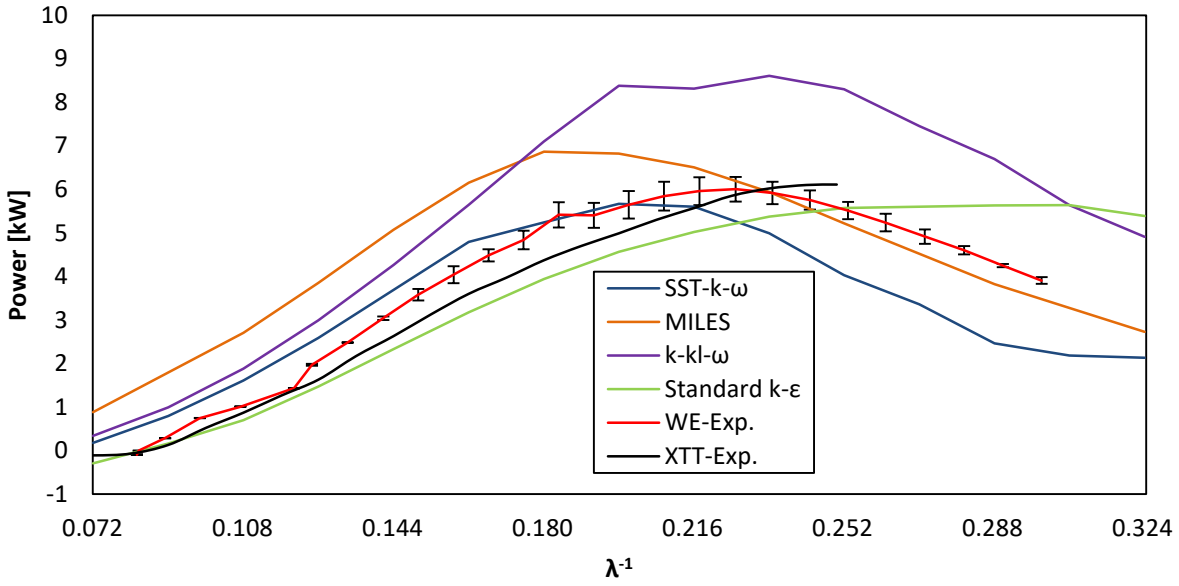

Figure 10: Power Curves for CFD and Experimental Results

5.2 Coefficient of Power

Figures 11 and 12 show the coefficient of power, C_{pow}, as a function of λ^{-1}, for the experimental results and CFD simulations using each turbulence model. The definition used for C_{pow} in the present study is

$$C_{pow} = \frac{P}{\frac{1}{2}\rho U_{\infty}^{3} A} \tag{15}$$

where P is the power generated by the turbine, ρ is the density of air, U_{∞} is wind speed and A is the rotor swept area. This variable can be generalized as the efficiency of the turbine in converting wind energy into mechanical energy. As noted above, however, it does not take into account efficiency (losses) associated with conversion of mechanical energy to electrical energy.

There exists a limit on the maximum C_{pow} a turbine can extract from the wind. This is known as the Betz-Joukowsky limit. This limit depends on major simplifications and

assumptions about airflow past a wind turbine though no well-documented study has violated this limit (Wood, 2013). The limit states that the maximum C_{pow} that can be extracted from the wind is

$$\boldsymbol{C_{pow,max} = 16/27 \approx 0.593} \quad (16)$$

This was determined by equating equation 13 with the axial induction factor (a), where

$$\boldsymbol{a = 1 - \frac{U_\infty}{U_0}} \quad (17)$$

therefore

$$\boldsymbol{C_{pow} = \frac{4U_0^2(U_\infty - U_0)}{U_\infty^3} = 4a(1-a)^2} \quad (18)$$

where U_0 is the wind speed outside of the bounding streamline. The $C_{pow,max}$ will occur when the change in C_{pow} with respect to a is zero. This occurs when at $a = \frac{1}{3}$.

Figure 11 shows the relationship between experimental results and each CFD approach for C_{pow}. Figure 12 provides an enhanced view of the region in which most of the model results appear to converge to a similar value of C_{pow}. Consistent with performance results shown below, it is apparent that none of the models are able to accurately predict C_{pow} over the entire range of wind speeds investigated. The behavior of the measured data and computational results are discussed in more detail below.

5.2.1 Experimental Data

Coefficient of power for each of the experiments varied similar to the results for the power output. This result was expected as the power output and coefficient of power are closely related as indicated by Eq. (15). The maximum C_{pow} for each experiment occurred in the same approximate region: $\lambda^{-1} = 0.125 - 0.150$ for WE, and $\lambda^{-1} = 0.135 - 0.153$ for XTT. The WE maximum, $C_{pow} = 0.3$, occurred at four successive data points and, similarly, the XTT maximum,

C_{pow} = 0.26, occurred at three successive data points. It is likely that experimental uncertainty accounted for these maximum values presenting themselves across a range of λ^{-1} versus at a singular point.

5.2.2 CFD Results

Relative to the WE experiment the SST-k-ω model showed the greatest differences in C_{pow} near the endpoints of the wind speed range. The largest error magnitude was experienced around $\lambda^{-1} = 0.288 - 0.324$. The same behavior existed from $\lambda^{-1} = 0.072$ to just before 0.108 but was not as severe as the end region. For $\lambda^{-1} = 0.108 - 0.288$, the model error magnitude progressively decreased until reaching a minimum around $\lambda^{-1} = 0.216$. From this point on the error magnitude grew until reaching a maximum at $\lambda^{-1} = 0.324$. When comparing this model to the XTT experiment, similar results were seen for the majority of the values of λ^{-1}. There was one significant difference between the two. At $\lambda^{-1} = 0.216$ the model reached its minimum error magnitude, similar to the comparison with the WE results. From this point on the error magnitude increased much faster than when compared to the WE experiment.

The MILES approach yielded a results for C_{pow} that was qualitatively different than all other models and experiments for $\lambda^{-1} = 0.072 - 0.144$. This was the greatest anomaly that was found for the investigation into C_{pow}. Most notably, the simulations appear to violate the Betz limit in the region of $\lambda^{-1} = 0.072$ to 0.108. However, the error magnitude relative to the experimental data sets displayed a similar qualitative behavior as the other CFD approaches over the majority of the wind speed range. The largest error magnitude was experienced at $\lambda^{-1} = 0.324$ followed by $\lambda^{-1} = 0.072$. The model error magnitude behavior for the remaining λ^{-1} was not the same for each experiment. When compared with the WE experiment the error magnitude progressively decreased from $\lambda^{-1} = 0.090$ to $\lambda^{-1} = 0.288$. A minimum error magnitude was

found at $\lambda^{-1} = 0.288$. For the XTT comparison the MILES error magnitude progressively decreased from $\lambda^{-1} = 0.090 - 0.234$. The minimum error magnitude was found at $\lambda^{-1} = 0.324$. Immediately following this $\lambda^{-1}$the error grew exponentially to a maximum at $\lambda^{-1} = 0.324$.

The k-k_L-ω model exhibited similar behavior as the previous models for the error magnitude. When compared to the WE experimental results the k-k_L-ω model showed the same behavior as the other models at the endpoints. However, the maximum error magnitude was found to be at $\lambda^{-1} = 0.072$. The error magnitude decreased to from $\lambda^{-1} = 0.072 - 0.126$ and experienced a slight increase from $\lambda^{-1} = 0.126 - 0.288$. Immediately following this point the error quickly dropped the absolute minimum at $\lambda^{-1} = 0.307$. Similar qualitative behavior existed for the model when compared with the XTT data. The maximum was found at the initial λ^{-1} while the minimum was predicted much earlier at $\lambda^{-1} = 0.270$.

When compared with the WE experimental results, the standard k-ε model behaved similar to the SST-k-ω model for the range of $\lambda^{-1} = 0.090 - 0.288$ showing the minimum error magnitude at $\lambda^{-1} = 0.234$. The largest error magnitude was found at $\lambda^{-1} = 0.090$. For $\lambda^{-1} = 0.288 - 0.324$ the standard k-ε model behaved nearly identical to the k-k_L-ω model. This result was very different when compared to the XTT experimental results. Again, the maximum error was found at $\lambda^{-1} = 0.324$ but the model did not behave in the same manner as any other model. For $\lambda^{-1} = 0.090 - 0.252$ the error magnitude was near constant around 10-18%. This was interpreted as providing a good quantitative match with this experiment. Though this appeared to suggest that the standard k-ε model was preferred, however two key points should be made. First, the standard k-ε model is known to overpredict turbulent kinetic energy and effective viscosity in the leading region of airfoils, and in fact this behavior was observed in the present

simulations (discussed in more detail below). This means that the model is expected to over predict viscous losses which results in lower overall power output and coefficient of power prediction. It is possible that the experimental results included surface roughness effects that were not taken into account in the CFD simulations, and that the standard k-ε is artificially mimicking that effect. If that is the case, then the standard k-ε results should be viewed perhaps as a fortuitous cancellation of errors rather than an example of inherent model superiority. Second, the known bias due to electrical losses in the experimental tests should lead to an overprediction by the CFD results, rather than an underprediction as shown by the standard k-ε model. Both of these considerations suggest that observed C_{pow} behavior should not be taken as sufficient evidence that the standard k-ε model is in general the best choice for wind turbine predictions.

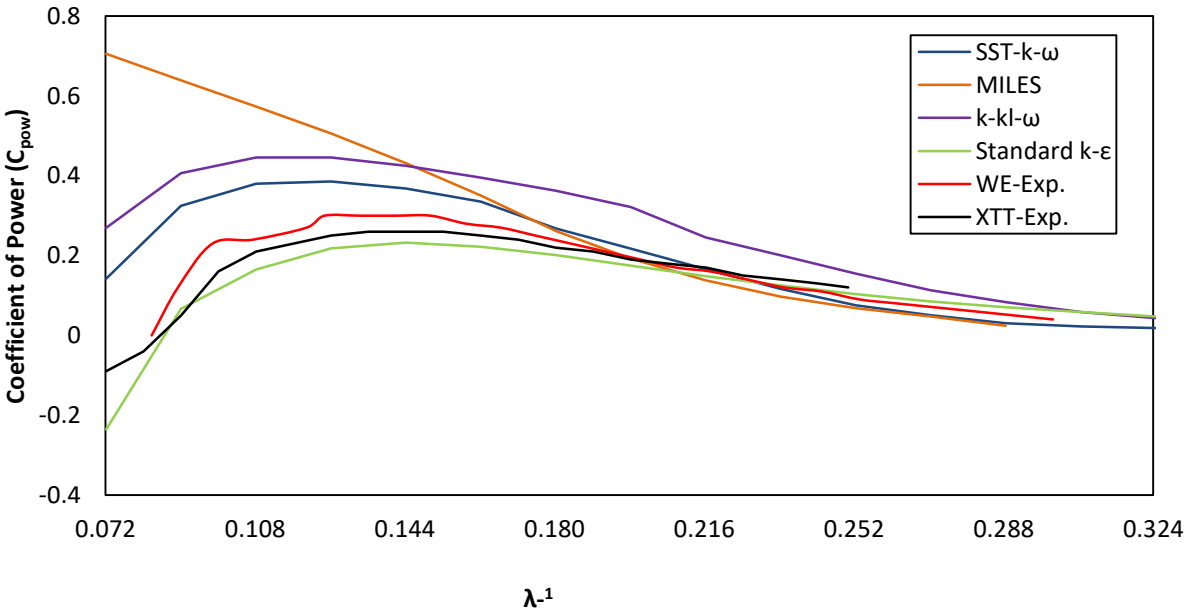

Figure 11: Coefficient of Power for CFD and Experimental Results

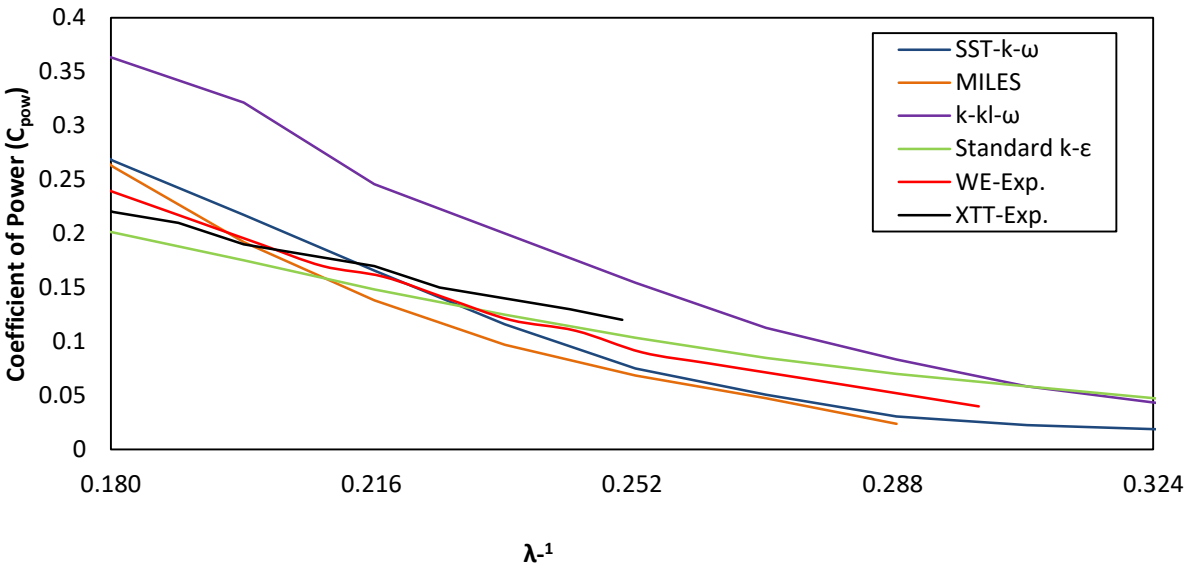

Figure 12: Coefficient of Power (Enhanced View of Figure 10)

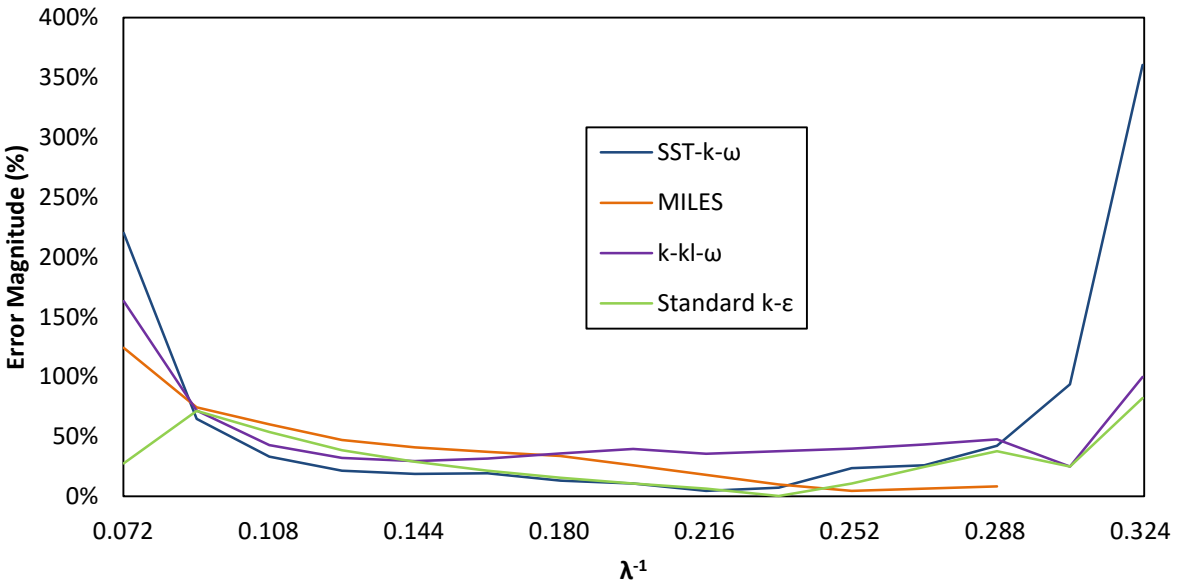

Figure 13: Error Magnitude, WE Experimental Baseline

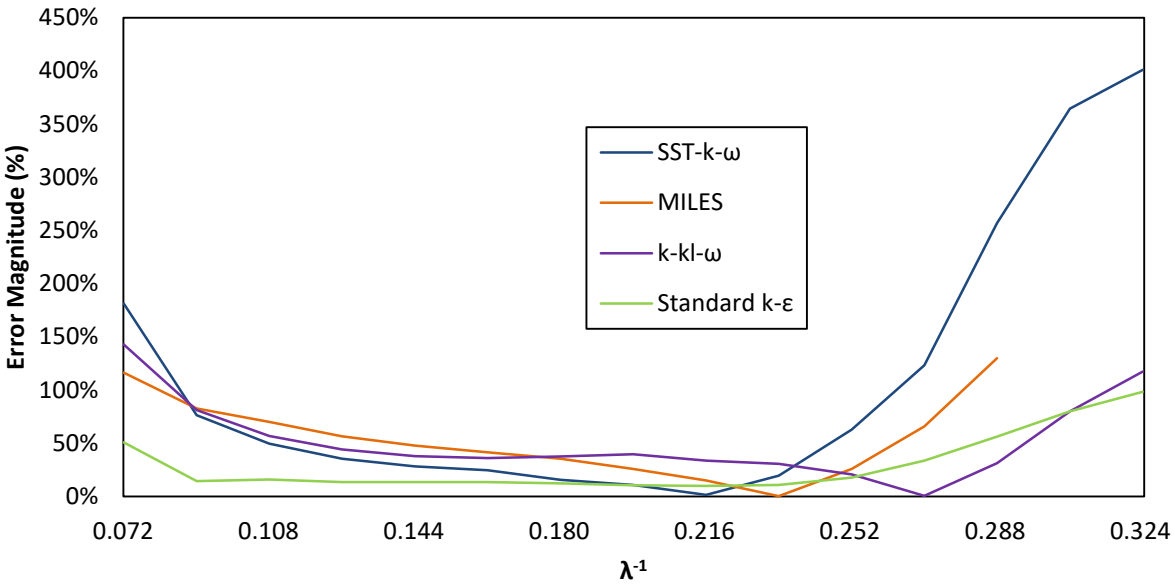

Figure 14: Error Magnitude, XTT Experimental Baseline

5.3 Airfoil Pressure and Friction Loading

Coefficient of pressure (C_p) and skin friction coefficient (C_f) were examined at a location of 0.45D, which corresponds to 90% span of the airfoil (Figure 4e). These two variables were chosen as they have a direct effect on the power output of the turbine. Generally, variation of C_p on the pressure and suction surfaces contributes to the power output, while C_f quantifies the viscous surface friction, which produces a net drag force and reduces the power output. Three values of λ^{-1} were inspected ($\lambda^{-1} = 0.072, 0.108, 0.144$) and the resultant distribution of C_p (figs. 16, 19, and 22) and C_f (figs. 25, 30 and 33) is shown. These values of inverse tip speed ratio (λ^{-1}) were chosen since this range is the typical operating range for the chosen turbine geometry and because this was where the maximum C_{pow} was found in each of the experiments. No experimental data was found for comparison of C_p or C_f. For this reason the model data were compared relative to one another to further highlight variability in turbulence model results. The

C_p and C_f were inspected on the airfoil surface and the respective plots for each were constructed using the following diagram (Figure 15). The plots have two global regions which is made up of a pressure side and suction side. The pressure side corresponds to s > 0 while the suction side corresponds to $s < 0$. These two regions are divided in the plots for C_p and C_f by the stagnation point where $s = 0$. The endpoints of the plots both correspond to the trailing edge of the airfoil. At this point $s = \pm 1$.

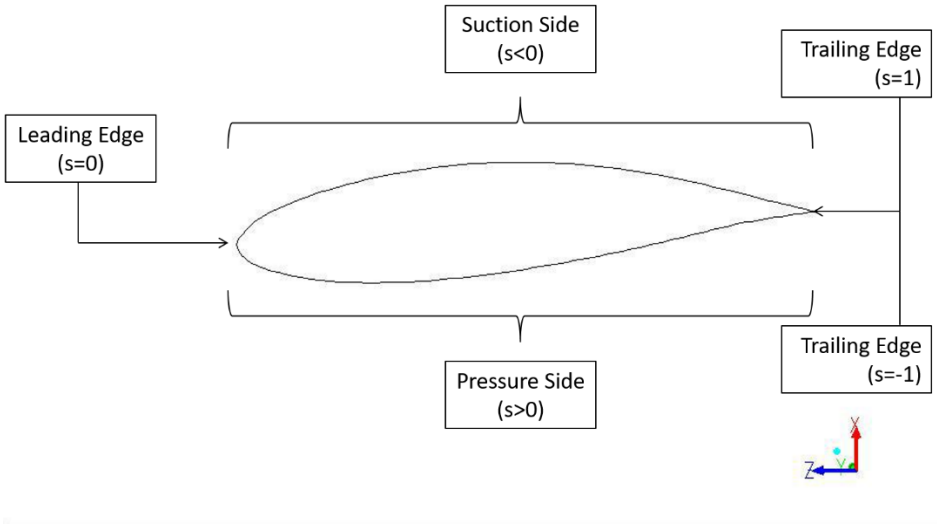

Figure 15: Regions for Pressure and Friction Plots

Coefficient of pressure, C_p, is the ratio of gage pressure to dynamic pressure. For the present study C_p was defined as

$$C_p = \frac{p - p_\infty}{\frac{1}{2}\rho U_\infty^2} \tag{19}$$

where p is static pressure on the airfoil, p_∞ is the atmospheric pressure, ρ is air density, and U_∞ is the inlet velocity. Static pressure is on the airfoil surface the dependent dimensional variable in the computation of C_p.

The plots show below show the distribution of C_p for the pressure and suction sides of the airfoil. The corresponding relative velocity magnitude (RVM) contours are shown for each of the plots (Figures 17, 20 and 23). RVM for the present study was defined as the velocity magnitude in the rotating reference frame normal to the hub of the turbine. RVM contours are shown due to the relation between velocity and pressure. It is well known that an inverse relationship between pressure and velocity exists. Therefore it can be stated that any increase in C_p is in general a result of a decrease in RVM, and vice versa. It can further be directly related to the turbine C_{pow}. An increase in the difference in C_p between the pressure and suction sides in general results in an increase in C_{pow}.

5.3.1 Pressure-Side Coefficient of Pressure

The k-k_L-ω, standard k-ε, and SST-k-ω models exhibited nearly the same qualitative behavior for $\lambda^{-1} = 0.072$ near the leading edge of the airfoil. The outlier for this λ^{-1} value was found with the MILES turbulence model. The MILES turbulence model predicted a larger pressure loading on the airfoil for the majority of the pressure side. This difference can be seen in figure 17. Each of the other models predicted roughly the same RVM whereas the MILES approach predicted the RVM to be much lower. Near the trailing edge of the pressure side the MILES model behaved similar to the k-k_L-ω model while the standard k-ε and SST-k-ω behaved similarly. The corresponding contour for RVM (Figure 18) confirms this. The standard k-ε and SST-k-ω models experienced an increase in velocity near the trailing edge while the MILES and k-k_L-ω models experienced a flow detachment near the trailing edge. This behavior is due to the fact that both of these models predict an initially laminar boundary layer on the pressure side at this location, while the standard k-ε and SST-k-ω models predict, by default, fully turbulent

boundary layers on all surfaces. The flow detachment by the MILES and k-k_L-ω models caused a decrease in the velocity and thus an increase in C_p.

The differences between models found on the pressure side diminished as the λ^{-1} value increased. For $\lambda^{-1} = 0.108$, the MILES model predicted the value of C_p much closer to the remaining models for the majority of the pressure side. Though they were present to a smaller degree, the small differences found near the trailing edge persisted for this λ^{-1}. This was confirmed by the corresponding contour of RVM (Figure 20). All differences on the pressure side of the airfoil were found to be negligible at $\lambda^{-1} = 0.144$. This was further validated by inspection of RVM (Figure 21). For $\lambda^{-1} = 0.144$ the RVM for each of the models is nearly identical on the pressure side of the airfoil. A small increase in velocity can be seen in the SST-k-ω model though this increase is not large enough to make a considerable difference in the pressure loading.

5.3.2 Suction-Side Coefficient of Pressure

The largest differences in C_p were found on the suction side of the airfoil. The variation of relative velocity magnitude and surface pressure is greater than on the pressure side. For $\lambda^{-1} = 0.072$, the suction side of the blade exhibited the largest difference between models. The SST-k-ω and k-k_L-ω models behaved quantitatively similar on the suction side near the leading edge. The slight difference was found around the halfway point between the leading and trailing edge, roughly at a position of -0.67 (reference fig. 15). At this point the k-k_L-ω model flow detached whereas the SST-k-ω model did not. This is due to the prediction of laminar flow by the k-k_L-ω up to the point of separation. The fully turbulent boundary layer predicted by the SST-k-ω remains attached over the entire surface. Figure 18 shows the point of separation and

reattachment for the k-k_L-ω model. This had an effect on the resultant C_p that was presented as a rapid increase in suction pressure forward and a decrease in pressure at the point of reattachment.

The remaining two models, MILES and standard k-ε, shared a near identical qualitative behavior but dramatically different quantitative behavior. The difference being that the MILES approach predicted larger suction pressures than the standard k-ε model for the majority of the suction side near the leading edge. Figure 17 shows that the MILES approach carries a lower RVM through much more of the suction side than does the standard k-ε model. Durbin (1996) found that the standard k-ε model is known to produce very high levels of turbulence in the leading-edge region of airfoils which reduces the velocity near the surface. The MILES and standard k-ε models lose their qualitative similarities near the trailing edge of the suction side, at a point roughly 90% aft of the leading edge. At this point the MILES and k-k_L-ω model become more similar. Figure 19 confirmed this similarity. At a point aft of the separation bubble for the k-k_L-ω model, the k-k_L-ω model and MILES approach appeared to be near identical.

Similar behavior occurred at $\lambda^{-1} = 0.108$ for each of the models. The only difference observed in comparison to the $\lambda^{-1} = 0.072$ results was that the peak values of the suction pressure were somewhat more pronounced near the leading edge of the airfoil. Similarly, the location of flow separation for the transition-sensitive k-k_L-ω model was moved closer to the leading edge. This was confirmed by inspection of the separation bubble for the k-k_L-ω model in Figures 19 and 21. The location of this bubble was around -0.62 whereas the previous λ^{-1} separation bubble for the k-k_L-ω model was at -0.67. The differences seen between models near the trailing edge for the suction side, specifically the last 10%, were near identical to the differences seen at $\lambda^{-1} = 0.072$.

The greatest qualitative similarities among all the models were found at $\lambda^{-1} = 0.144$. This was due in large part to the behavior of the k-k_L-ω model. At this value of λ^{-1} the separation bubble was not present (see fig. 24). For this reason the k-k_L-ω, MILES, and SST k-ω turbulence models shared a high degree of qualitative and quantitative similarity. The flow around the airfoil for each of these models showed no appreciable differences in terms of relative velocity magnitude (see fig. 23). The standard k-ε model shared a similar qualitative behavior with the remaining three models but it under predicted the suction pressure. As discussed previously, this is believed to be due to the overprediction of turbulent kinetic energy and consequently reduced RVM as shown in fig. 23.

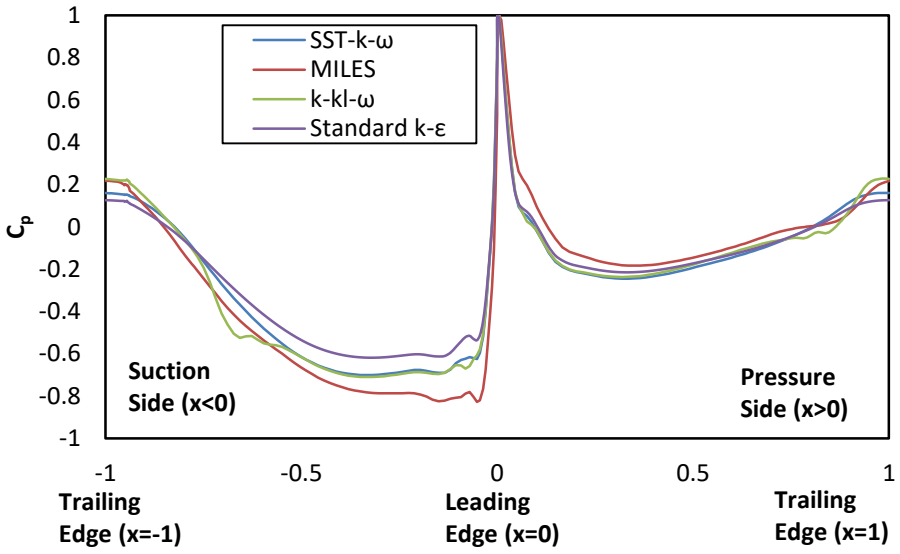

Figure 16: Pressure Coefficient around Airfoil, λ^{-1}=0.072, 90% span

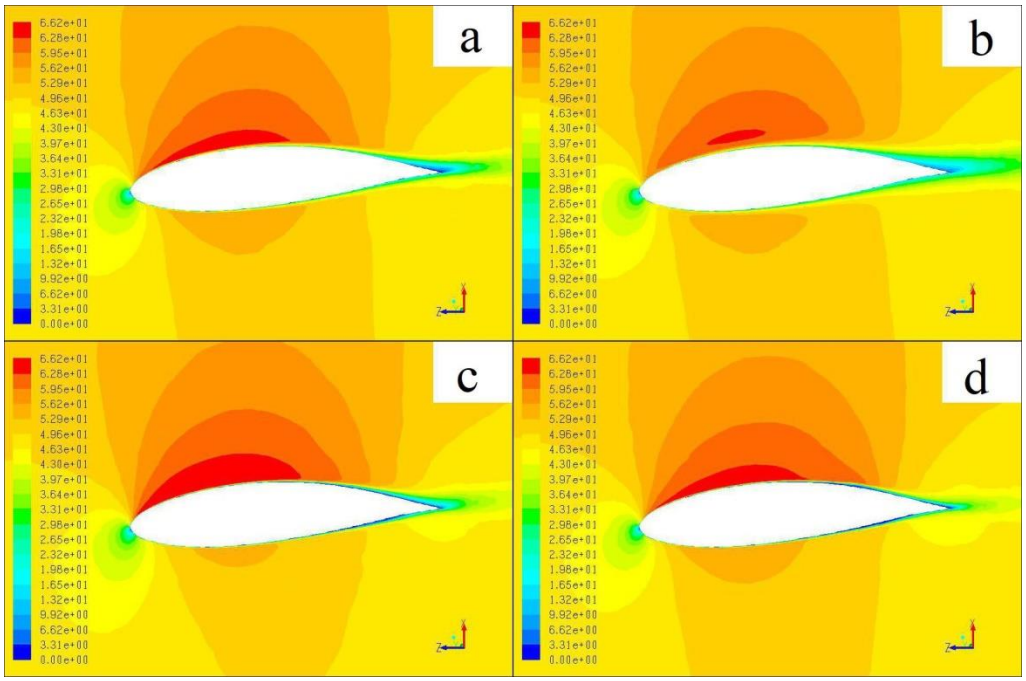

Figure 17: Contours of RVM, λ^{-1}=0.072, 90% span,
(a)SST-k-ω (b) Standard k-ε (c)MILES (d)k-kl-ω

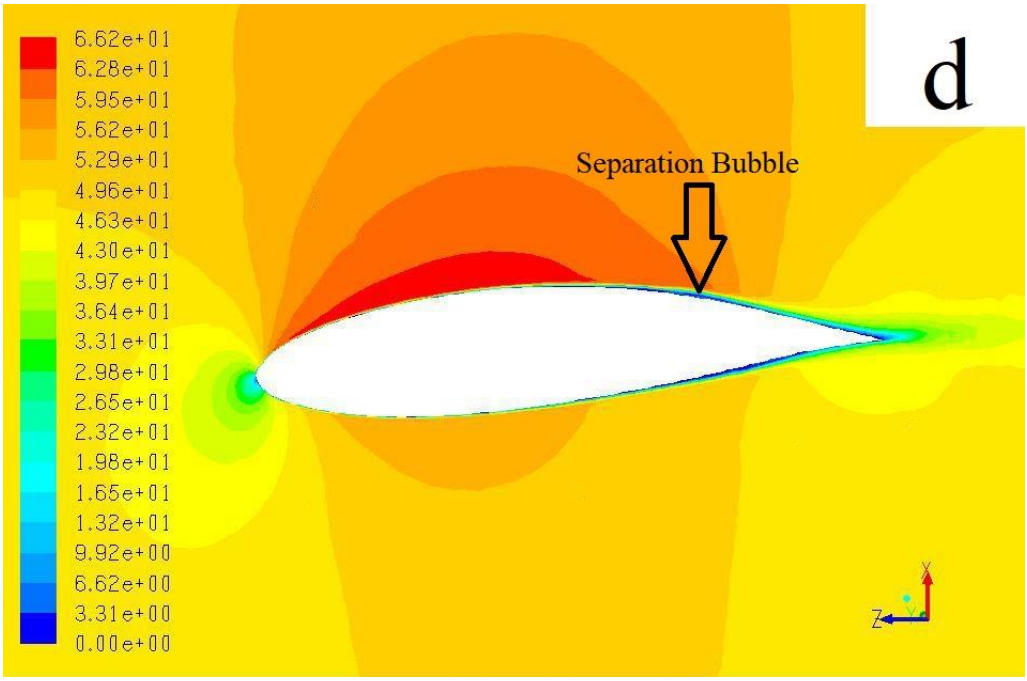

Figure 18: Contour of RVM; λ^{-1}=0.072, 90% span, (d)k-kl-ω

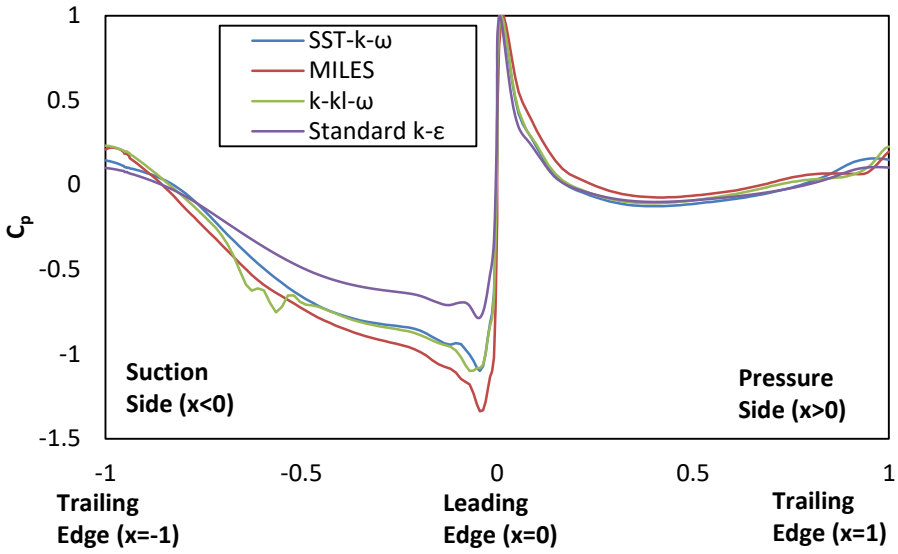

Figure 19: Pressure Coefficient around Airfoil, λ^{-1}=0.108, 90% span

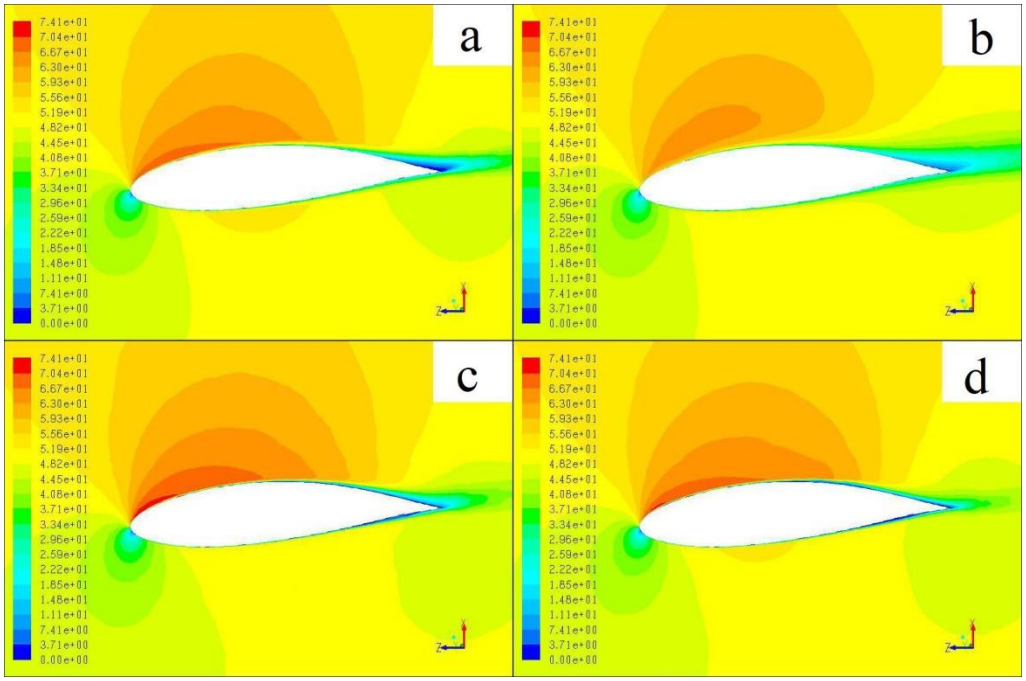

Figure 20: Contours of RVM, λ^{-1}=0.108, 90% span,
(a)SST-k-ω (b) Standard k-ε (c)MILES (d)k-kl-ω

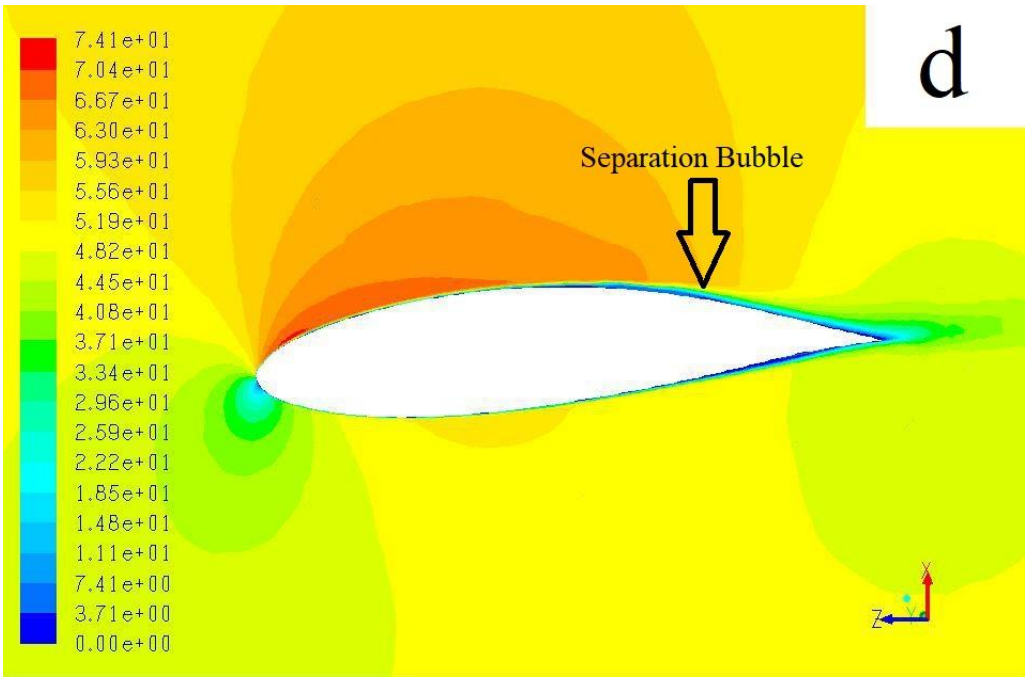

Figure 21: Contour of RVM; λ^{-1}=0.108, 90% span, (d)k-kl-ω

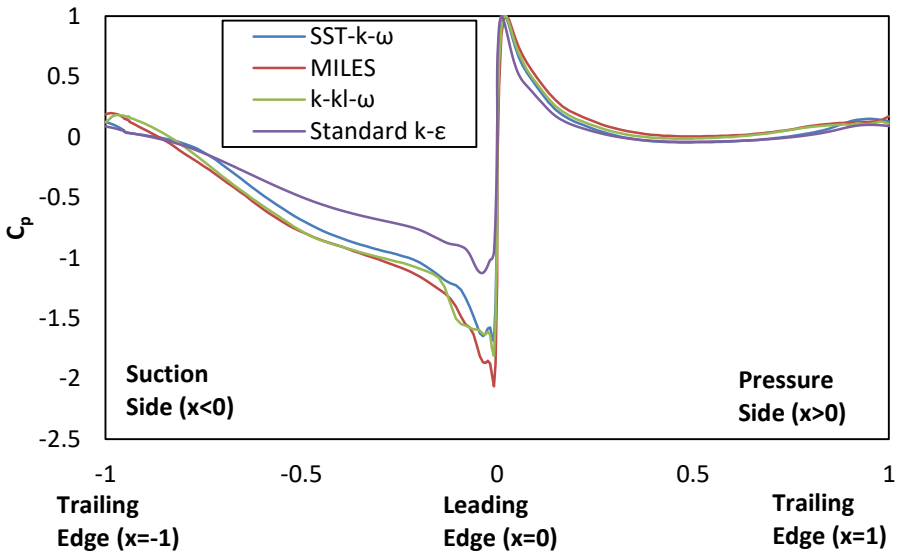

Figure 22: Pressure Coefficient around Airfoil, λ^{-1}=0.144, 90% span

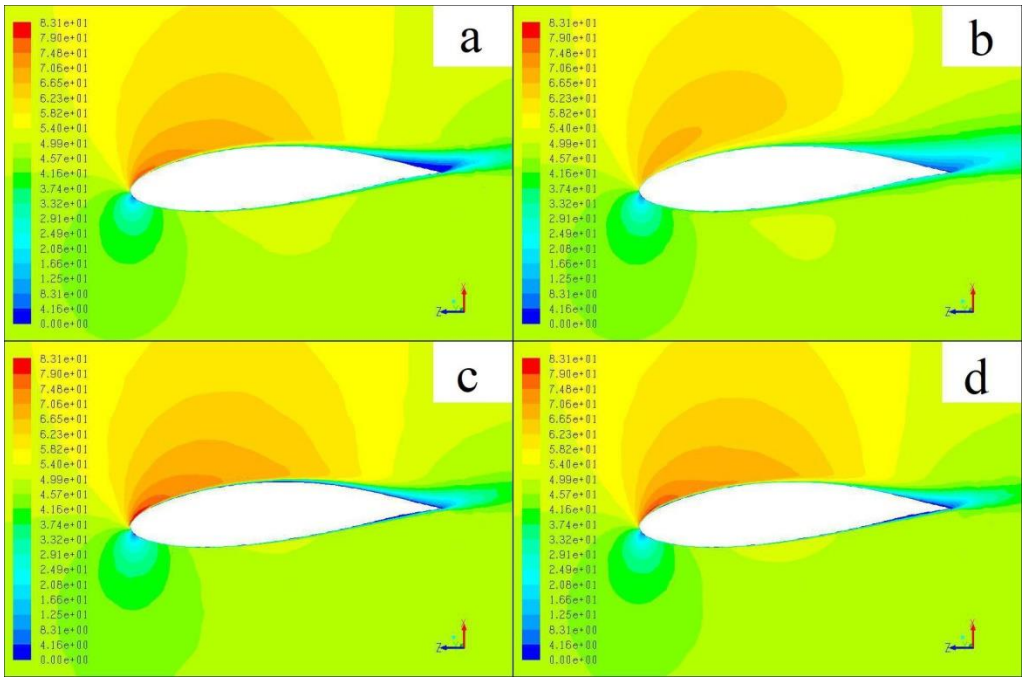

Figure 23: Contours of RVM, λ^{-1}=0.144, 90% span,
(a)SST-k-ω (b) Standard k-ε (c)MILES (d)k-kl-ω

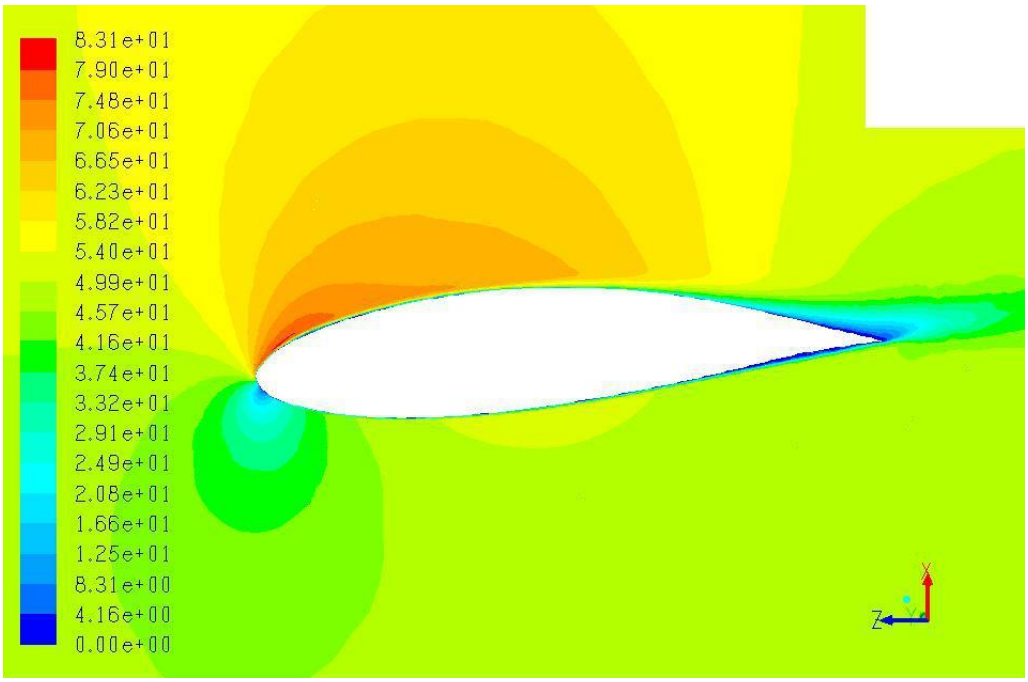

Figure 24: Contour of RVM; λ^{-1}=0.144, 90% span, (d)k-kl-ω

5.4 Skin Friction Coefficient

Another important variable in HAWT studies is C_f. Skin friction coefficient is similar to pressure coefficient in that it quantifies a contribution of force on the airfoil surface. Pressure coefficient is the result of a force being applied to the airfoil in the normal direction. This force typically contributes to the power output of the HAWT. Skin friction coefficient is the result of a force in a direction tangential to the airfoil surface. Consequently, C_f contributes to the drag force the HAWT experiences. This is a detriment to the power output of HAWTs. Skin friction coefficient is the ratio of the local wall shear to the dynamic pressure. For the present study, the skin friction coefficient was defined as

$$C_f = \frac{\tau_w}{\frac{1}{2}\rho U_\infty^2} \tag{20}$$

where τ_w is the wall shear, ρ is air density, and U_∞ is the inlet velocity. Skin friction coefficient, C_f was examined at the same span location, 90% of radial span, as the coefficient of pressure, C_p.

5.4.1 Pressure-Side Skin Friction Coefficient

At $\lambda^{-1} = 0.072$, the k-k_L-ω and MILES models yielded a qualitatively and quantitatively similar result (see fig. 25). This was confirmed by the contour of radial velocity,V_r, for the specified λ^{-1}, shown in figure 26. The slight differences in the predicted values of C_f found near the leading edge were visualized by the contours for each model. Figure 27 showed that the relatively high levels of τ_w for the k-k_L-ω model did not propagate as far downstream from the leading edge as the MILES results did (fig. 28). Interestingly, both of these models show evidence of boundary layer transition, identifiable as a relatively sharp increase in C_f, at a surface location just downstream of -0.7.

The remaining two models, SST-k-ω and standard k-ε, shared a qualitative behavior with the other models. These models behaved similar to one another near the trailing edge of the pressure side while the MILES approach and k-k_L-ω showed erratic behavior near the trailing edge, in the former case due to the unsteady nature of the resolved turbulence, and in the latter case likely due to underlying unsteadiness of the separated flow region. Similar behavior between the models existed for $\lambda^{-1} = 0.180$ (fig. 30 and 31). This behavior also existed for $\lambda^{-1} = 0.324$ with one glaring difference. In the region of increasing C_f near the leading edge the MILES, k-k_L-ω and SST-k-ω predict a quantitatively similar C_f local maximum (fig. 33 and 34). This was a departure from the previous two λ^{-1} where the SST-k-ω over predicted the C_f.

5.4.2 Suction-Side Skin Friction Coefficient

The suction side of the airfoil showed, for $\lambda^{-1} = 0.072$, the k-k_L-ω and MILES turbulence models were very similar in both quantitative and qualitative behavior (fig. 25). A region existed from a position of -0.18 to -0.50 where the models predicted the C_f with good quantitative agreement to each other. This region was where the flow was laminar, hence lacking turbulence, and therefore the prediction of skin friction was very similar. The differences between these models at this λ^{-1} were found near the leading and trailing edges. At both the leading and trailing edge the MILES turbulence model predicted a higher C_f than the k-k_L-ω model. This was a result of the nature of the MILES model and the inability to capture, and accurately model, the small scales of motion. The flow for each of these models transitions from laminar to turbulent around -0.5 and persists through the remaining portion of the blade. Comparison with the C_p results above suggests that for the k-k_L-ω model the transition actually corresponds to boundary layer separation, which is also indicated by the fact that C_f is equal to zero at separation (-0.52) and reattachment points (-0.77). In contrast, the MILES model seems

to indicate transition occurring in the attached boundary layer, most likely triggered by the adverse pressure gradient in that region (see fig. 16).

The standard k-ε and SST-k- ω models shared a qualitative behavior with the other models in a region from -0.18 to -0.50. These models did show turbulent behavior near the trailing edge of the blade, though it was dissimilar to the presentation of turbulence by the k-k_L-ω and MILES turbulence models. The key difference was that these models did not model the same transition, from laminar to turbulent flow, as the MILES and k-k_L-ω models. Both standard k-ε and SST-k- ω models predicted laminar flow for 95% of the suction side. The last 5%, near the trailing edge, was predicted to be turbulent though there was no transition zone. The standard k-ε and SST-k- ω models shared a consistent qualitative behavior throughout the entirety of the suction side. These models were in quantitative agreement near the leading and trailing edges, though the standard k-ε model predicted a higher C_f throughout the majority of the laminar region on the suction side (fig. 30).

Similar behavior was seen for the k-k_L-ω and MILES turbulence models for $\lambda^{-1} = 0.108$ (fig. 30 and 32), though the region of quantitative agreement became smaller, roughly from -0.20 to -0.45. The models were still in qualitative agreement near the leading and trailing edges with the MILES turbulence model predicting a larger C_f. These models, standard k-ε and SST-k- ω, exhibited the same behavior as seen for the previous values of λ^{-1}. At the leading and trailing edges the models were in agreement but between the two the standard k-ε over predicted the C_f. For the MILES and k-k_L-ω models, the turbulent region was slightly larger than the previous λ^{-1}.

A $\lambda^{-1} = 0.144$, the largest differences were seen between models (fig. 33 and 35). The standard k-ε and SST-k- ω predicted the C_f with the same behavior as the previous two values of

λ^{-1}. The difference was seen in the k-k_L-ω and MILES turbulence models. From the leading edge to -0.20, these models were in qualitative agreement. From -0.20 to -0.70 these models did not predict the C_f with any similarity. The k-k_L-ω model predicted an area of increased C_f from -0.25 to -0.70 that reached a maximum at -0.45. This was an area of laminar flow where the flow detached from the blade at -0.19, reattached to the blade at -0.65, then became turbulent from -0.65 to the trailing edge. For the same region from -0.19 to -0.65, the MILES turbulence model predicted the flow to be turbulent. Though the flow was turbulent for this region, the C_f was nearly constant with a slight increase near -0.70. From -0.70 to -0.95 these models shared qualitative agreement and both predicted turbulent flow. From -0.95 to the trailing edge the models were in quantitative agreement.

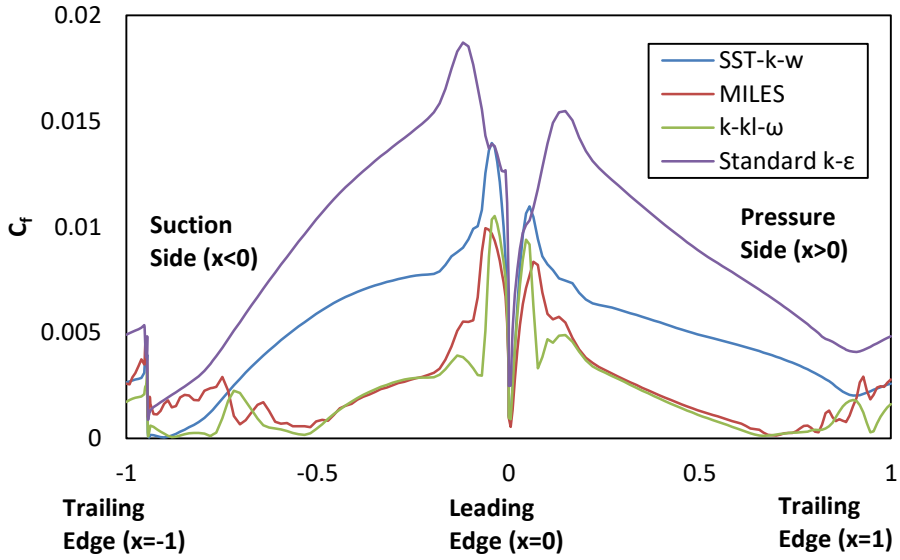

Figure 25: Skin Friction Coefficient around Airfoil, λ^{-1}=0.072, 90% span

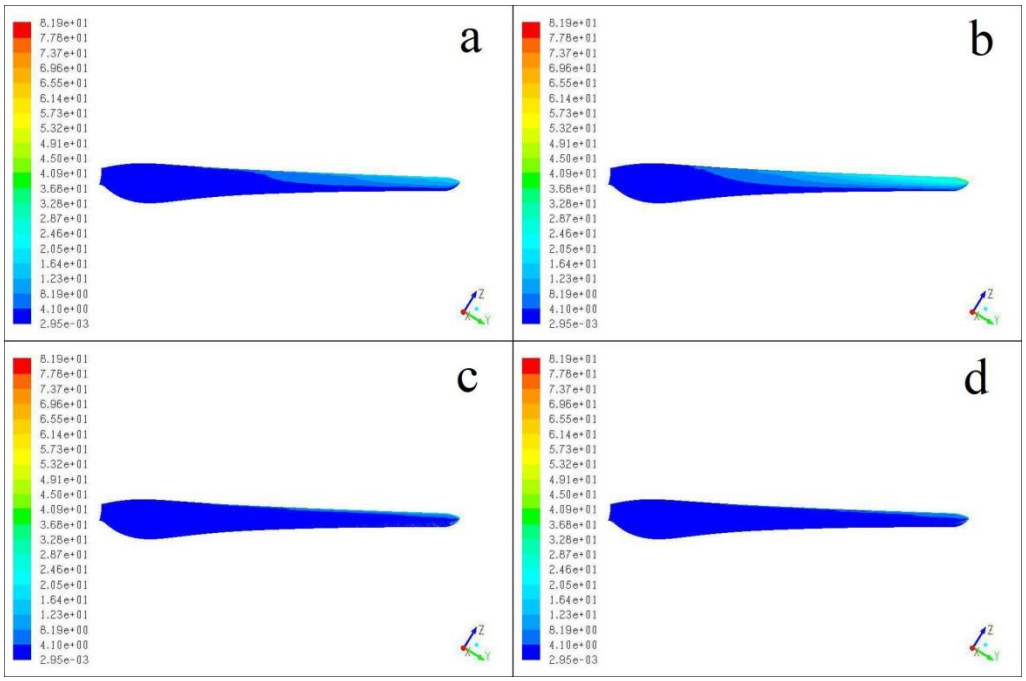

Figure 26: Contours of Wall Shear, Pressure Side, λ^{-1}=0.072,
(a)SST-k-ω (b) Standard k-ε (c)MILES (d)k-kl-ω

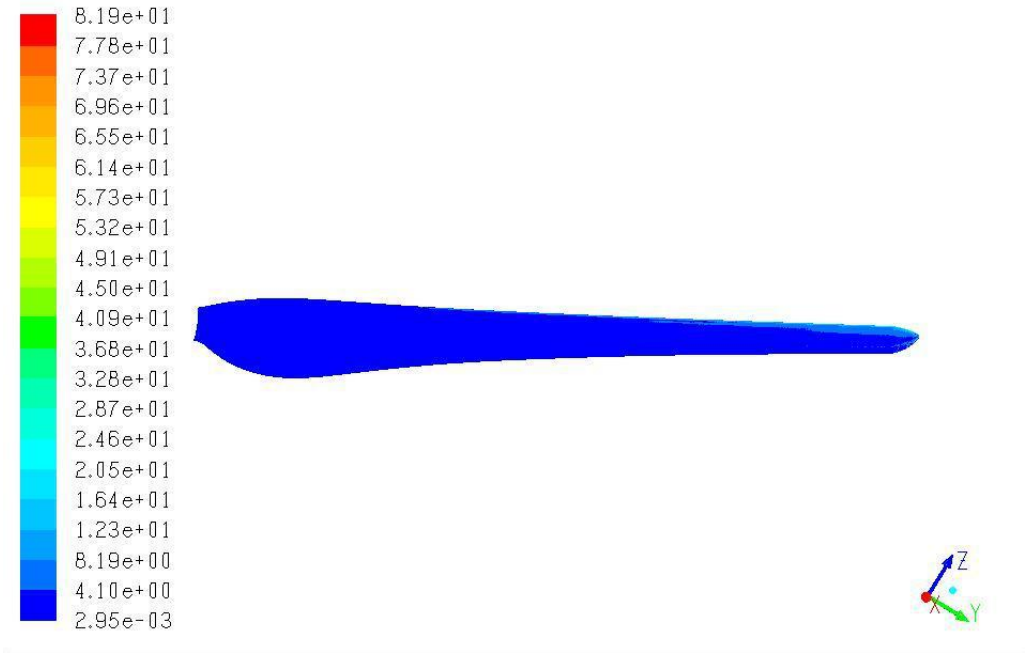

Figure 27: Contours of Wall Shear, Pressure Side, λ^{-1}=0.072, k-kl-ω

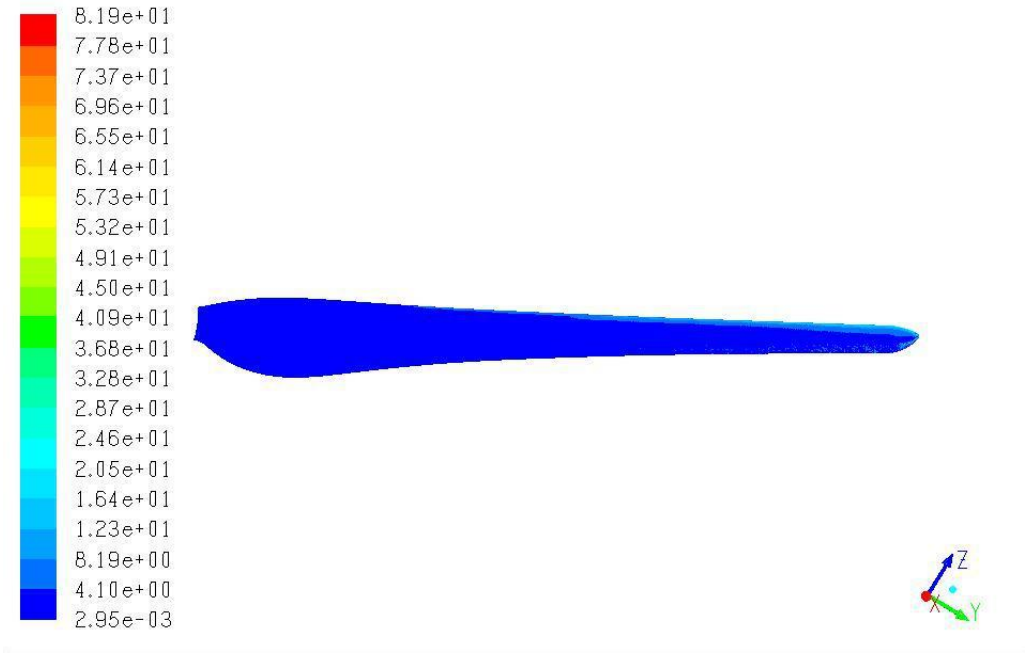

Figure 28: Contours of Wall Shear, Pressure Side, λ^{-1}=0.072, MILES

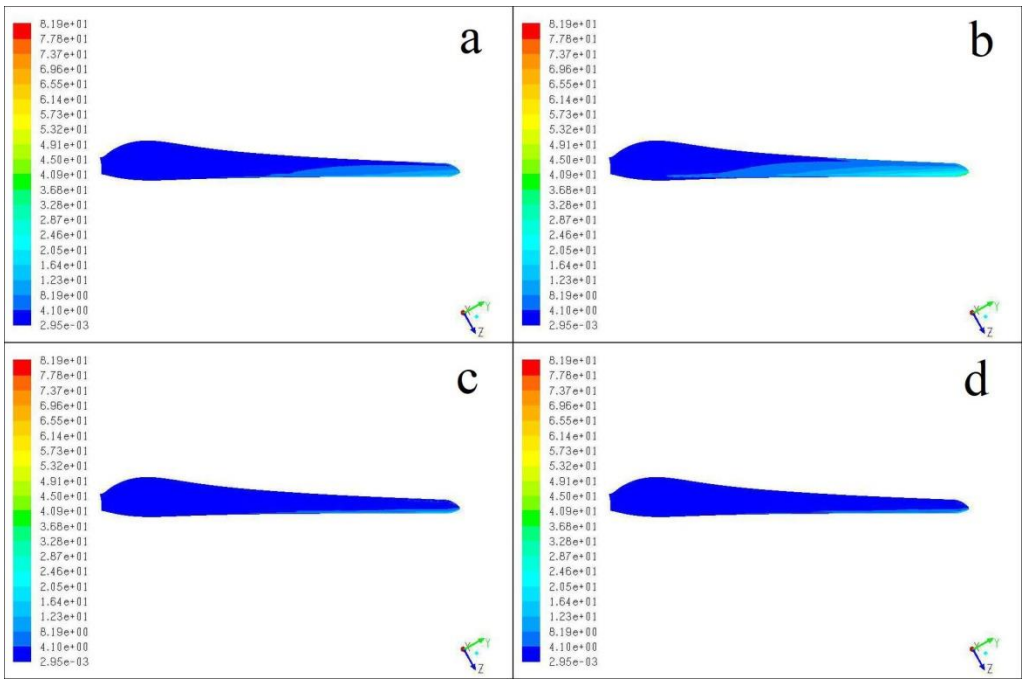

Figure 29: Contours of Wall Shear, Suction Side, λ^{-1}=0.072,
(a)SST-k-ω (b) Standard k-ε (c)MILES (d)k-kl-ω

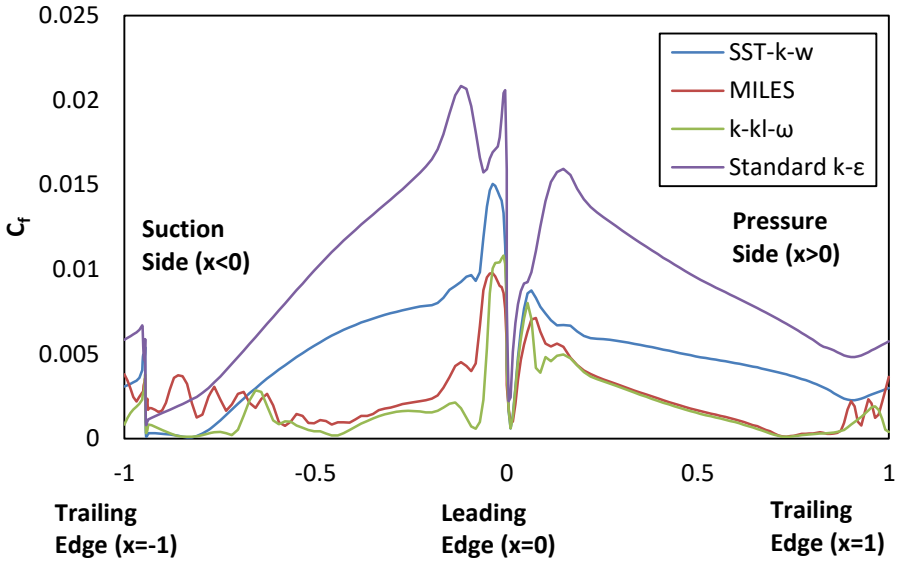

Figure 30: Skin Friction Coefficient around Airfoil, λ^{-1}=0.108, 90% span

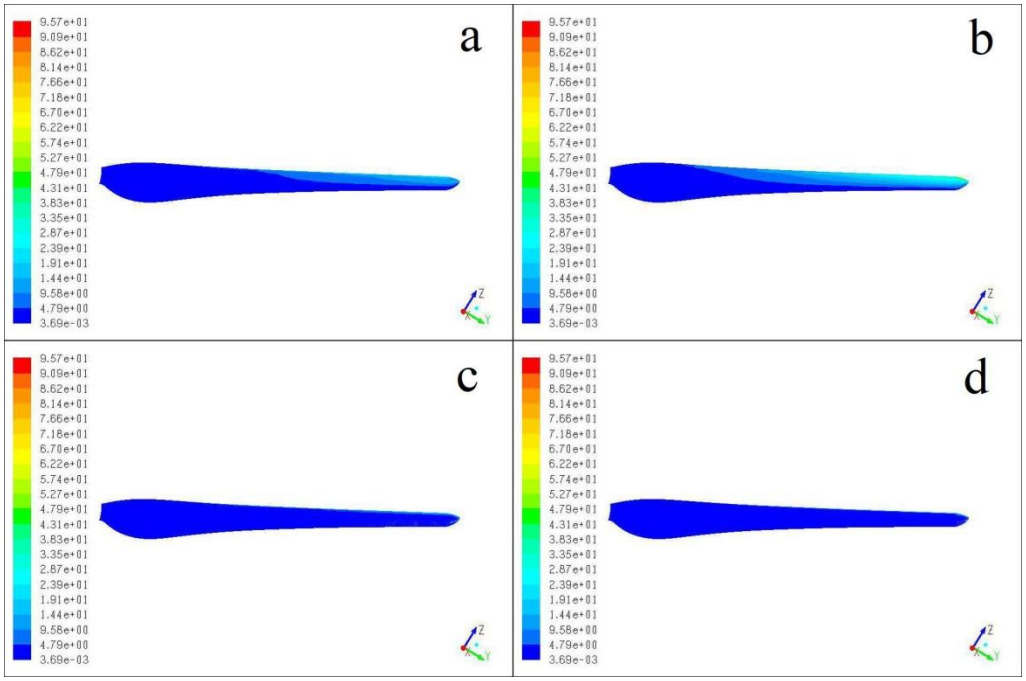

Figure 31: Contours of Wall Shear, Pressure Side, λ^{-1}=0.108,
(a)SST-k-ω (b) Standard k-ε (c)MILES (d)k-kl-ω

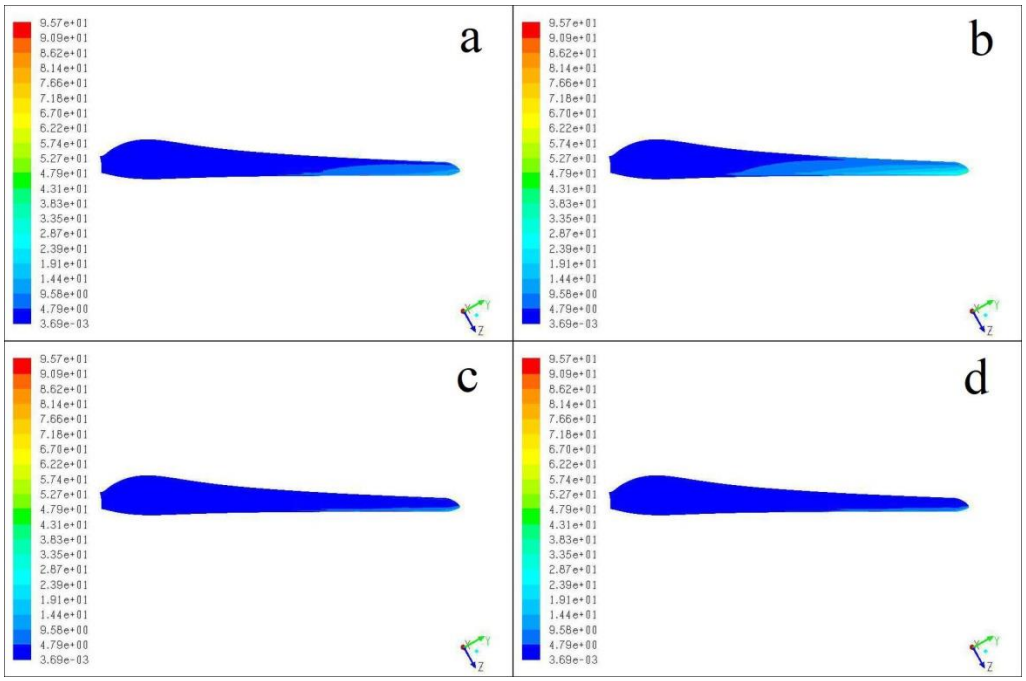

Figure 32: Contours of Wall Shear, Suction Side, λ^{-1}=0.108,
(a)SST-k-ω (b) Standard k-ε (c)MILES (d)k-kl-ω

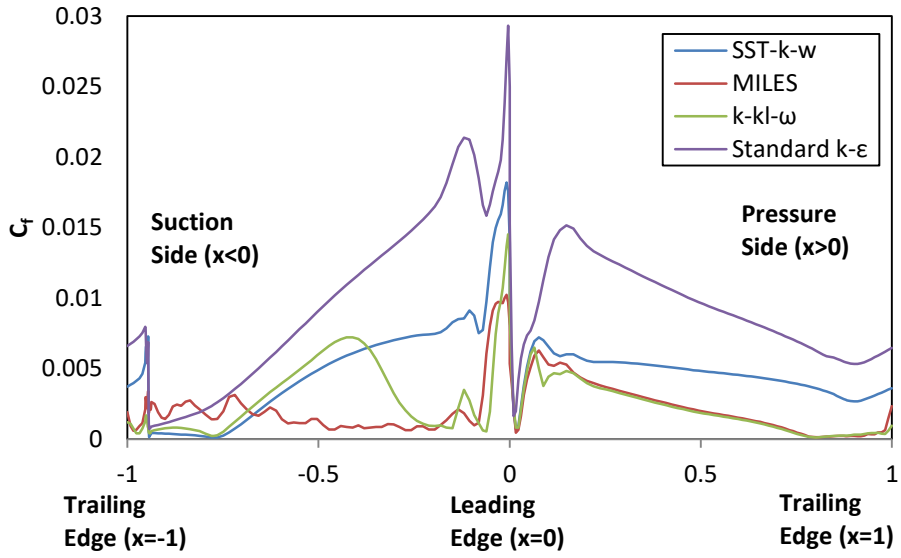

Figure 33: Skin Friction Coefficient around Airfoil, λ^{-1}=0.144, 90% span

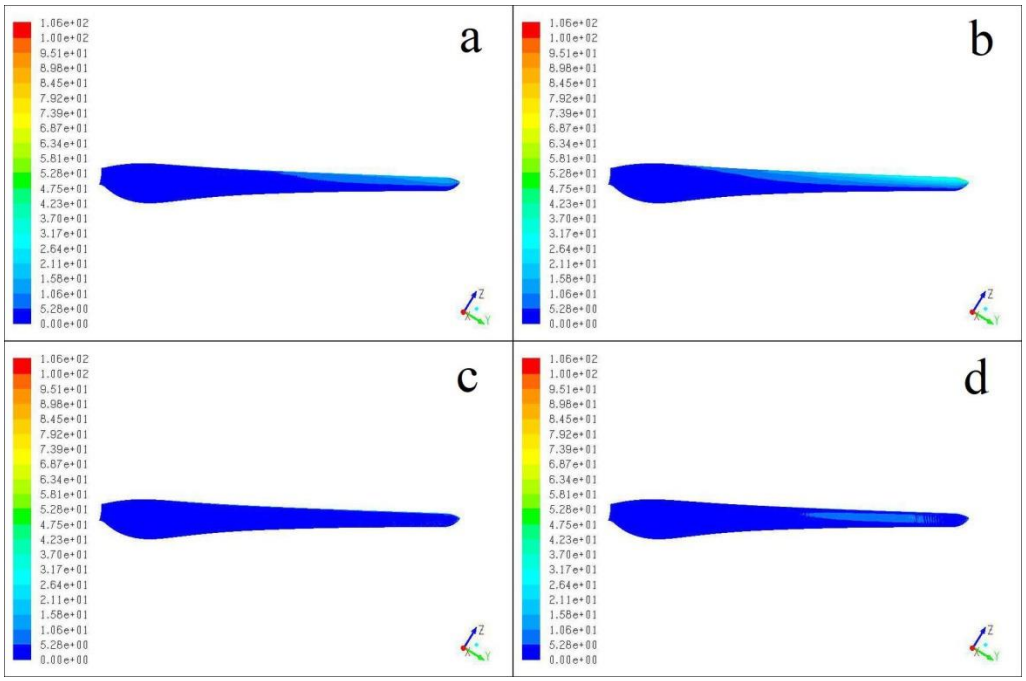

Figure 34: Contours of Wall Shear, Pressure Side, λ^{-1}=0.144,
(a)SST-k-ω (b) Standard k-ε (c)MILES (d)k-kl-ω

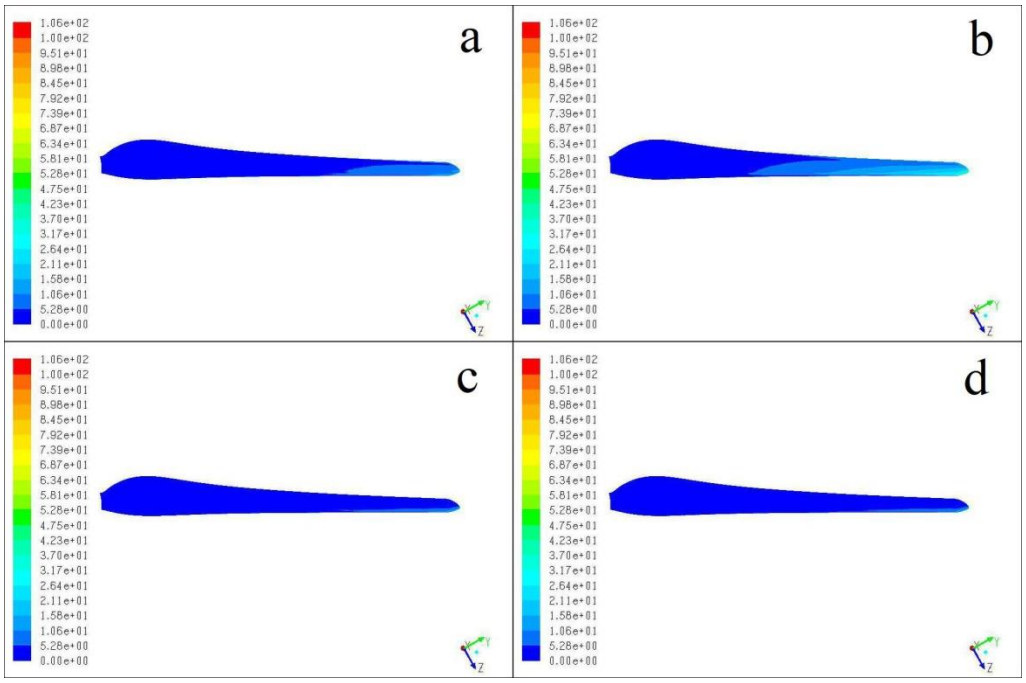

Figure 35: Contours of Wall Shear, Suction Side, λ^{-1}=0.144,
(a)SST-k-ω (b) Standard k-ε (c)MILES (d)k-kl-ω

5.5 Wall Shear Stress Distribution

5.5.1 Suction Side

Wall shear was investigated for $\lambda^{-1} = 0.072, 0.180, 0.324$. Results for all models in the region of the airfoil tip on the suction surface are shown in figs. 36-38. The standard k-ε model predicted the highest shear loading at the tip for all λ^{-1} values. This result was substantially higher than any of the other three models. The high levels of shear stress are again indicative of the increased levels of turbulence that are expected to be predicted in the boundary layer by the standard k-ε model. The SST-k-ω model showed stress levels at the leading edge comparable to the MILES and k-k_L-ω models but higher levels over the majority of the surface. This is due to the fact that the SST-k-ω model predicts a fully turbulent boundary layer and does not resolve transition from laminar to turbulent. The MILES and k-k_L-ω turbulence models show the lowest levels of shear stress due to their ability to predict both laminar and turbulent flow regions. They also show some level of unsteadiness, visible as patchy regions of higher shear stress. For the MILES model, the flow is shear stress distribution is quite patchy and unsteady since any turbulence in the flow appears as fluctuating velocity which in turns yields fluctuating shear stress on the wall.

As the value of λ^{-1} increased, the relative behavior of the models did not change significantly. Effectively, the angle of attack of the airfoil also increased and the region of high shear stress moved closer to the leading edge. For the midrange value $\lambda^{-1} = 0.180$, the flow is predicted to be separated by the MILES and k-k_L-ω models, since the laminar boundary layer tends to separate more readily under adverse pressure gradient. At the highest value of λ^{-1}, the flow appears to be separated for all models except for standard k-ε. The delay in separation for

the standard k-ε is due to the prediction of high turbulence, and helps to explain the late prediction of stall indicated in the power performance plots (fig. 10).

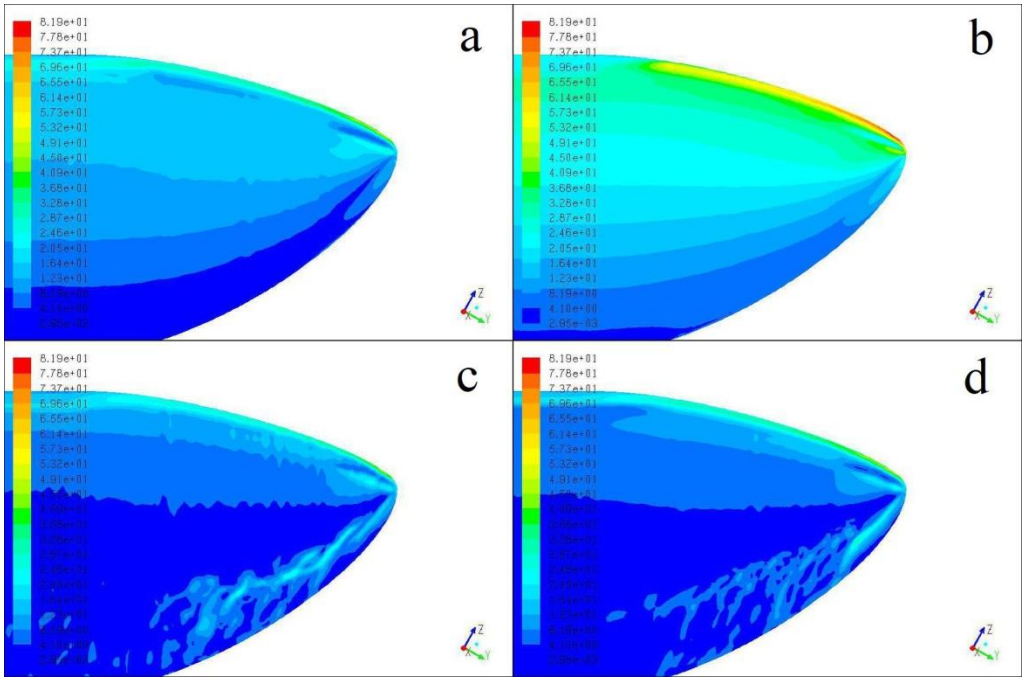

Figure 36: Contours of Wall Shear Near Blade Tip, Suction Side, λ^{-1}=0.072, (a)SST-k-ω (b) Standard k-ε (c)MILES (d)k-kl-ω

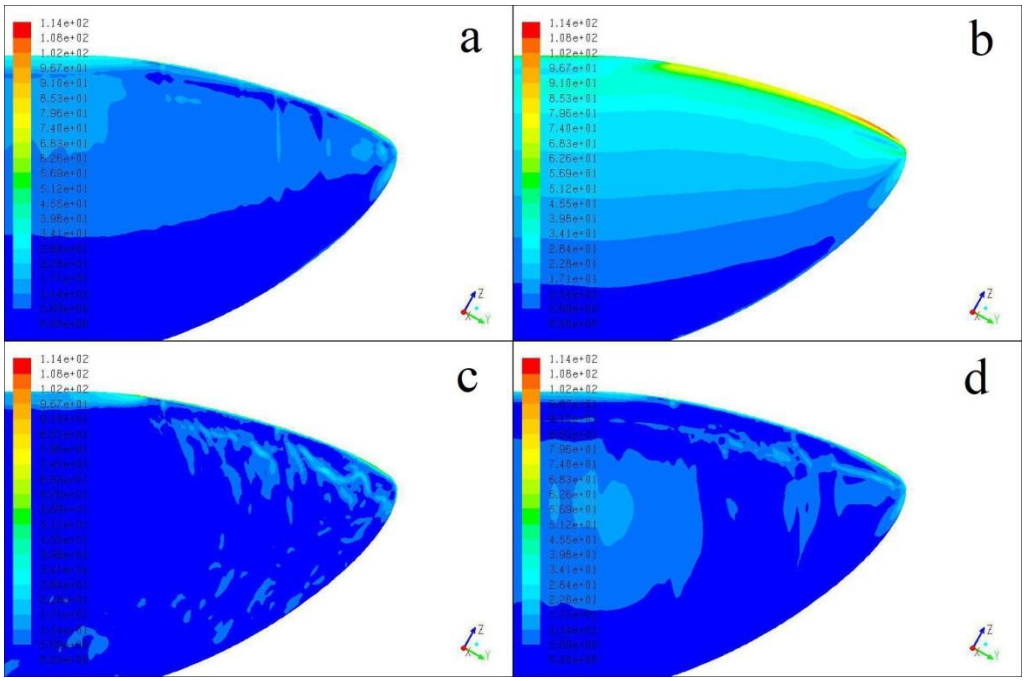

Figure 37: Contours of Wall Shear Near Blade Tip, Suction Side, λ^{-1}=0.180, (a)SST-k-ω (b) Standard k-ε (c)MILES (d)k-kl-ω

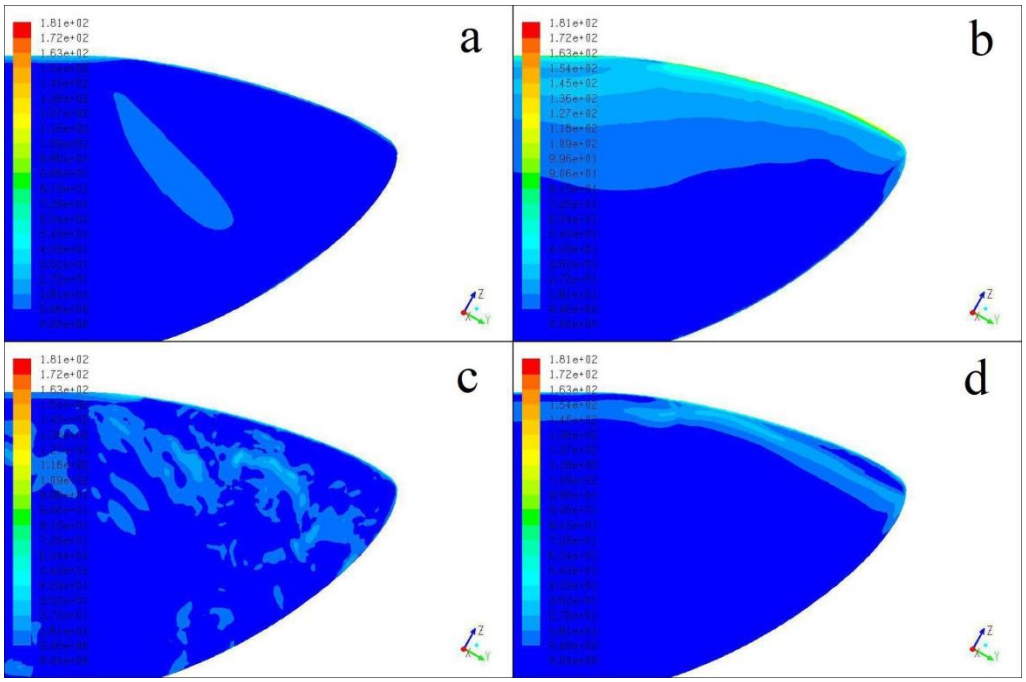

Figure 38: Contours of Wall Shear Near Blade Tip, Suction Side, λ^{-1}=0.324, (a)SST-k-ω (b) Standard k-ε (c)MILES (d)k-kl-ω

5.5.2 Pressure Side

The pressure side of the blade for $\lambda^{-1} = 0.072$ showed that the standard k-ε and SST-k-ω models again predicted clearly defined areas of high shear. This was likely due to the inherent prediction of fully turbulent flow for these models. The MILES and k-k_L-ω models predicted regions of shear similar to one another. This value of λ^{-1} accounted for the largest difference between the modeling of τ_w between turbulence models (fig. 39). When looking at $\lambda^{-1} = 0.180$ the model $\tau_w$was predicted in a similar manner as the previous λ^{-1} (fig. 40). At $\lambda^{-1} = 0.324$ (fig. 41) the SST-k-ω and standard k-ε models predicted wall shear very similarly. The same qualitative behavior between models was shared while the standard k-ε over predicted the value of τ_w. This was again likely due to the over prediction of turbulence at the stagnation point (further discussed in the section below on turbulent kinetic energy). The remaining turbulence models, MILES and k-k_L-ω, were very closely related. Each model exhibited a nearly identical contour for τ_w near the tip (fig. 39 c and d). The only slight difference that existed was that the k-k_L-ω results showed a clearly defined area of shear while the MILES turbulence model was unable to capture a clearly defined area. Again, this is directly related to the differences the MILES and k-k_L-ω models had in modeling C_p and C_f.

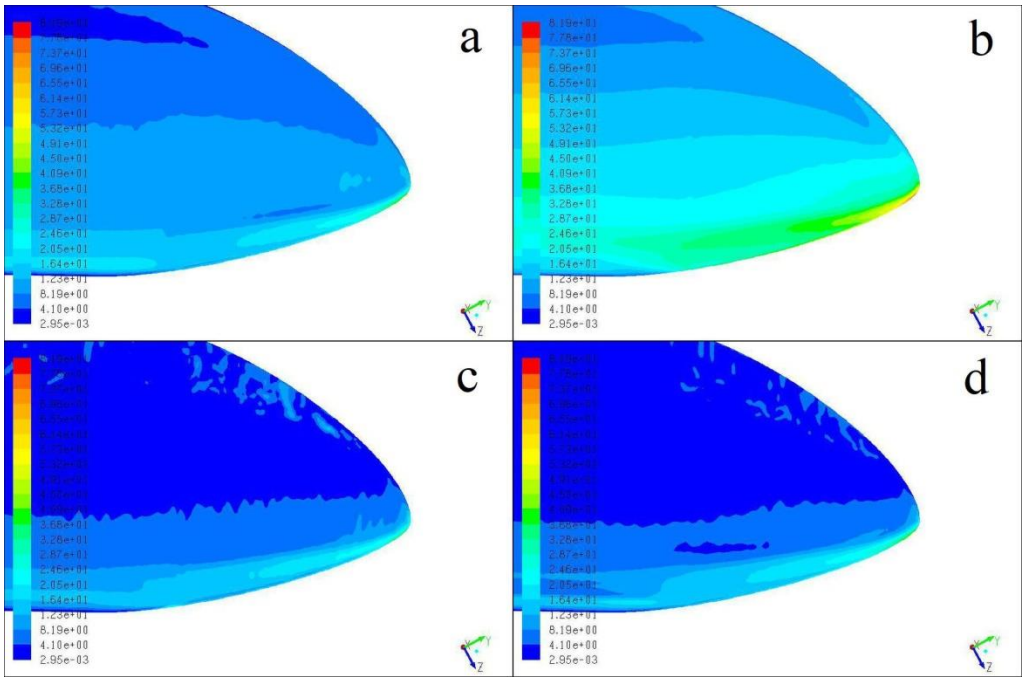

Figure 39: Contours of Wall Shear Near Blade Tip, Pressure Side, λ^{-1}=0.072, (a)SST-k-ω (b) Standard k-ε (c)MILES (d)k-kl-ω

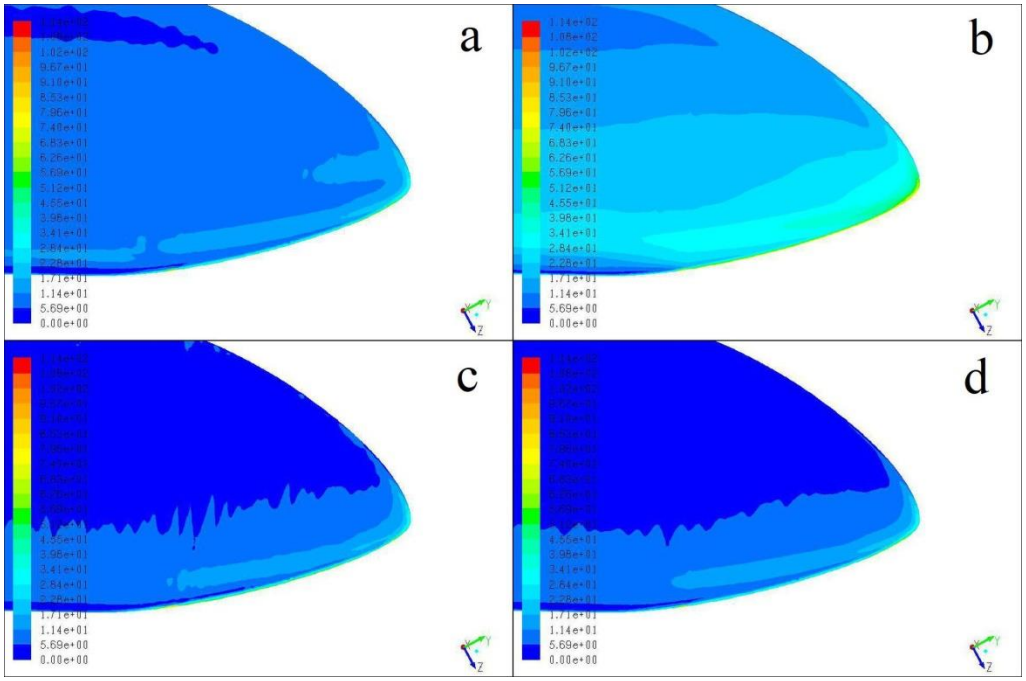

Figure 40: Contours of Wall Shear Near Blade Tip, Pressure Side, λ^{-1}=0.180, (a)SST-k-ω (b) Standard k-ε (c)MILES (d)k-kl-ω

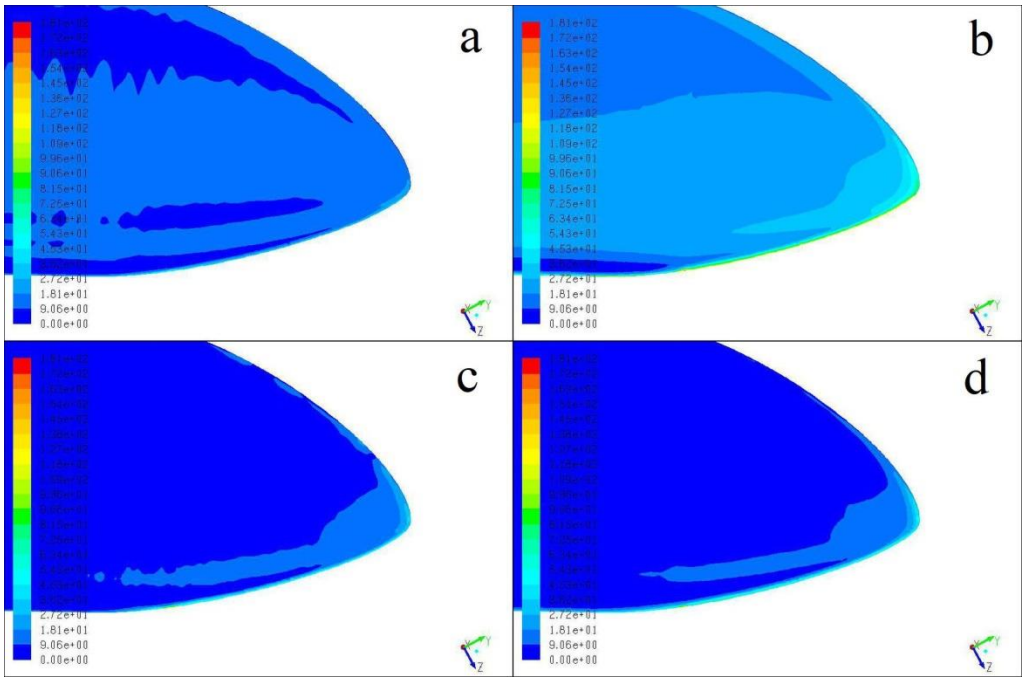

Figure 41: Contours of Wall Shear Near Blade Tip, Pressure Side, λ^{-1}=0.324, (a)SST-k-ω (b) Standard k-ε (c)MILES (d)k-kl-ω

5.6 Radial Velocity

Radial velocity (V_r) in HAWTs is the velocity component of flow from the root of the blade outward toward the tip. Micallef et al. (2012) observed that complex behaviors of V_r occurred at the root and tip. These behaviors were seen at various λ^{-1} and span locations and are presented below.

The V_r for $\lambda^{-1} = 0.072$ for five span wise locations; 25%, 33%, 50%, 75%, 90%; was examined (figs. 42, 44, 46, 47, 50). At this value of λ^{-1} the SST-k-ω and standard k-ε models showed no complex radial flow for all span wise locations. This was not the case for the MILES and k-k_L-ω models. The MILES turbulence model predicted complex V_r behavior near the tip at span wise locations of 75% and 90% (figs. 48 and 51). The k-k_L-ω model predicted complex V_r near both the root and the tip at span wise locations of 25%, 33%, 75% and 90% (figs. 43, 45, 49, and 52). The only span wise location where this behavior was not predicted was at 50% span.

While both k-k_L-ω and MILES turbulence models predicted V_r at 75% and 90% span, the presentation of V_r differed. At both span locations the MILES turbulence model predicted a thin layer of V_r that was located close to the airfoil surface. Radial velocity was predicted on the suction side only at 75% span and both sides of the airfoil at 90% span. The k-k_L-ω model predicted a V_r at these locations that was beginning to detach and separate itself from the airfoil surface. This flow was seen on both the suction and pressure sides for both span wise locations.

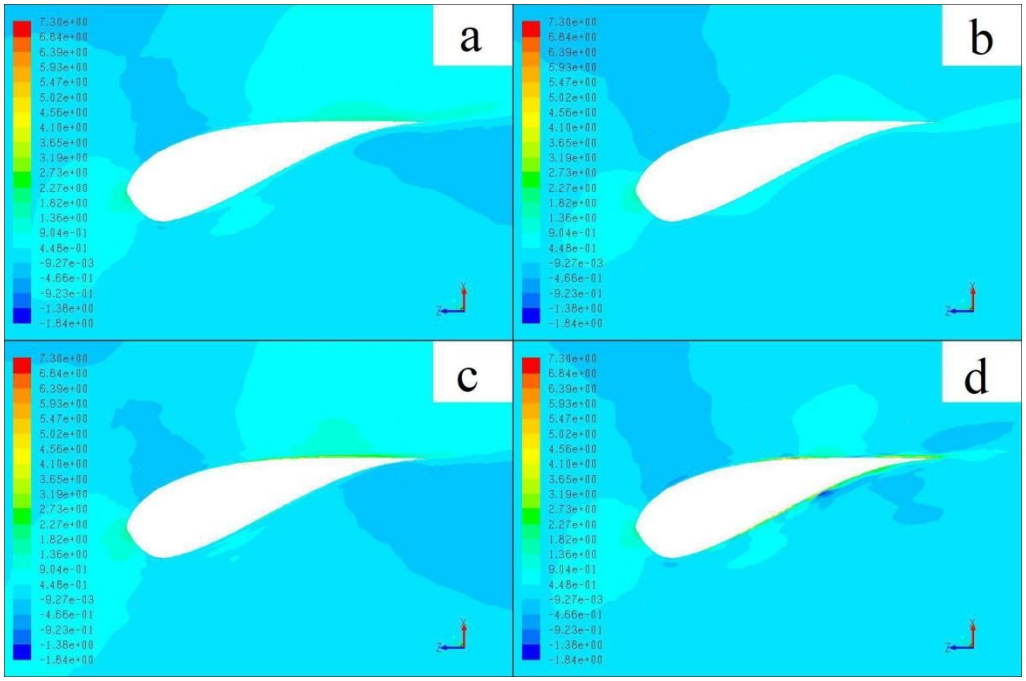

Figure 42: Contours of Radial Velocity, λ^{-1}=0.072, 25% span,
(a)SST-k-ω (b) Standard k-ε (c)MILES (d)k-kl-ω

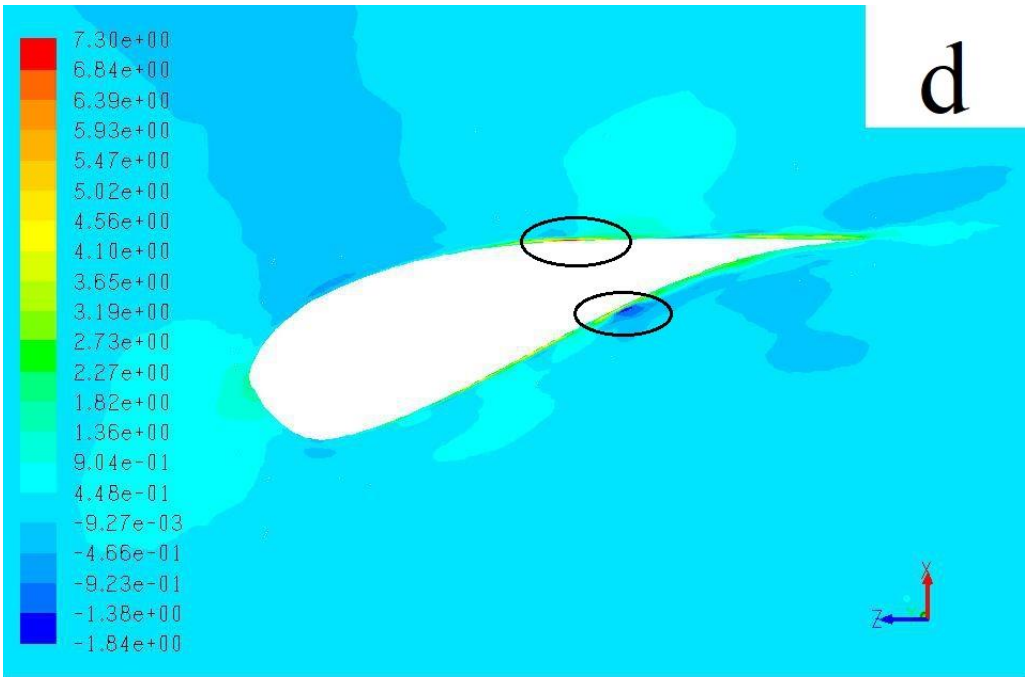

Figure 43: Contours of Radial Velocity, λ^{-1}=0.072, 25% span, (d) k-kl-ω

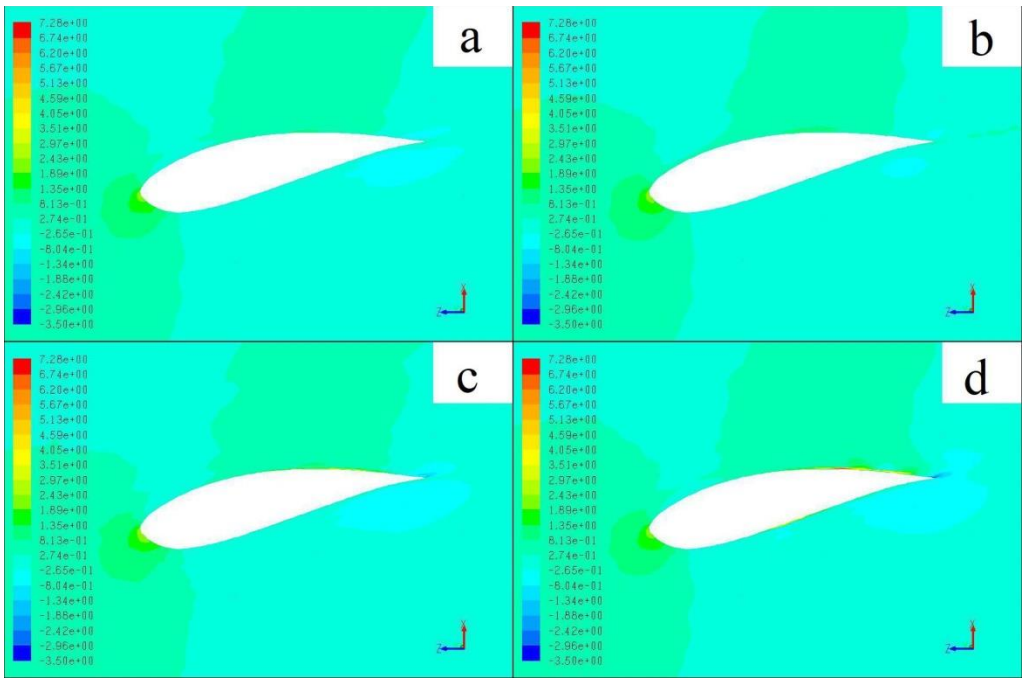

Figure 44: Contours of Radial Velocity, λ^{-1}=0.072, 33% span,
(a)SST-k-ω (b) Standard k-ε (c)MILES (d)k-kl-ω

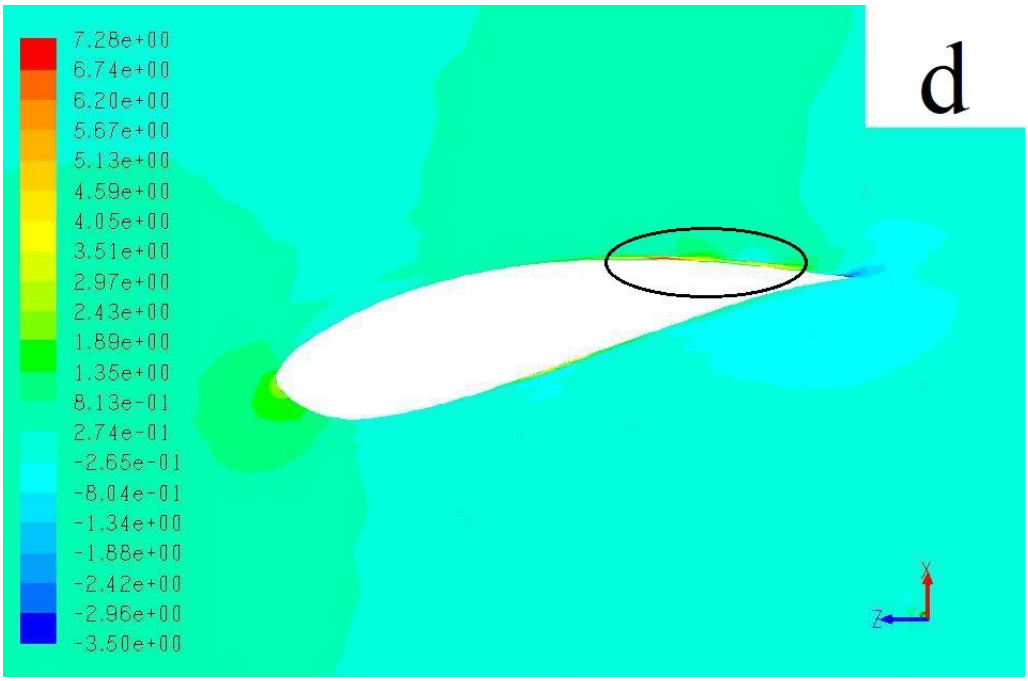

Figure 45: Contours of Radial Velocity, λ^{-1}=0.072, 33% span, (d) k-kl-ω

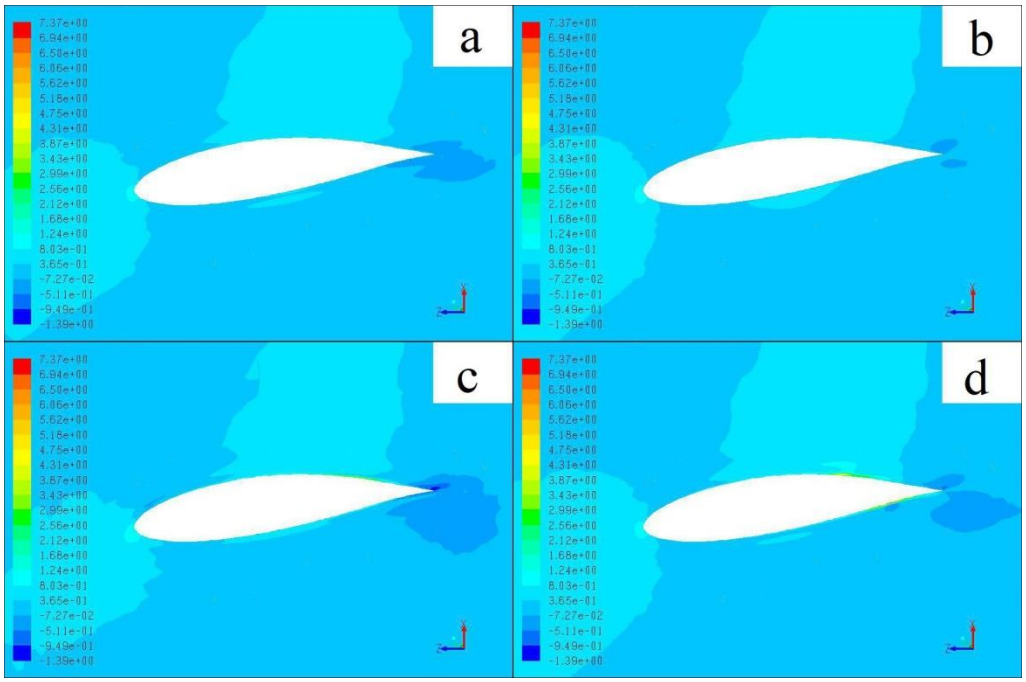

Figure 46: Contours of Radial Velocity, λ^{-1}=0.072, 50% span,
(a)SST-k-ω (b) Standard k-ε (c)MILES (d)k-kl-ω

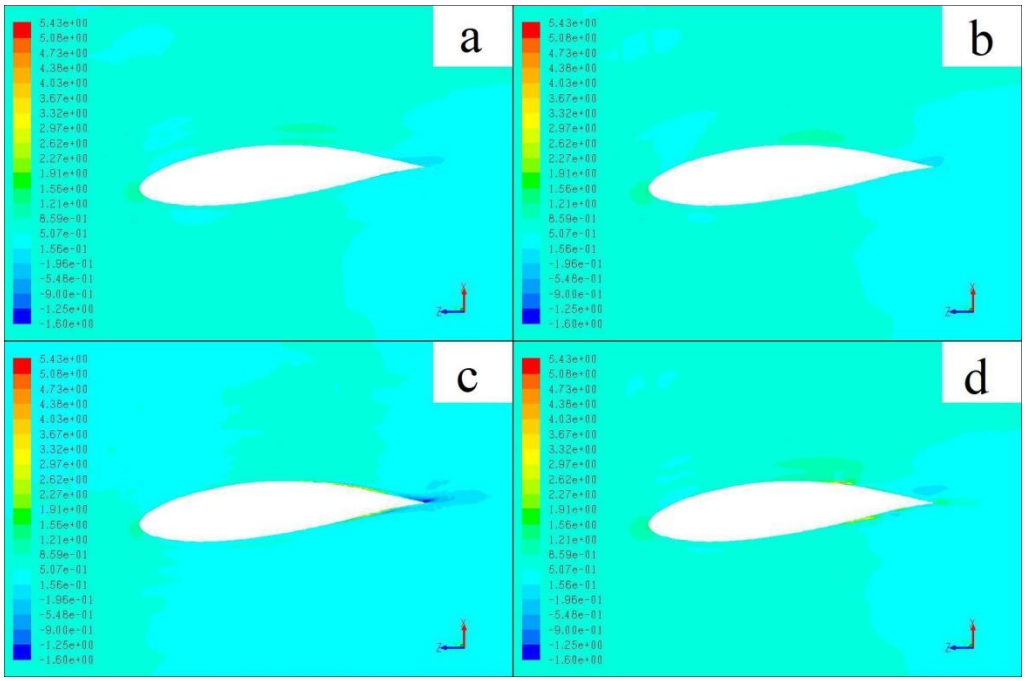

Figure 47: Contours of Radial Velocity, λ^{-1}=0.072, 75% span,
(a)SST-k-ω (b) Standard k-ε (c)MILES (d)k-kl-ω

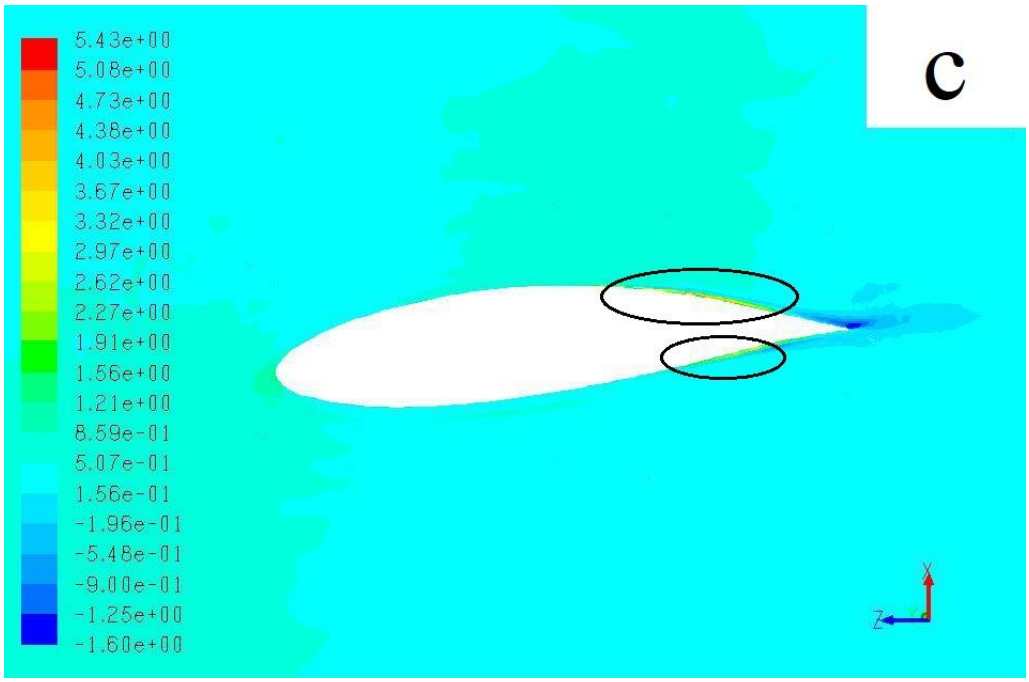

Figure 48: Contours of Radial Velocity, λ^{-1}=0.072, 75% span, (c)MILES

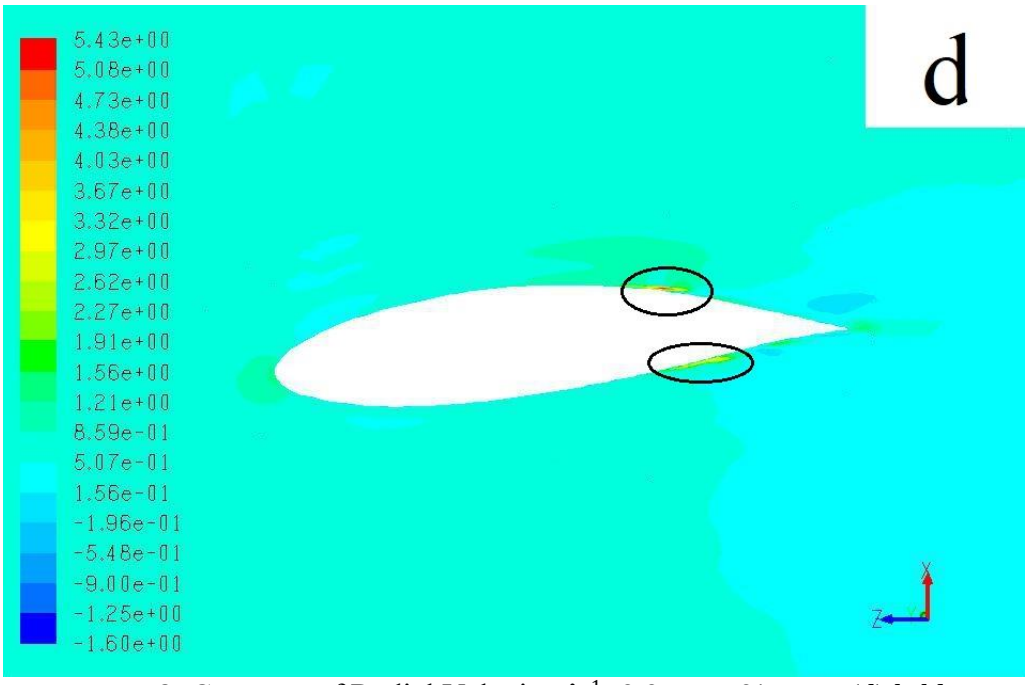

Figure 49: Contours of Radial Velocity, λ^{-1}=0.072, 75% span, (d) k-kl-ω

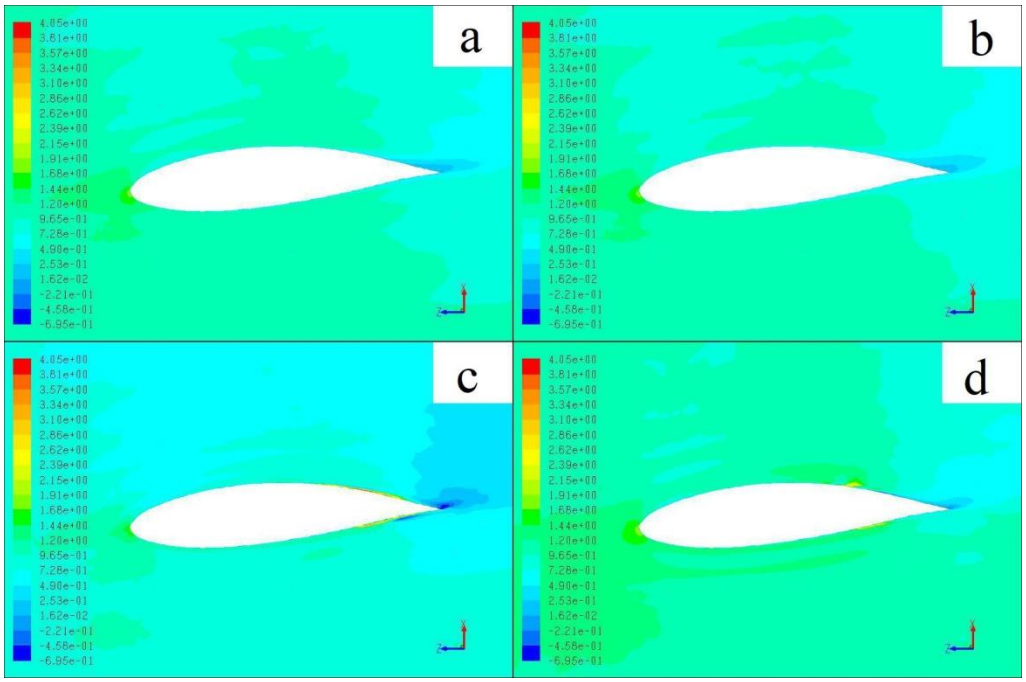

Figure 50: Contours of Radial Velocity, λ^{-1}=0.072, 90% span,
(a)SST-k-ω (b) Standard k-ε (c)MILES (d)k-kl-ω

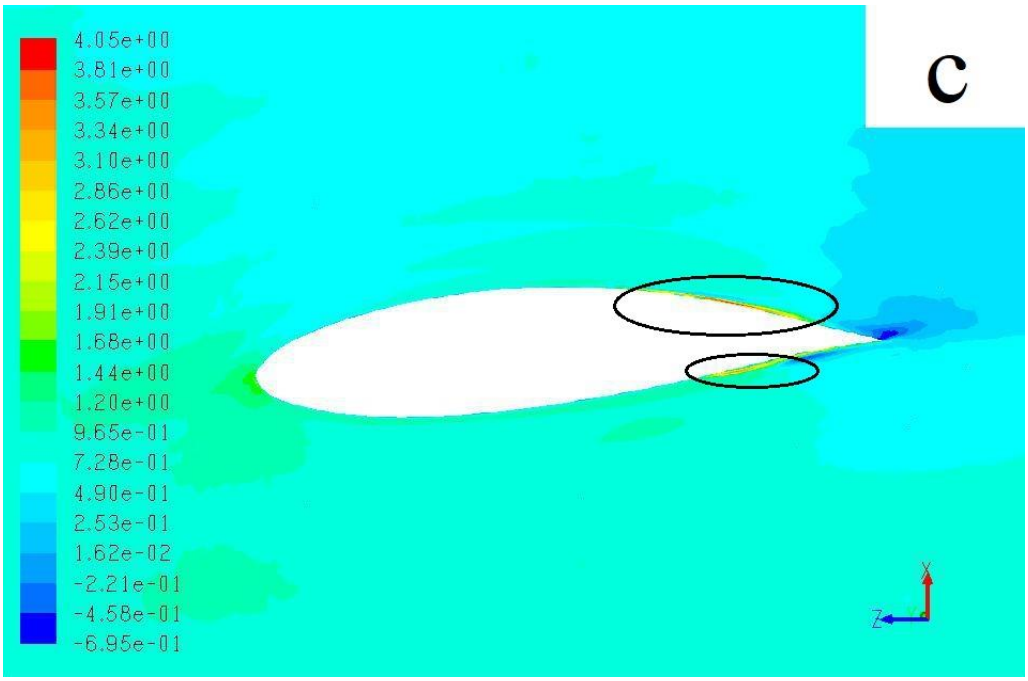

Figure 51: Contours of Radial Velocity, λ^{-1}=0.072, 90% span, (c) MILES

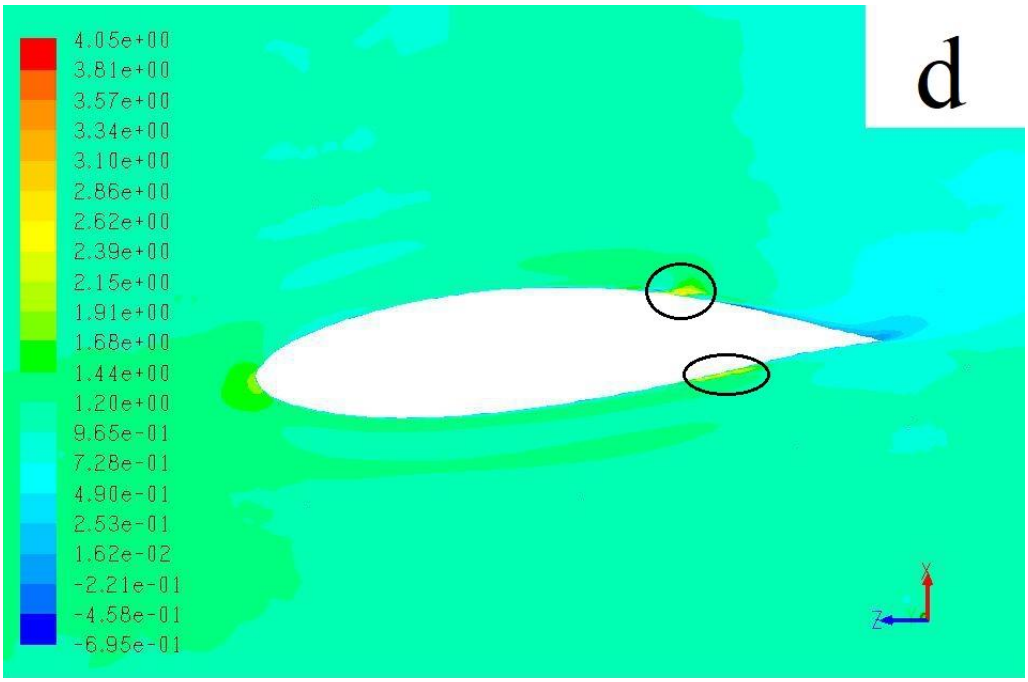

Figure 52: Contours of Radial Velocity, λ^{-1}=0.072, 90% span, (d) k-kl-ω

The differences between models for $\lambda^{-1} = 0.180$ were not as subtle as those seen for$\lambda^{-1} = 0.072$. The SST-k-ω model predicted a much higher V_r on the suction side through all span wise locations (figs 52-56) with the exception coming at 90% span (fig. 57). At 25% and 50% span the standard k-ε model predicted a similar V_r. The major difference for these locations was that the standard k-ε prediction was small in magnitude and located closer to the trailing edge than that of the SST-k-ω prediction. The remaining span wise locations provided no consistent results between models. Finally, the MILES turbulence model yielded an anomalous result. At 90% span, a small area of increased V_r was found near the leading edge (fig. 58) . This result was not found with any other method at any span wise location for $\lambda^{-1} = 0.180$.

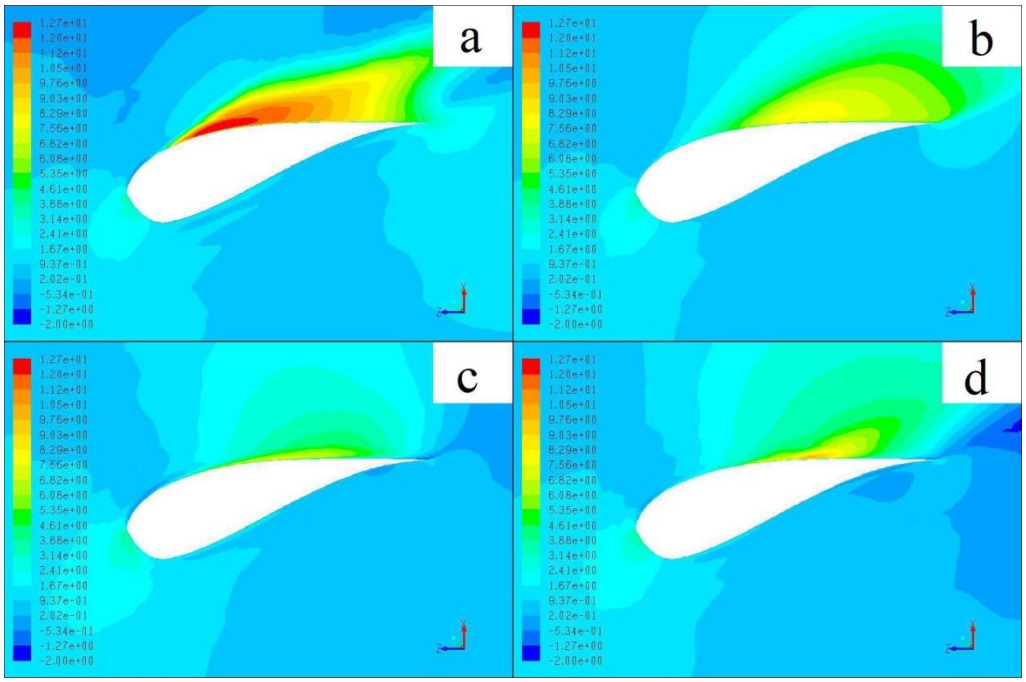

Figure 53: Contours of Radial Velocity, λ^{-1}=0.180, 25% span,
(a)SST-k-ω (b) Standard k-ε (c)MILES (d)k-kl-ω

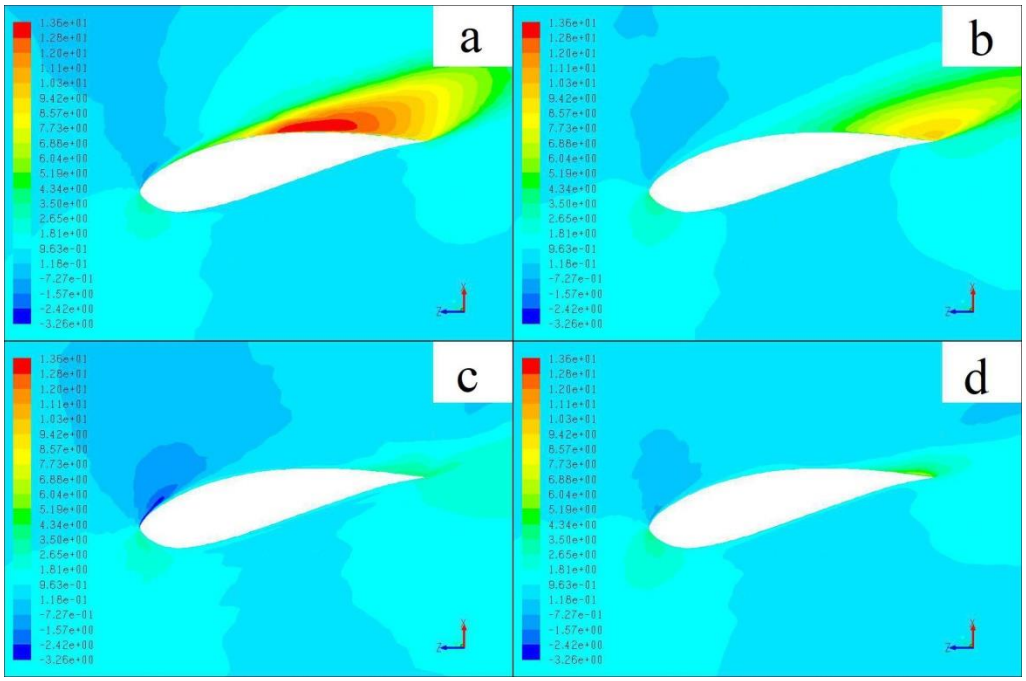

Figure 54: Contours of Radial Velocity, λ^{-1}=0.180, 33% span,
(a)SST-k-ω (b) Standard k-ε (c)MILES (d)k-kl-ω

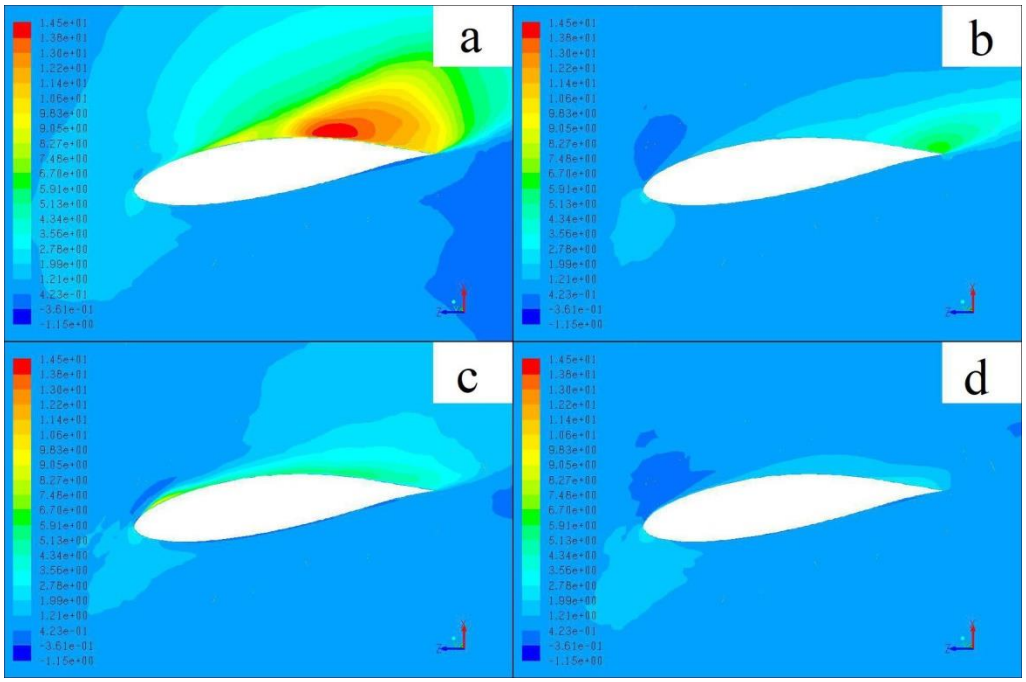

Figure 55: Contours of Radial Velocity, λ^{-1}=0.180, 50% span,
(a)SST-k-ω (b) Standard k-ε (c)MILES (d)k-kl-ω

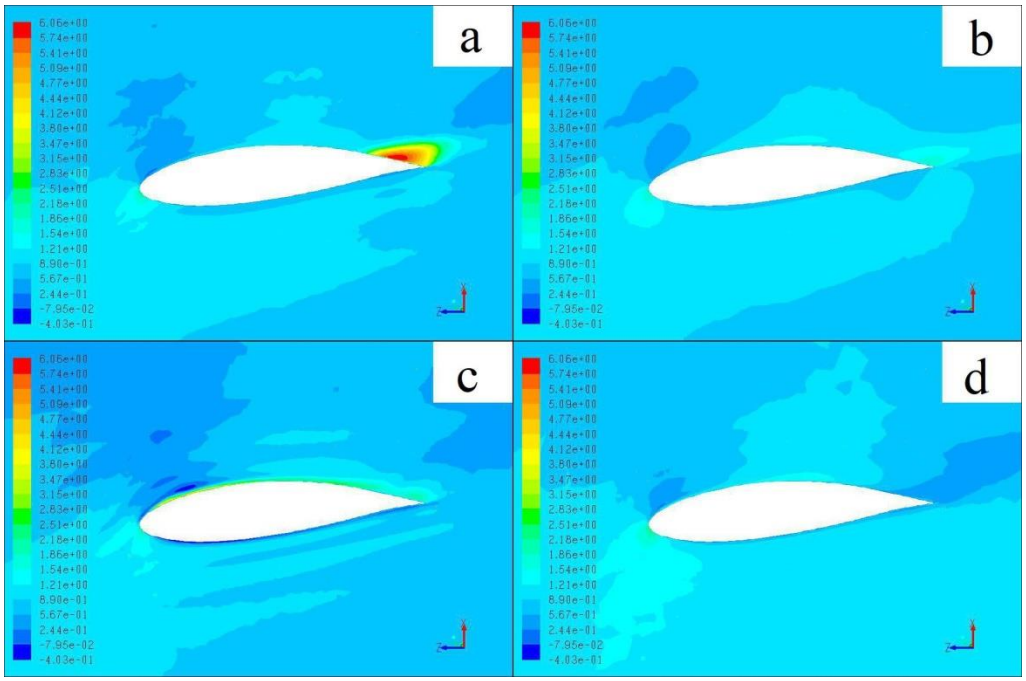

Figure 56: Contours of Radial Velocity, λ^{-1}=0.180, 75% span,
(a)SST-k-ω (b) Standard k-ε (c)MILES (d)k-kl-ω

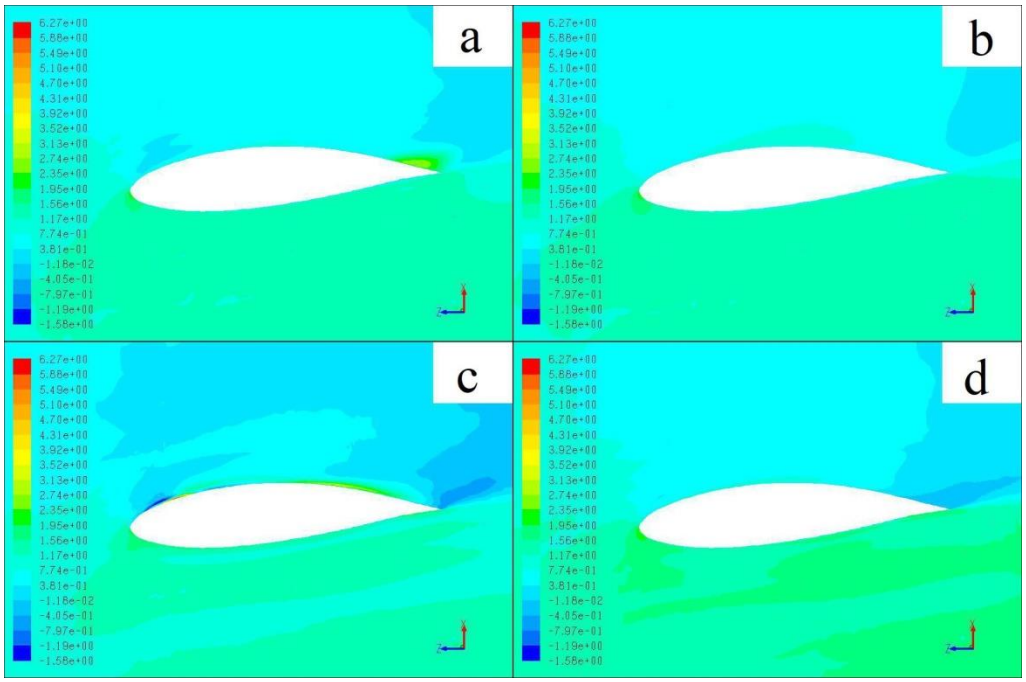

Figure 57: Contours of Radial Velocity, λ^{-1}=0.180, 90% span,
(a)SST-k-ω (b) Standard k-ε (c)MILES (d)k-kl-ω

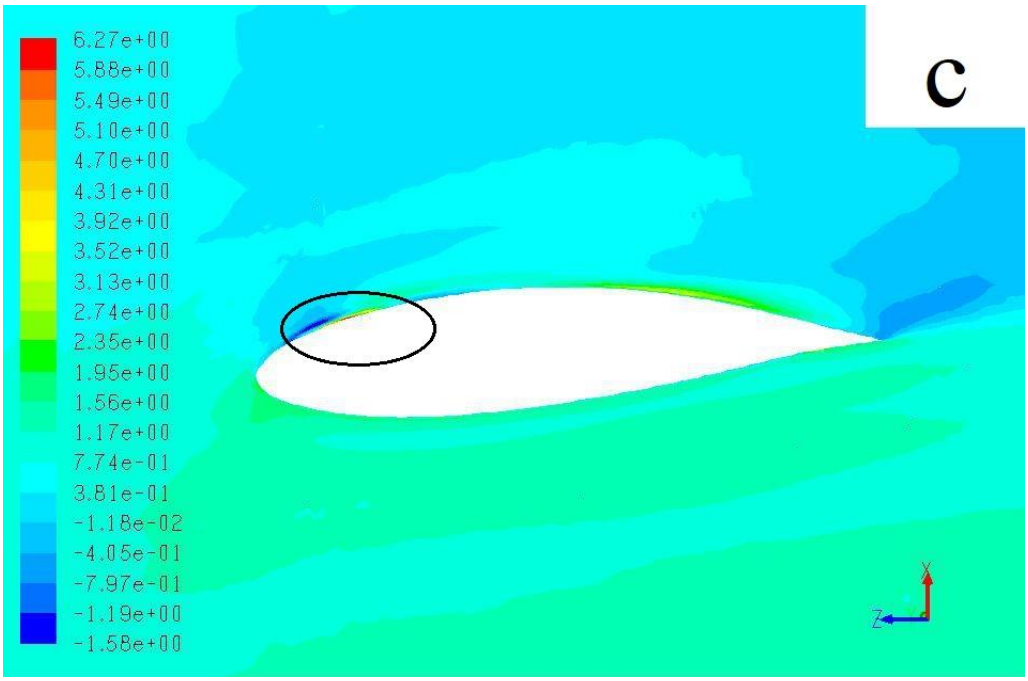

Figure 58: Contours of Radial Velocity, λ^{-1}=0.180, 90% span, (c) MILES

At $\lambda^{-1} = 0.324$ the turbine was past the point of rating. Though the flow physics at this λ^{-1} may not be of particular interest with regard to turbine performance, the results provided more insight to the variation of turbulence model predictions. The V_r was inspected at the same five span wise locations for $\lambda^{-1} = 0.324$. The MILES turbulence model predicted the highest V_r near the root of the blade, specifically at 25% and 33% (figs. 59 and 60). At these locations the k-k_L-ω and standard k-ε model predictions were similar in magnitude, with the major difference being that the k-k_L-ω V_r was predicted nearer and attached to the leading edge. At 33% span the SST-k-ω prediction behaved much like the k-k_L-ω prediction. For the remaining span wise locations, the SST-k-ω model predicted a much higher V_r than all other models. The remaining models showed no similarity in prediction with one another or with the SST-k-ω model.

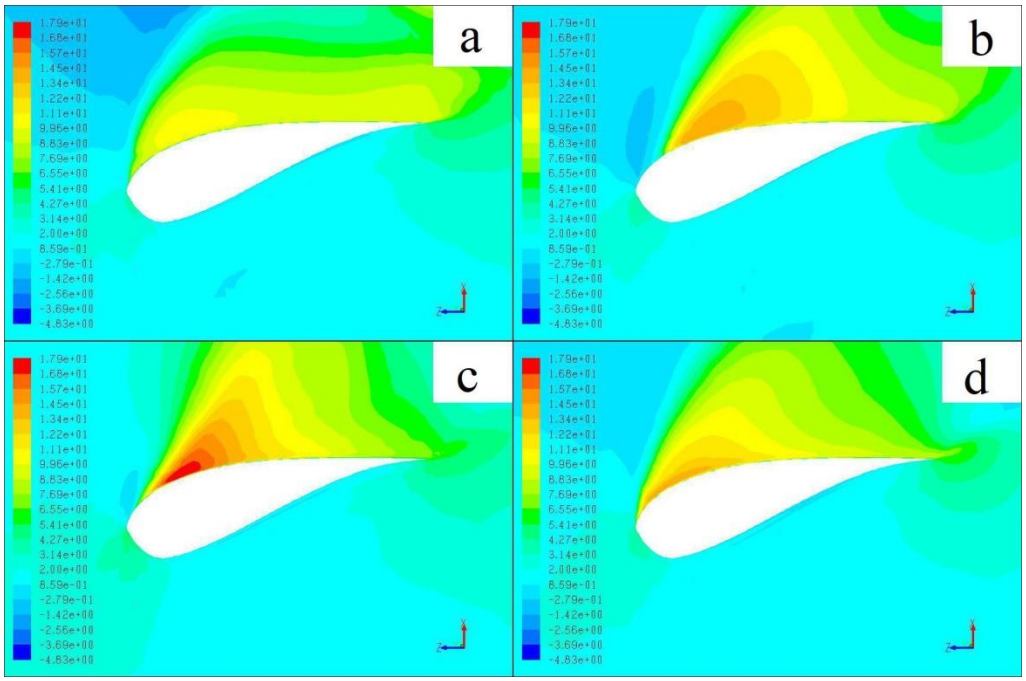

Figure 59: Contours of Radial Velocity, λ^{-1}=0.324, 25% span,
(a)SST-k-ω (b) Standard k-ε (c)MILES (d)k-kl-ω

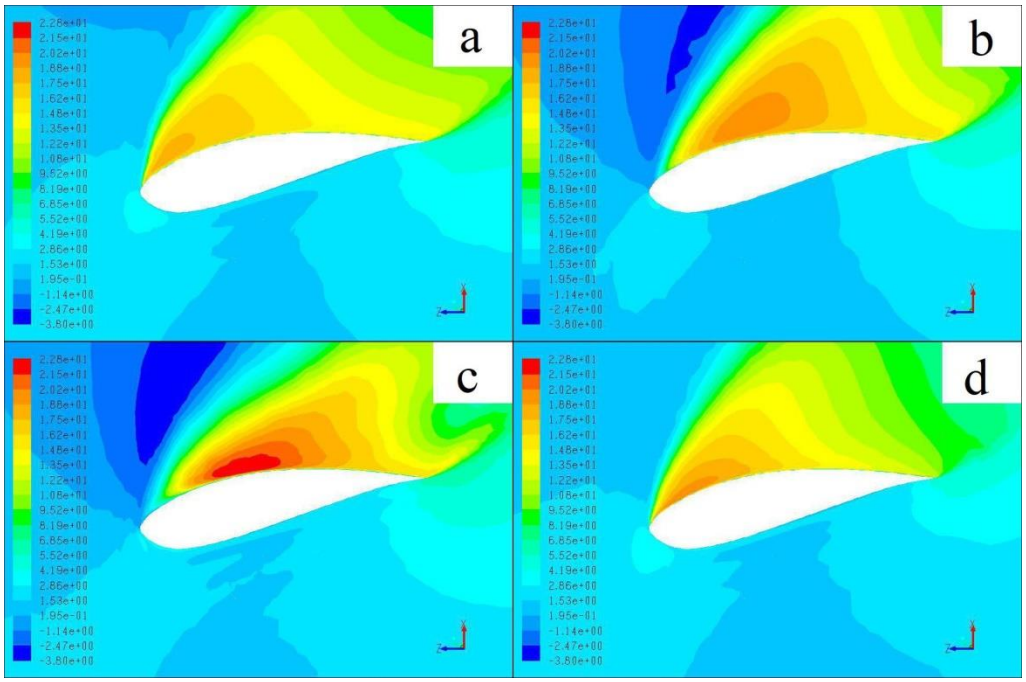

Figure 60: Contours of Radial Velocity, λ^{-1}=0.324, 33% span,
(a)SST-k-ω (b) Standard k-ε (c)MILES (d)k-kl-ω

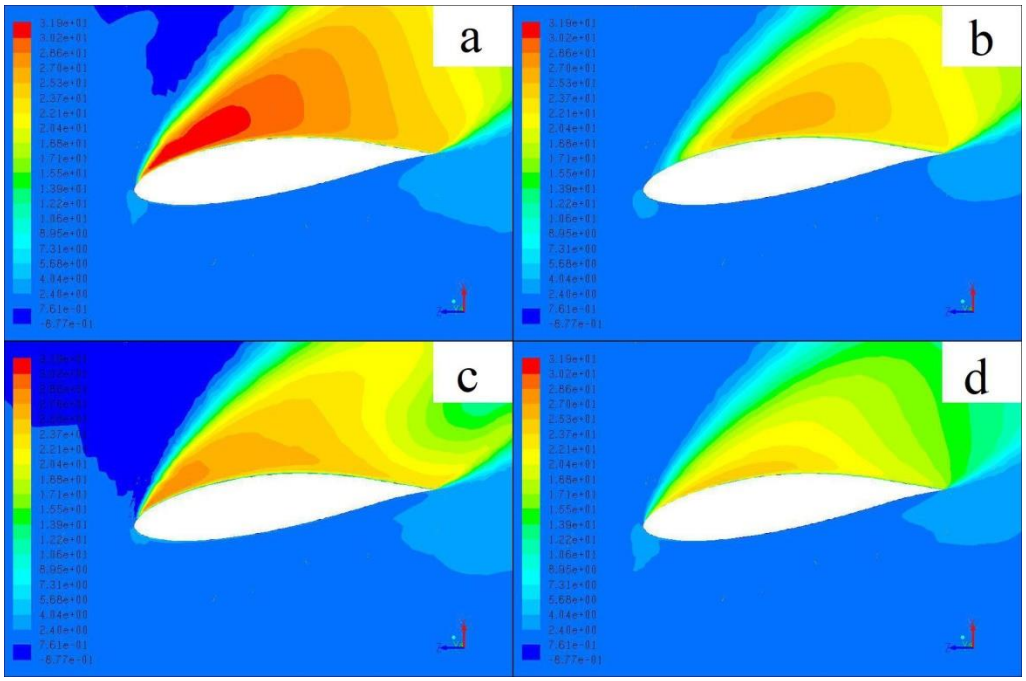

Figure 61: Contours of Radial Velocity, λ^{-1}=0.324, 50% span,
(a)SST-k-ω (b) Standard k-ε (c)MILES (d)k-kl-ω

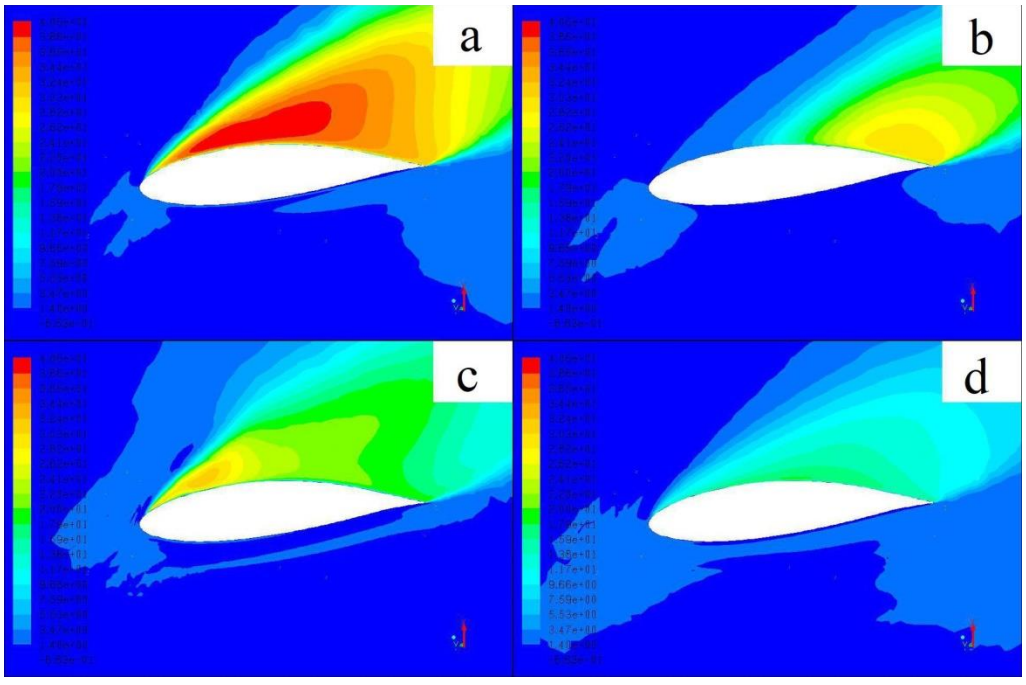

Figure 62: Contours of Radial Velocity, λ^{-1}=0.324, 75% span,
(a)SST-k-ω (b) Standard k-ε (c)MILES (d)k-kl-ω

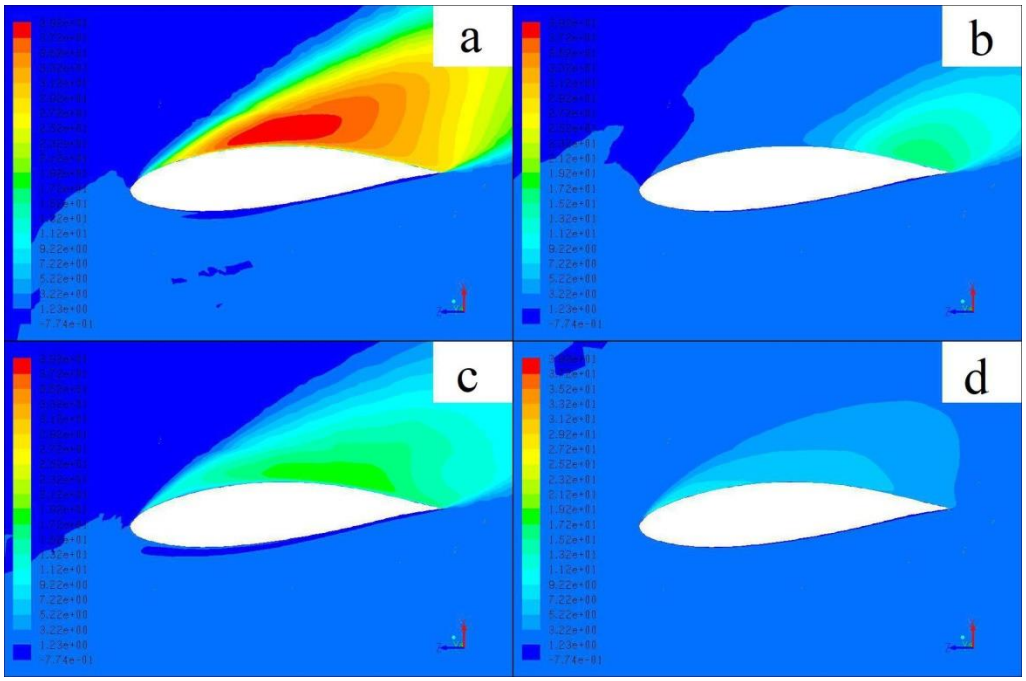

Figure 63: Contours of Radial Velocity, λ^{-1}=0.324, 90% span,
(a)SST-k-ω (b) Standard k-ε (c)MILES (d)k-kl-ω

5.7 Turbulent Kinetic Energy

Turbulent kinetic energy (TKE) is a measure of the intensity of the turbulence in the flow. Specifically, it is the magnitude of the temporal variance of the velocity vector, defined at each point in space. For the RANS models, turbulent kinetic energy (denoted by *k*) is determined by solution of a transport equation (eqs. 6, 9 and 11). For the MILES model, time-dependent velocity fluctuations are resolved in the solution and TKE is determined based on statistical averaging of the flowfield. The TKE results for three $\boldsymbol{\lambda^{-1}}$ values at five span locations are presented below.

There results using different models show substantial differences for $\lambda^{-1} = 0.072$ and $\lambda^{-1} = 0.180$ (fig. 64-73). The standard k-ε model predicted a region of high values of TKE near the stagnation point and propagating back to the trailing edge of the airfoil. It was assumed that

the high prediction of TKE was a result of the stagnation point anomaly presented by Durbin (1996). The propagation of TKE rearward was a result of the high prediction of TKE at the stagnation point, which also diffused into the boundary layer, increasing the predicted level of turbulent viscosity, which in turn produces the high values of wall shear stress and delayed separation of the boundary layer as discussed previously. Although this behavior is known to be non-physical, it is interesting that it results in an improvement in the overall prediction of power performance relative to the other models (see fig. 10).

The SST-k-ω model does not show the stagnation point anomaly and therefore predicts much lower overall levels of turbulence in and near the boundary layer. However, even though the levels are lower, the boundary layer is fully turbulent over the entire surface. In contrast, the contours of TKE highlight the transitional nature of the boundary layer as predicted by the k-k_L-ω and MILES models. The figures clearly indicate regions of both laminar and turbulent flow, which supports results seen above, particularly contours of wall shear stress and C_f profiles.

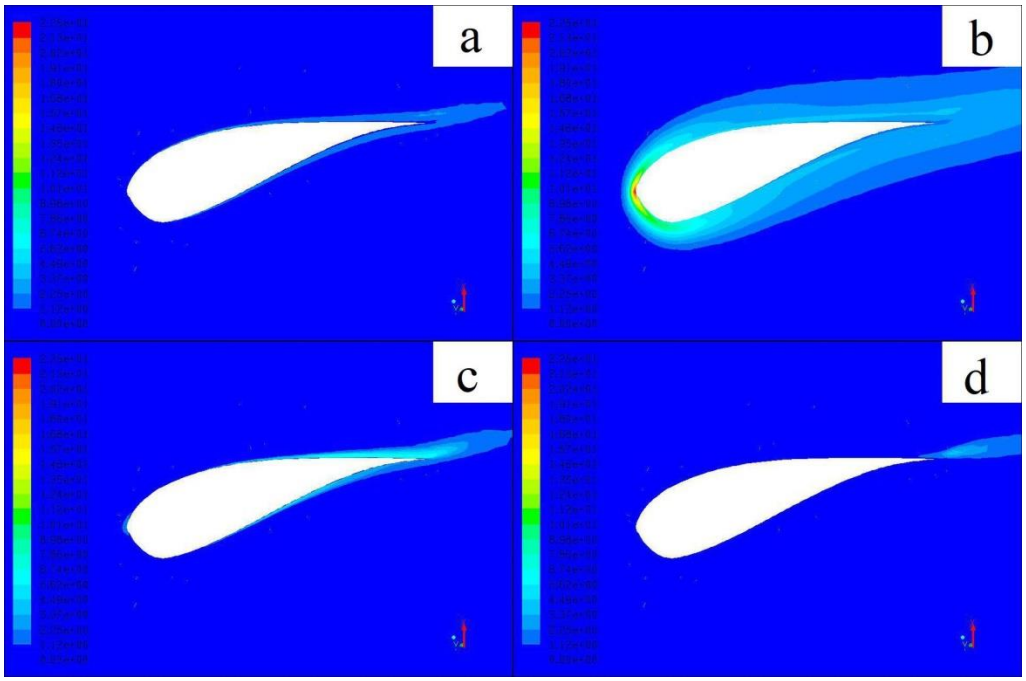

Figure 64: Contours of Turbulence Kinetic Energy, λ^{-1}=0.072, 25% span, (a)SST-k-ω (b) Standard k-ε (c)MILES (d)k-kl-ω

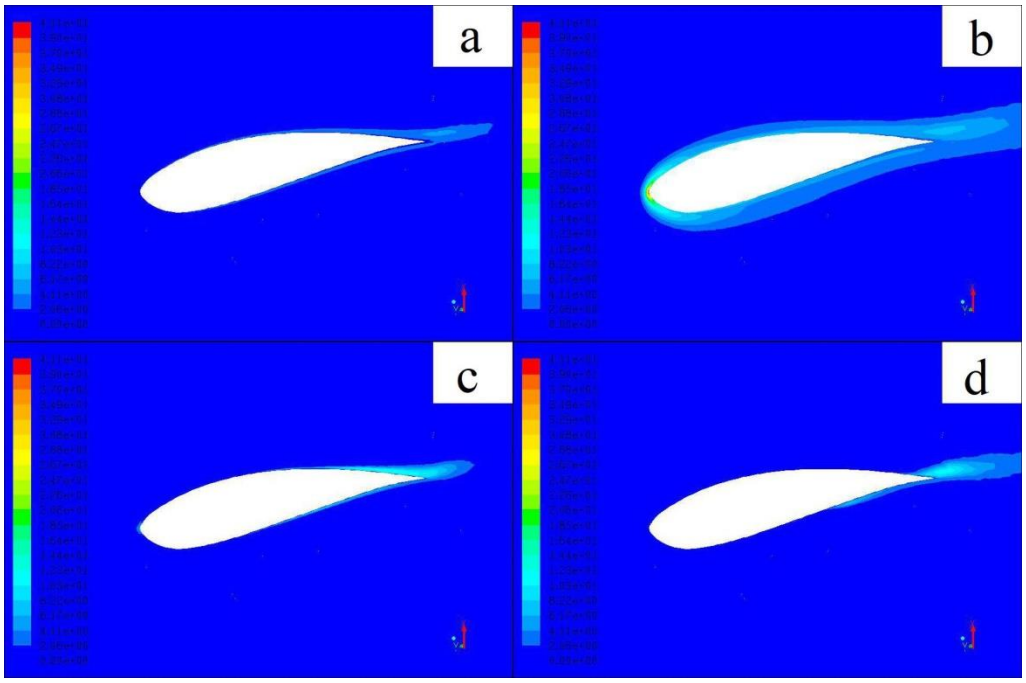

Figure 65: Contours of Turbulence Kinetic Energy, λ^{-1}=0.072, 33% span, (a)SST-k-ω (b) Standard k-ε (c)MILES (d)k-kl-ω

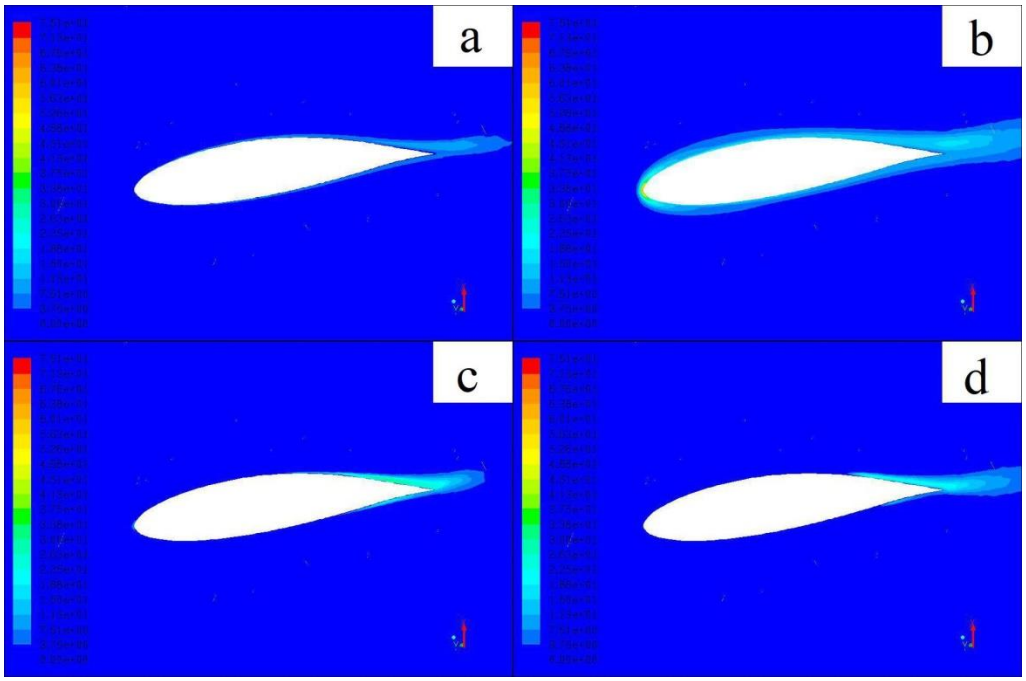

Figure 66: Contours of Turbulence Kinetic Energy, λ^{-1}=0.072, 50% span, (a)SST-k-ω (b) Standard k-ε (c)MILES (d)k-kl-ω

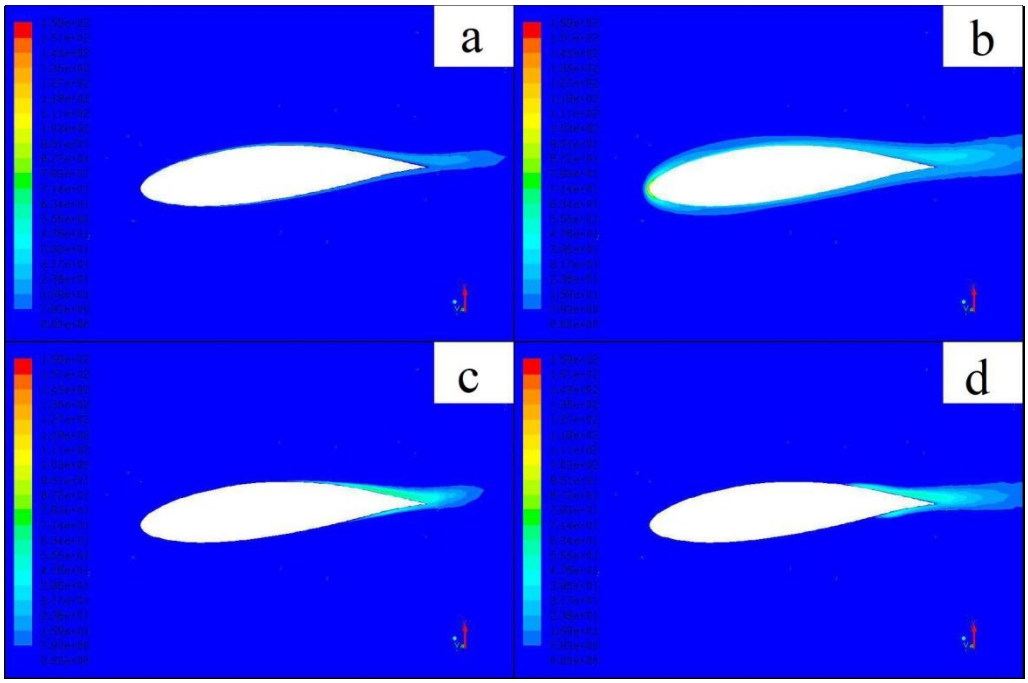

Figure 67: Contours of Turbulence Kinetic Energy, λ^{-1}=0.072, 75% span, (a)SST-k-ω (b) Standard k-ε (c)MILES (d)k-kl-ω

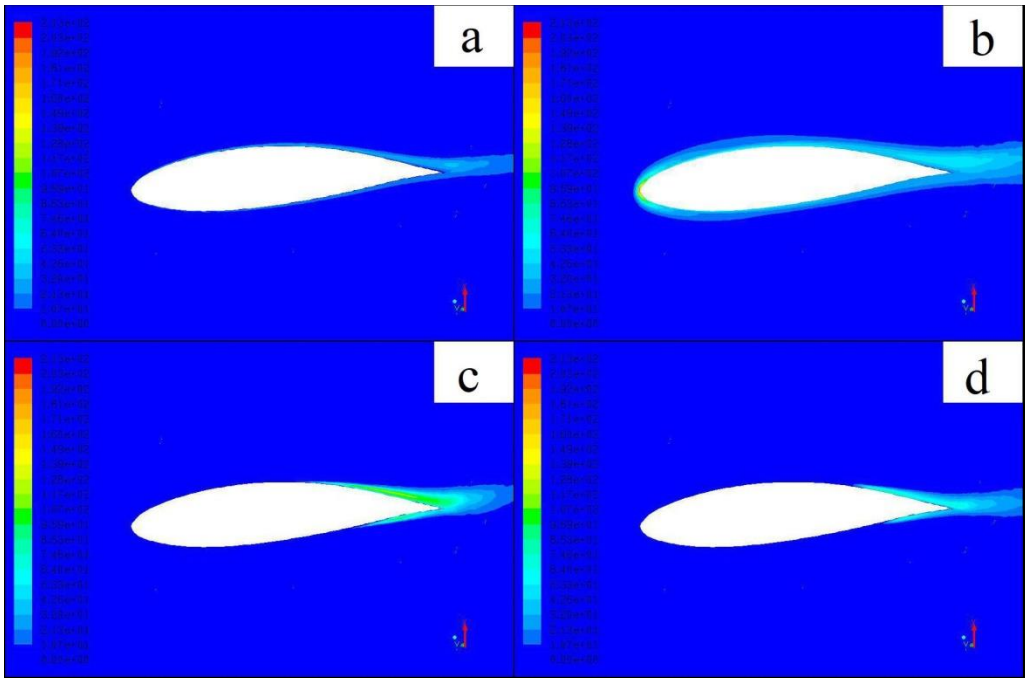

Figure 68: Contours of Turbulence Kinetic Energy, λ^{-1}=0.072, 90% span, (a)SST-k-ω (b) Standard k-ε (c)MILES (d)k-kl-ω

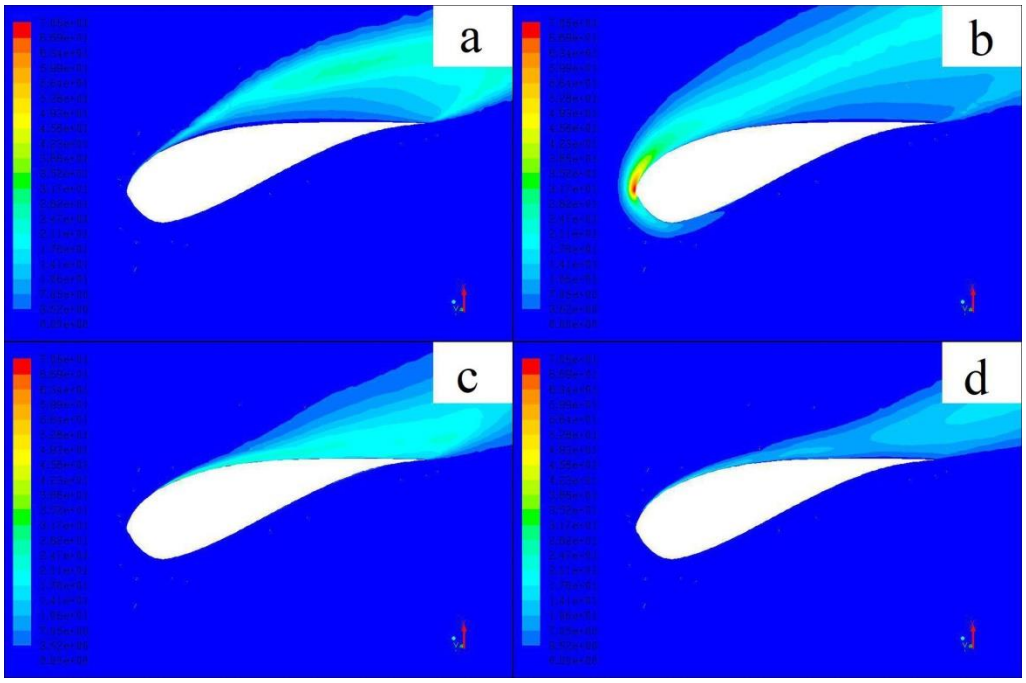

Figure 69: Contours of Turbulence Kinetic Energy, λ^{-1}=0.180, 25% span, (a)SST-k-ω (b) Standard k-ε (c)MILES (d)k-kl-ω

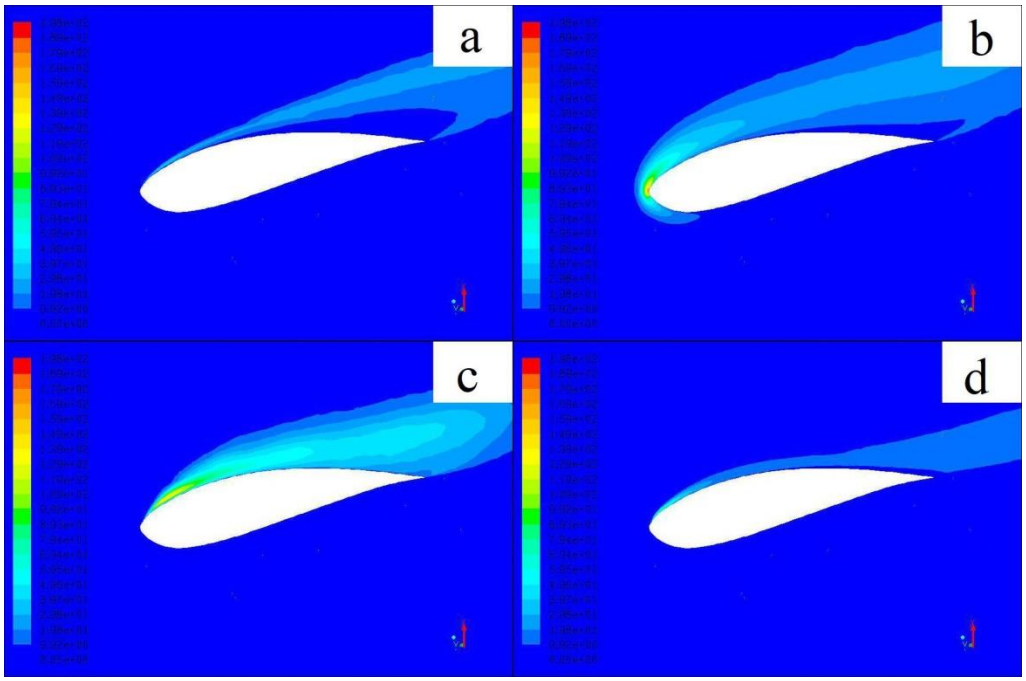

Figure 70: Contours of Turbulence Kinetic Energy, λ^{-1}=0.180, 33% span, (a)SST-k-ω (b) Standard k-ε (c)MILES (d)k-kl-ω

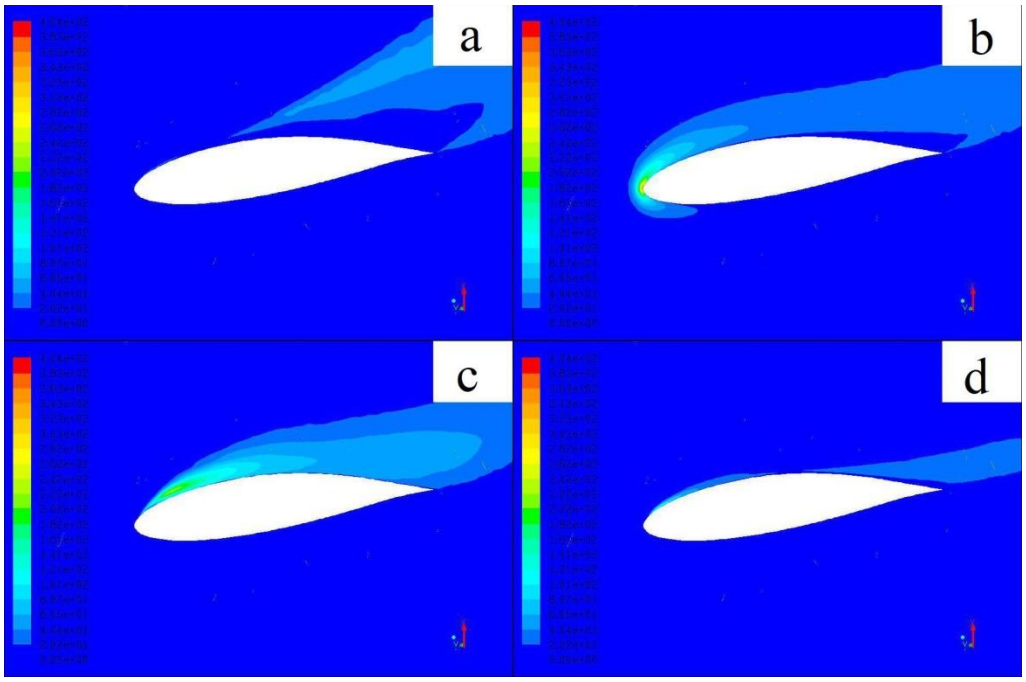

Figure 71: Contours of Turbulence Kinetic Energy, λ^{-1}=0.180, 50% span, (a)SST-k-ω (b) Standard k-ε (c)MILES (d)k-kl-ω

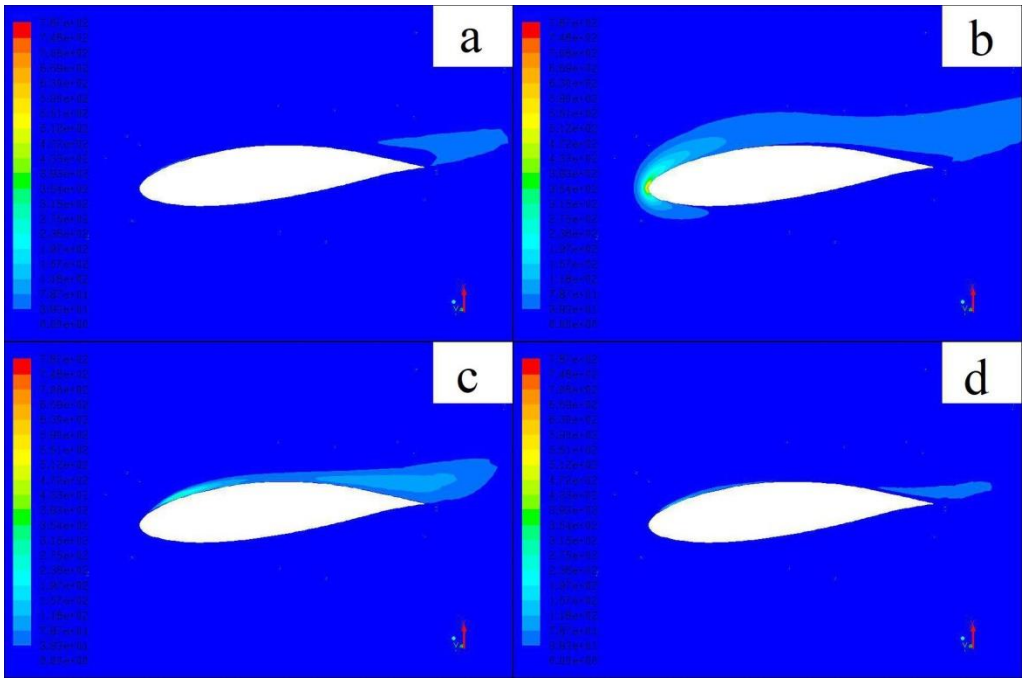

Figure 72: Contours of Turbulence Kinetic Energy, λ^{-1}=0.180, 75% span, (a)SST-k-ω (b) Standard k-ε (c)MILES (d)k-kl-ω

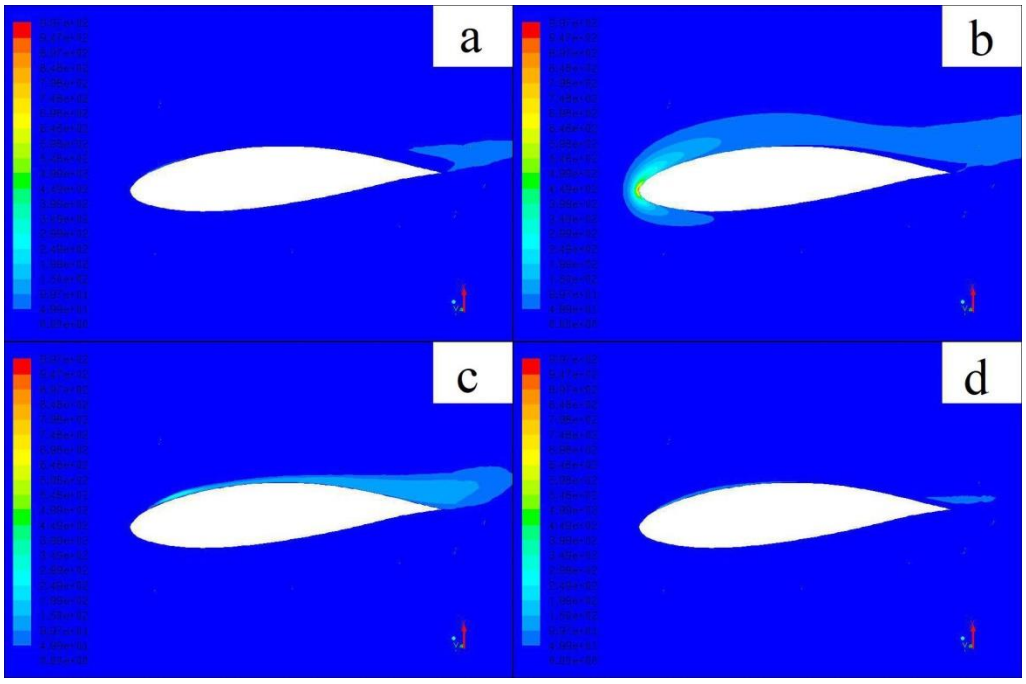

Figure 73: Contours of Turbulence Kinetic Energy, λ^{-1}=0.180, 90% span, (a)SST-k-ω (b) Standard k-ε (c)MILES (d)k-kl-ω

Model results for $\boldsymbol{\lambda^{-1} = 0.324}$ were all qualitatively very similar to one another throughout all of the span locations (fig. 75-79), though the levels of turbulence varied from model to model. The span locations that yielded the most similarity across all models was at 33%, 50%, and 75%. It is clear that at this value of $\boldsymbol{\lambda^{-1}}$ the boundary layer is completely separated over the entire airfoil. This result was consistent with the assumptions of Micallef et al. (2012).

The remaining locations yielded a large variance in TKE between each of the models. Each of the models exhibited a similar qualitative representation of TKE but the value for each model varied greatly. The MILES turbulence model predicted the largest value of TKE near the root and at the tip that was attached to the airfoil near the leading edge. The k-k_L-ω model predicted a very similar TKE profile but lacked the large region of TKE near the leading edge. This difference is likely due to the way each of the models predicts and models turbulence in the transition region. The result for SST-k-ω was expected due to the behavior of the shear stress limiter inherent to the model. This aspect helps prevent the buildup of excessive TKE near stagnation points whereas the standard k-ε struggles to do this at the stagnation point. This difference was highlighted near the root and tip where the standard k-ε model predicted a high TKE at the stagnation point and the SST-k-ω model did not present a high prediction at the stagnation point.

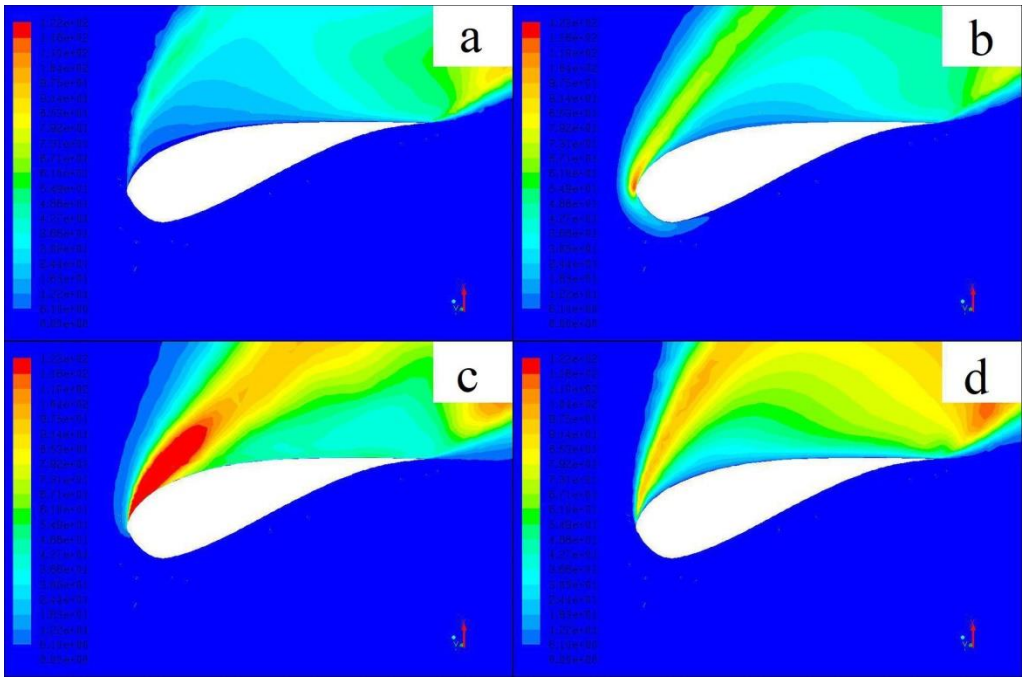

Figure 74: Contours of Turbulence Kinetic Energy, λ^{-1}=0.324, 25% span, (a)SST-k-ω (b) Standard k-ε (c)MILES (d)k-kl-ω

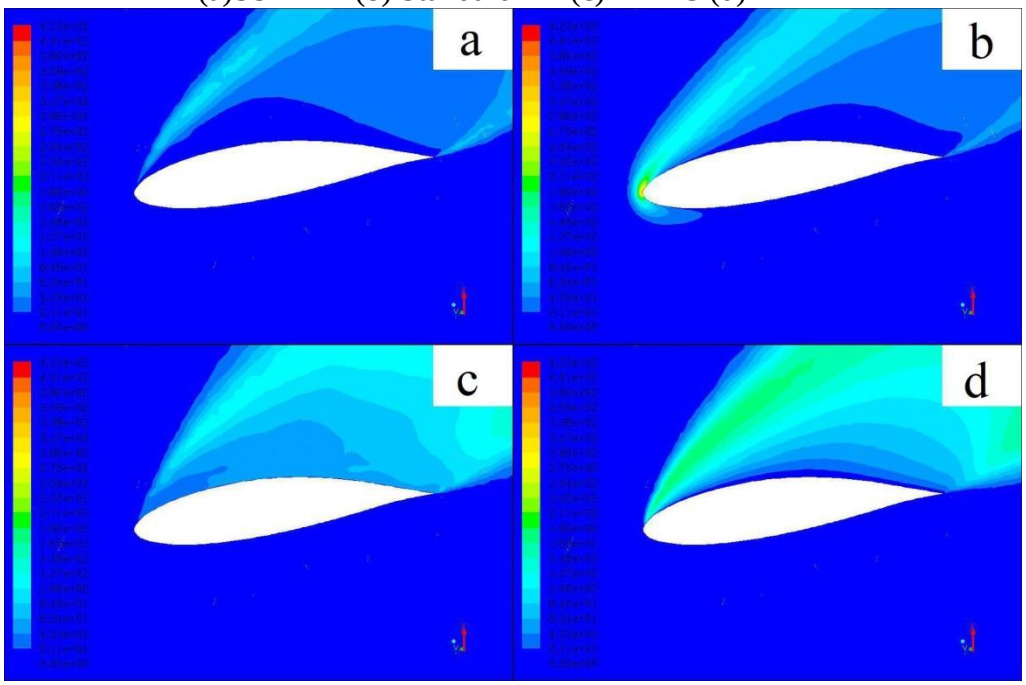

Figure 75: Contours of Turbulence Kinetic Energy, λ^{-1}=0.324, 33% span,(a)SST-k-ω (b) Standard k-ε (c)MILES (d)k-kl-ω

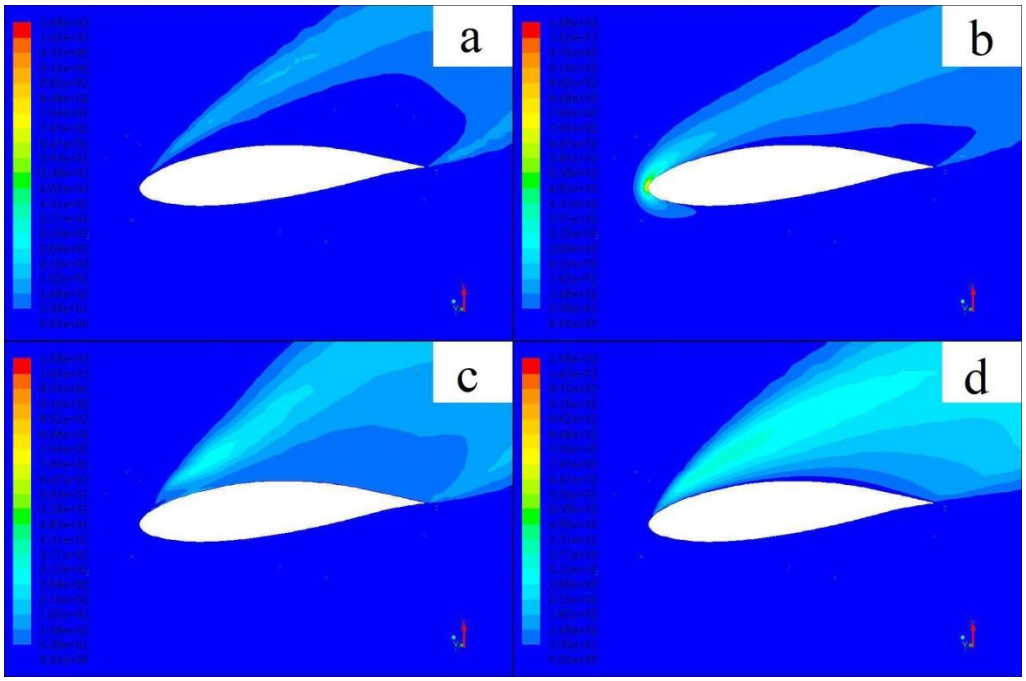

Figure 76: Contours of Turbulence Kinetic Energy, λ^{-1}=0.324, 50% span, (a)SST-k-ω (b) Standard k-ε (c)MILES (d)k-kl-ω

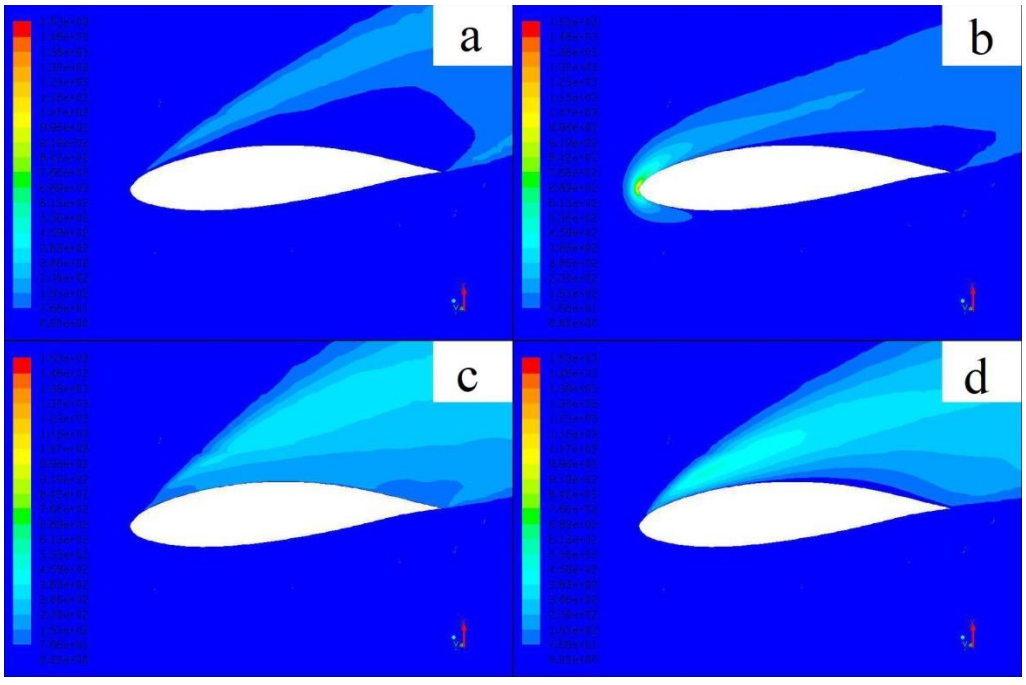

Figure 77: Contours of Turbulence Kinetic Energy, λ^{-1}=0.324, 75% span, (a)SST-k-ω (b) Standard k-ε (c)MILES (d)k-kl-ω

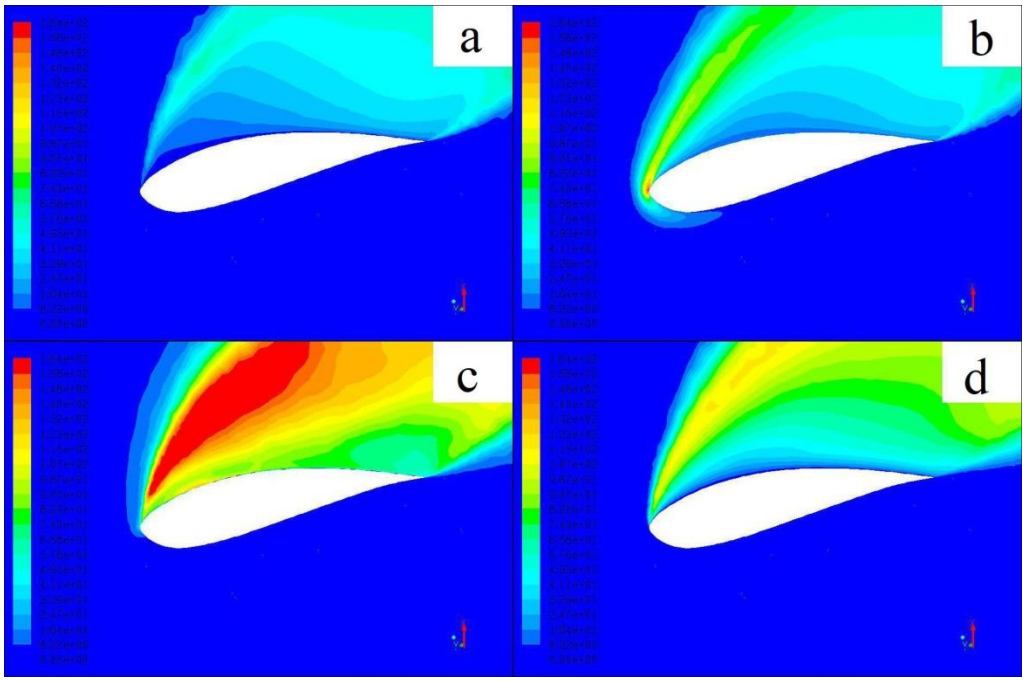

Figure 78: Contours of Turbulence Kinetic Energy, λ^{-1}=0.324, 90% span, (a)SST-k-ω (b) Standard k-ε (c)MILES (d)k-kl-ω

CHAPTER VI

CONCLUSIONS AND FUTURE WORK

6.1 Conclusions

Computational fluid dynamics (CFD) simulations of the Endurance S343 HAWT were performed for $\lambda^{-1} = 0.072 - 0.324$. These simulations were carried out using three Reynolds-averaged Navier RANS turbulence models (SST-k-ω, Transition k-k_L-ω, Standard k-ε) and an implicit large-eddy simulation model (MILES). The CFD results were then compared with experimental test results for turbine performance and coefficient of power (C_{pow}). The experimental test results did not provide data for any other aspects of the flow physics, so detailed comparison in terms of surface or field distributions of flow variables was not possible. In order to elucidate the reason for different power predictions using different turbulence models, several other results, including C_p, C_f, τ_w, V_r, and TKE, were compared to find differences for each of the models.

Two different experimental data sets were used for validation. It was observed that the experimental test results yielded different results for the same geometry and test conditions when compared with one another. This difference highlights the inherent uncertainty in measurements of complex flow systems. This was also an interesting parallel when looking into the turbulence model behavior for the numerical simulations as it provided some insight into the nature and complexity of three-dimensional studies.

When comparing results from the different turbulence models, dach model exhibited behaviors that were unlike their counterparts. The k-k_L-ω model produced the highest overprediction of power in comparison with the WE experimental results and but predicted the inverse tip speed ratio (λ^{-1}) corresponding to peak performance within 7% of both of the

experiments. This model also predicted an anomalous behavior that was also seen in the WE test, a slight decrease and subsequent increase in power near the peak performance value. The SST-k-ω model showed qualitative similarities with the experimental tests with regards to performance, and closer quantitative agreement than the k-k_L-ω model. Stall was predicted at a value of λ^{-1} more than 20% less than the test results, however the maximum power output was found to be within 6% of the experiments.

The MILES turbulence model failed to predict the power output and the value of λ^{-1} at stall with reasonable agreement. Both were found to be outside of differ by more than 12% from the experimental data. The standard k-ε model predicted the performance well for $\lambda^{-1} = 0.072 - 0.108$. This quantitative similarity diminished at values of λ^{-1} past this range. The point of rating was found to be at a λ^{-1} that was more than 20% higher than either experimental result yet the power output was predicted to only be 6% lower than each experiment.

Based on the comparison of power output, no single turbulence model could be judged to be inherently superior, and all showed non-trivial disagreement with measurement data over at least part of the speed range investigated. Furthermore, each of the models were found to show significant differences from the others over all or part of the speed range. Not only was no model consistent with the experiments, no model was consistent with any other model.

Results from the CFD simulations of this HAWT did not provide a turbulence model that completely and accurately modeled the experimental tests with a high degree of certainty. Each turbulence model displayed differing characteristics. The standard k-ε model modeled excessive turbulence as a result of the stagnation point anomaly. The effect of this was increased wall shear and drag. This increase led to delayed separation yet it was this turbulence model that provided

the closest result to the experiments. The stagnation point anomaly is a shortcoming of the standard k-ε model. This made justification of the accuracy of the turbulence model difficult. More concretely, no justification of model accuracy could be made due to the similarity of the model results with experimental results being predicated on a shortcoming of the turbulence model itself. The SST-k-ω predicted a fully turbulent boundary layer. This prediction is likely not a realistic representation of what was physically occurring within the boundary layer. However, the SST-k-ω model yielded reasonable agreement with the experiments through much of the speed range up to the point of rating especially since the CFD results should be greater than the experimental results due to mechanical and electrical losses. The k-k_L-ω model provided the best qualitative agreement. This model predicted a laminar boundary layer which led to a reduction in wall shear. The consequence of this was early separation. These factors caused the shape of the power curve for this turbulence model to closely resemble the experimental results more than any other model. The MILES turbulence model predicts transition in the boundary layer. The result of this was early separation and stall. This resulted in the point of rating shifting to a lesser λ^{-1} than the experimental results. The results for this model could likely be improved upon by refining the grid. This grid refinement would allow more of the turbulent fluctuations to be accurately resolved.

Each of the turbulence models was employed on a consistent test case. A key focus for this study was to effectively address every aspect of the test case so the turbulence model results could be compared. For this test case the geometry and dimensionality were held constant. To ensure turbulence model results were not varied as a result of poor selection of boundary conditions, the placement as well as the type of boundary conditions was studied at length. The grid was refined to a level that well exceeds previous works in open literature. Even when taking

special care of the aforementioned aspects the results of each turbulence model was highly varied. This led to the conclusion that turbulence model selection has a great impact on CFD results and CFD end users should always be aware of the inherent uncertainty when using CFD for analysis and design.

6.2 Future Work

Future efforts will focus on a more in-depth analysis of the behavior of these models using a three-dimensional geometry. Additional test cases are necessary in development of a more comprehensive picture of model performance. Suggestions include larger turbines at a higher Reynolds number and alternative models. Potential models for investigation are hybrid RANS-LES models. These models could be employed and would take advantage of the strengths of each approach. Further investigation into the effects a more refined grid has on the results of these models is also of high importance. This will facilitate more accurate results when employing large eddy simulation.

LIST OF REFERENCES

Abdelsalam, A. M., Boopathi, K., Gomathinayagam, S., Hari Krishnan Kumar, S., & Ramalingam, V. (2014). Experimental and numerical studies on the wake behavior of a horizontal axis wind turbine. *Journal of Wind Engineering and Industrial Aerodynamics,128*, 54-65. doi:10.1016/j.jweia.2014.03.002

Abdelsalam, A. M., & Ramalingam, V. (2014). Wake prediction of horizontal-axis wind turbine using full-rotor modeling. *Journal of Wind Engineering and Industrial Aerodynamics,124*, 7-19. doi:10.1016/j.jweia.2013.11.005

Aftab SMA, Mohd Rafie AS, Razak NA, Ahmad KA (2016) Turbulence Model Selection for Low Reynolds Number Flows. PLoS ONE 11(4):e0153755. doi:10.1371/journal.pone.0153755

Ameur, K., Masson, C., & Eecen, P. J. (2011). 2D and 3D numerical simulation of the wind-rotor/nacelle interaction in an atmospheric boundary layer. *Journal of Wind Engineering and Industrial Aerodynamics,99*(8), 833-844. doi:10.1016/j.jweia.2011.06.002

T.J. Barth and D.C. Jesperson, The design and application of upwind schemes on unstructured meshes, AIAA 89-0366 (1989).

Durbin, P. (1996). On the k-3 stagnation point anomaly. *International Journal of Heat and Fluid Flow,17*(1), 89-90. doi:10.1016/0142-727x(95)00073-y

Elfarra, M. A., Sezer-Uzol, N., & Akmandor, I. S. (2013). NREL VI rotor blade: Numerical investigation and winglet design and optimization using CFD. *Wind Energy,17*(4), 605-626. doi:10.1002/we.1593

Endurance Wind Power « WWEA Small Wind Platform. (2012). Retrieved July 11, 2019, from http://small-wind.org/business-directory/139/endurance-wind-power/

Fureby, C., & Grinstein, F. (1999). Monotonically integrated large eddy simulation of free shear flows. *AIAA Journal,37,* 544-556. doi:10.2514/3.14208

Hefny, M. M., & Ooka, R. (2009). CFD analysis of pollutant dispersion around buildings: Effect of cell geometry. *Building and Environment,44*(8), 1699-1706. doi:10.1016/j.buildenv.2008.11.010

Herbert-Acero, J. F., Probst, O., Rivera-Solorio, C. I., Castillo-Villar, K. K., & Méndez-Díaz, S. (2015). An Extended Assessment of Fluid Flow Models for the Prediction of Two-Dimensional Steady-State Airfoil Aerodynamics. *Mathematical Problems in Engineering,2015,* 1-31. doi:10.1155/2015/854308

Jasak, H., H.G. Weller, and A.D. Gosman. "High Resolution NVD Differencing Scheme for Arbitrarily Unstructured Meshes." *International Journal for Numerical Methods in Fluids* 31.2 (1999): 431-49.

Jones, W., & Launder, B. (1972). The prediction of laminarization with a two-equation model of turbulence. *International Journal of Heat and Mass Transfer,15*(2), 301-314. doi:10.1016/0017-9310(72)90076-2

Krogstad, P. -., & Lund, J. (2011). An experimental and numerical study of the performance of a model turbine. *Wind Energy,15*(3), 443-457. doi:10.1002/we.482

Mathur, S.R., J.Y. Murthy, 1997. A pressure based methods for unstructured meshes. Numer. Heat Trans. Part B., 31: 195-215. DOI: 10.1080/10407799708915l0

Menter, F. R. (1994). Two-equation eddy-viscosity turbulence models for engineering applications. *AIAA Journal,32*(8), 1598-1605. doi:10.2514/3.12149

Micallef, D., Bussel, G. V., Ferreira, C. S., & Sant, T. (2012). An investigation of radial velocities for a horizontal axis wind turbine in axial and yawed flows. *Wind Energy*,*16*(4), 529-544. doi:10.1002/we.1503

Patankar, and Spalding. "A Calculation Procedure for Heat, Mass and Momentum Transfer in Three-dimensional Parabolic Flows." *International Journal of Heat and Mass Transfer* 15.10 (1972): 1787-806.

Sezer-Uzol N. Unsteady flow simulations around complex geometries using stationery or rotating unstructured grids. PhD Thesis, The Pennsylvania State University, 2006.

Thumthae, C., & Chitsomboon, T. (2009). Optimal angle of attack for untwisted blade wind turbine. *Renewable Energy*,*34*(5), 1279-1284. doi:10.1016/j.renene.2008.09.017

U.S. Installed and Potential Wind Power Capacity and Generation. (2019). Retrieved March 27, 2019, from https://windexchange.energy.gov/maps-data/321

Walters, D. K., & Cokljat, D. (2008). A Three-Equation Eddy-Viscosity Model for Reynolds-Averaged Navier–Stokes Simulations of Transitional Flow. *Journal of Fluids Engineering*,*130*(12), 121401. doi:10.1115/1.2979230

Wilcox, D. A. (1994). Simulation of Transition with a Two-Equation Turbulence Model. *AIAA Journal*,*32*(2), 247-255. doi:10.2514/3.59994

Wind Facts at a Glance. (n.d.). Retrieved March 27, 2019, from https://www.awea.org/wind-101/basics-of-wind-energy/wind-facts-at-a-glance

D. L. (2012). *Wind Turbine Generator System Endurance S-343 Power Performance Test Report*(pp. 1-89, Rep. No. SWCC-10-09). Spanish Fork, UT: Windward Engineering, LLC.

Wood, D. H. (2013). *Small Wind Turbines: Analysis, design and application*. London: Springer. doi:10.1007/978-1-84996-175-2